

**Polarized target
for the measurement
of
the gluon contribution to the nucleon spin
in the COMPASS experiment**

Nagoya University

Thesis for the degree Doctor of Philosophy in Physics
by

Naoki TAKABAYASHI ¹

2002

¹ Supported by Research Fellowships of the Japan Society for the Promotion of Science for Young Scientists.

CONTENTS

1. <i>Introduction</i>	1
2. <i>Spin structure of the nucleon</i>	5
2.1 Deep inelastic scattering	5
2.2 Cross section and structure functions in unpolarized DIS	7
2.3 Cross section and structure functions in polarized DIS	9
2.4 Structure functions and spin puzzle in Parton Model picture	13
2.4.1 Parton distribution	14
2.4.2 Spin puzzle in Parton Model picture	16
2.5 Structure functions and spin puzzle in QCD evolved Parton Model	18
2.5.1 Unpolarized structure functions	18
2.5.2 Factorization schemes	20
2.5.3 DGLAP equation and Scaling violation	22
2.5.4 Spin-dependent structure functions and polarized DGLAP equation	23
2.6 Interpretation of small $\Delta\Sigma$. Is gluon contribution large?	24
2.6.1 Sum rules	25
2.6.2 Axial anomaly	26
3. <i>COMPASS experiment</i>	30
3.1 Open charm lepto-production via photon-gluon fusion	30
3.2 Expectations	35
3.2.1 Luminosity	35
3.2.2 Reconstruction of the open charm events	35
3.2.3 Statistical accuracy	37
3.3 Comparison with the other experiments on Δg	40
3.3.1 High p_T hadron pairs	40
3.3.2 $p\bar{p}$ collision	41
3.3.3 Comparison of the expected precisions and the kinematic ranges	42

3.4	Experimental setup	43
3.4.1	Polarized muon beam	44
3.4.2	Polarized target	47
3.4.3	COMPASS spectrometer	49
4.	<i>Polarized Target</i>	54
4.1	Dynamic nuclear polarization	55
4.1.1	Definition of polarization	55
4.1.2	Thermal equilibrium polarization	56
4.1.3	Zeeman splitting	57
4.1.4	Dipolar-dipolar interaction	58
4.1.5	Macroscopic effects	63
4.1.6	Hyperfine interaction	64
4.1.7	Equal spin temperature	70
4.2	The polarization measurement	72
4.2.1	Nuclear magnetic resonance	72
4.2.2	Detection of the absorption function	73
4.2.3	Area method	77
4.3	Polarized target apparatus	79
4.3.1	Dilution refrigerator	79
4.3.2	Superconducting magnet	85
4.3.3	Microwave system	88
4.3.4	Nuclear magnetic resonance system	90
4.4	Target material ${}^6\text{LiD}$	92
4.4.1	Choice of the material	92
4.4.2	Preparation of ${}^6\text{LiD}$	97
4.5	Results from polarized target	99
4.5.1	TE calibration	99
4.5.2	Deuteron polarization	104
4.5.3	Paramagnetic resonance at high polarization	108
4.5.4	Verification of equal spin temperature theory	109
5.	<i>Superconducting magnet for the polarized target</i>	112
5.1	Electromagnetics	113
5.2	Cryogenics	119
5.2.1	Normal continuous operation	121
5.2.2	Cooling down phase	122
5.3	Active protection system	124
5.4	Anomalous cases	127

6. <i>Conclusions and Outlook</i>	131
<i>Appendix</i>	134
A. <i>Parameters in Chapter 3</i>	135
B. <i>Parameters in Chapter 4</i>	137
C. <i>Parameters in Chapter 5</i>	139

LIST OF FIGURES

2.1	Feynman diagram of DIS	6
2.2	DIS in the infinite momentum frame	15
2.3	Amplitudes of DIS off a quark	18
2.4	Squares of the Feynman diagram involving real gluon emission	19
2.5	Squares of the Feynman diagrams with a initial gluon	19
2.6	Illustration of the QCD processes of the four splitting functions	21
2.7	Diagrams relevant to axial anomaly	27
3.1	Example of the possible shapes of Δg	31
3.2	Feynman diagram of open charm leptonproduction via photo- gluon fusion	32
3.3	Expected statistical accuracy	38
3.4	Feynman diagram of the high p_T jet pair	40
3.5	Feynman diagram of the γ production in pp or $p\bar{p}$ collisions .	42
3.6	Projected accuracies on $\Delta g/g$	43
3.7	M2 polarized muon beam line	45
3.8	Spin configurations of in the COMPASS experiment	48
3.9	COMPASS spectrometer in 2001	51
4.1	DNP mechanism via dipolar-dipolar interaction	62
4.2	DNP mechanism via hyperfine interaction	70
4.3	Series LRC resonance circuit	74
4.4	Side view of the COMPASS polarized target apparatus	80
4.5	Materials inside the particle detection acceptance	81
4.6	Diagram of the dilution refrigerator	82
4.7	Phase diagram of ^3He - ^4He mixture	84
4.8	Operation of the magnet system during the field rotation . . .	86
4.9	Magnetic field during the field rotation	87
4.10	Microwave system	88
4.11	Schematic outline of the NMR system	91
4.12	Face centered cubic structure	92
4.13	Simple illustration of the F-center	98

4.14	Paramagnetic resonance spectrum of the irradiated ${}^6\text{LiD}$. . .	99
4.15	NMR signal extraction	100
4.16	Relaxation of the nuclear spin to the thermal equilibrium . .	101
4.17	Build-up of the deuteron polarization	105
4.18	Enhanced deuteron signals	106
4.19	Paramagnetic resonance spectrum of ${}^6\text{LiD}$ at high polarization	108
4.20	Test of EST	110
5.1	Illustration of the coils in Magnet	113
5.2	Electric scheme of Solenoid and Corrections	115
5.3	Electric scheme of Dipole	116
5.4	Cryogenic scheme of Magnet	120

LIST OF TABLES

3.1	Numerical presentation of the cross sections of open charm lepto-production	36
3.2	Parameters of the polarized muon beam	46
4.1	Thickness of the material in the polarized target apparatus	89
4.2	Figure of merit of the target materials	95
4.3	Measurements for TE calibration	102
4.4	Errors in TE calibration	103
4.5	Maximum deuteron polarization	107
5.1	Electromagnetic characteristics of Solenoid	114
5.2	Electromagnetic characteristics of Corrections	117
5.3	Electromagnetic characteristics of Dipole	118
5.4	DL (Slow discharge)	125
5.5	DR (Rapid discharge) 1	126
5.6	DR (Rapid discharge) 2	127
5.7	Anomalous cases, AN1-AN3	128
5.8	Anomalous cases, AN4-AN6	129
5.9	Anomalous cases, AN7	130
A.1	Variables in Chapter 3	136
B.1	Constants in Chapter 4	138
B.2	Units for Chapter 4	138
B.3	Abbreviations for Chapter 4	138
C.1	Terms in Chapter 5	140
C.2	Abbreviations in Chapter 5	141

1. INTRODUCTION

Scattering a beam of elementary particles such as leptons off a target of nucleons provides an experimental technique for investigating the structure of the nucleons. In low energy scattering, where the beam energy is less than the target mass, the nucleon looks like a point-like particle. However, as the energy of the incident lepton increases, the structure of nucleon begins to unveil. When the lepton energy increases above the nucleon mass, the charge distributions of the nucleons are probed. The deviation of the measured cross section from the known cross section for a point-like particle describes the charge distribution of the composite objects. The form factors, or charge distributions, of the nucleons were measured by this technique in the experiments during the 1970s at SLAC.

If the lepton energy increases even higher, then the deep inelastic scattering (DIS) regime is reached. In DIS, the lepton has high enough energy to break apart the nucleons and therefore to probe the internal structure of the nucleons, namely the structure functions. Polarized DIS experiment, in which polarized leptons are scattered off a target of polarized nucleons, provides the information on the internal structure of the nucleon spin. The spin-dependent structure function of the nucleon was experimentally measured first by the Yale-SLAC Collaboration E80 [1], and then by the E130 Collaboration [2] in 1970s and early 1980s, using 8 and 20 GeV electron beam. At CERN, the European Muon Collaboration (EMC) [3, 4] investigated the proton spin structure during the 1980s using 90 GeV muon beam.

The EMC results reported in 1988 attracted the attentions of the researchers, which state that the quarks carry unexpectedly small fraction (0.128 ± 0.013 (*stat*) ± 0.019 (*sys*)) of the nucleon spin. The EMC interpreted its data in the framework of the naive Parton Model and found that the experimentally measured value of the Ellis-Jaffe Sum Rule [5] for the proton is too small compared to the theoretical prediction. Following the EMC results, extensive theoretical and experimental works were performed to understand the spin structure of the nucleon in 1990s. One of the theoretical advances was to describe the spin dependent structure function in the framework of Quantum Chromodynamics (QCD), showing the Q^2 evo-

lution of the structure functions due to the interaction between quarks and gluons. Experimentally, precise measurements had been carried out by the Spin Muon Collaboration (SMC) at CERN using 100 and 190 GeV muon beam with proton and deuteron target, by a series of experiments at SLAC, E142, E143, E154 and E155 using 26-50 GeV electron beam with proton, deuteron, and ^3He target, and by the HERMES collaboration at DESY using 28 GeV electron beam with proton and ^3He target. These experimental data together with the QCD evolution analysis still show that the quarks carry unexpectedly small fraction, 20-30 %, of the nucleon spin at $Q^2 = 10 \text{ GeV}^2$ and that the Ellis-Jaffe Sum Rule is violated. On the other hand, the Bjorken Sum Rule [6, 7], which is the difference of the first moment of the spin-dependent structure function g_1 between a proton and a neutron and which is a model independent result of QCD, was confirmed.

Although there is no principal reason that the quarks should carry the entire nucleon spin from the pure theoretical view of QCD, it still seems surprising that the quarks are responsible only for such a small fraction. According to the conservation of the angular momentum, the missing part of the nucleon spin should be explained by the gluon spin or/and the angular momentum of partons. The direct measurements on their quantities are awaited. One of the main goals of the COMPASS experiment is to measure the gluon polarization $\Delta g/g$ by a clean channel, namely open charm lepto-production, with a statistical accuracy of 10 %. The COMPASS experiment uses 100-190 GeV polarized muon beam with a polarized nucleon target. In addition to COMPASS, various experiments, HERMES at DESY, STAR and PHENIX at RHIC-BNL, E161 at SLAC are aiming to measure $\Delta g/g$ precisely by different approaches and at complementary kinematic ranges. The precise data are expected to be reported in coming years.

This thesis pertains to the polarized target for the COMPASS experiment. Apparently, the COMPASS experiment cannot run without polarized target and the high performance is required. The author made an essential contribution in the preparation, the development, the installation, the commissioning and the evaluation of the results of the complex COMPASS polarized target system in all the aspects but the target material which had been developed and produced by the collaborators in Bochum university. The challenges were

- to realize the world largest solid polarized target to obtain higher statistics,
- to achieve high polarization by high performance hardware setup,

- to measure the polarizations of all the polarizable nuclear species over the large volume of the target material precisely without harming the particle physics experiment,
- to minimize the non-target material to reduce the multiple scattering for the efficient reconstruction of D^0 from the decay particles,
- to change the sign of the target polarization frequently, in order to allow the measurement of the double spin asymmetry of open charm lepto-production.

The author was particularly in charge of the large superconducting magnet for the polarized target. In the long term, statistics limited experiment, the stability of such a key apparatus is a crucial factor and the attentions was payed for it. The main feature of this thesis is to report the apparatus, the nature of the target material related to the dynamic nuclear polarization, and the results of the polarized target.

Chapter by chapter, the thesis is organized in the following manner.

Chapter 2 reviews the today's knowledge on the spin structure of the nucleon. The basics of DIS is described as a experimental tool to access the spin-dependent structure functions. The quark contribution to the nucleon spin is discussed in the two theoretical frameworks, namely naive Parton Model and QCD evolved Parton Model. In the latter, the role of gluon spin is discussed. The violation of the Ellis-Jaffe sum rule and the verification of the Bjorken sum rule are shown. The theoretical idea of axial anomaly is given as one of the scenarios which might explain the missing spin of the nucleon.

Chapter 3 describes the COMPASS experiment whose spectrometer was commissioned in 2001 and started data taking in 2002. The theoretical basis to investigate the gluon polarization $\Delta g/g$ of the nucleon spin is presented. The expected accuracy of the COMPASS experiment is shown in comparison with the other forth coming and future experiments. The apparatus of the COMPASS experiment is described in the general terms.

Chapter 4 reports the COMPASS polarized target. The theories on the dynamic nuclear polarization and those on the determination of the target polarization are shown with the orientation of their application to the practical system. The apparatus of the COMPASS polarized target is described by dividing it into the sub-systems, the dilution refrigerator, the superconducting magnet, the microwave system, and the nuclear magnetic resonance system. The efforts to minimize the non-target materials are reported in the

context of the microwave cavity design. The choice of ${}^6\text{LiD}$ as a target material is discussed and its preparation technique is briefly presented. Then, the results from the polarized target are reported, including the calibration of the polarization measurement, deuteron polarization, and the test of equal spin temperature theory.

Chapter 5 contains the technical aspects on the superconducting magnet system, the hardware of which the author was in charge. The magnet started its operation successfully in 2001 together with the entire apparatus of the polarized target. Since it is not appropriate to report all the details of its preparation and installation, the basic characteristics related to the operation and the protection of the hardware are reported.

Chapter 6 is the conclusions and outlook.

2. SPIN STRUCTURE OF THE NUCLEON

Why do you measure the gluon contribution to the nucleon spin? The answer is trivial, *It's not trivial to understand or predict the experimental data on the spin structure of the nucleon theoretically. And the spin is a fundamental quantity to characterize the particles.* This is a very short explanation of the motivation.

According to the angular momentum sum rule [8], the nucleon spin s_n can be decomposed into three parts

$$\frac{1}{2} = \frac{s_n}{\hbar} = \frac{1}{2}\Delta\Sigma + \Delta G + L \quad , \quad (2.1)$$

where $\Delta\Sigma$ is the contribution by the quark spin, ΔG is that by the gluon spin and L is the contribution of the orbital angular momentum of the quarks and gluons.

In this chapter, today's understanding on the spin structure, mainly on the quark spin contribution $\Delta\Sigma$, is reviewed since the experiments and the theories to date have extensively studied the contribution from the quarks $\Delta\Sigma$. As an analogy and a guide for the spin-dependent structure functions, the spin-independent structure functions are also discussed. The spin structure of the nucleon is discussed in the two theoretical frameworks, namely naive Parton Model and QCD evolved Parton Model.

2.1 Deep inelastic scattering

Deep inelastic scattering (DIS) is a process where the four-momentum of the mediating electroweak boson (γ , W^\pm , Z^0) is large enough to probe the substructure of a nucleon. The momentum transfer from the incoming particle and the break-up of the target nucleon leads to the notion of inelasticity.

In most DIS experiments, a charged lepton ℓ^\pm is scattered off a nucleon n to an outgoing lepton $\ell^{\pm'}$ and a hadronic final state X

$$\ell^\pm + n \rightarrow \ell^{\pm'} + X \quad . \quad (2.2)$$

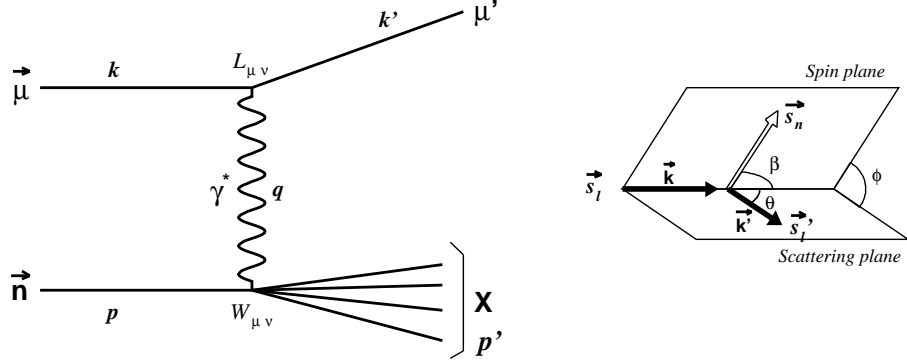


Fig. 2.1: (Left) Feynman diagram of DIS in the one-photon exchange process. (Right) Illustration of the angles in the lab frame.

In the lowest order perturbation theory, this process can be described by the exchange of a neutral boson (γ , Z^0). In COMPASS, the center-of-mass energy ($\sqrt{s} \sim \sqrt{2Em_n} \sim 14\text{-}20$ GeV) is well below the masses of the weak gauge bosons, the one-photon exchange process is the dominant process (Figure 2.1). The experiments so far shows the two-photon exchange process is negligible based on the study of the cross sections from the opposite charge leptons.

In the laboratory frame, the incoming lepton ℓ^\pm with a four momentum $k = (E, \vec{k})$ scatters at an angle θ with the outgoing momentum $k' = (E', k')$ by emitting a virtual photon γ^* . The four-momentum squared of the virtual photon is

$$q^2 = (k - k')^2 \quad . \quad (2.3)$$

Assuming the azimuthal symmetry and neglecting the lepton mass, the momentum transfer squared $Q^2 = -q^2$ is

$$Q^2 \stackrel{\text{lab}}{=} 4EE' \sin^2 \frac{\theta}{2} \quad , \quad (2.4)$$

where E (E') is the energy of incoming (outgoing) lepton. The Q^2 is the measure of the resolution with which the virtual photon can probe ($\lambda \sim 1/Q \sim 0.06$ fm for $Q^2 = 10 \text{ GeV}^2$). The energy transferred by the virtual

photon is

$$\nu = \frac{p \cdot q}{m_n} \stackrel{\text{lab}}{=} E - E' \quad . \quad (2.5)$$

At COMPASS, the target nucleon with mass m_n is at rest in the lab frame. The four-momentum p of the target nucleon is $p_{\text{lab}} = (m_n, \vec{0})$. Defining p' to be the sum of the four-momenta of the outgoing hadron fragments X , the invariant mass squared W^2 of the hadronic final state can be expressed as

$$W^2 = (p + q)^2 = p'^2 = m_n^2 + 2m_n\nu - Q^2 \quad . \quad (2.6)$$

DIS is considered as a process in which $1/Q$ is smaller than the size of the nucleon so that the leptons scatters off a single parton. Furthermore, W has to be more than 2 GeV to ensure the complete break-up of the nucleon instead of a hadronic resonance. As a common description, two dimensionless scaling variables are introduced,

$$y = \frac{p \cdot q}{pk} \stackrel{\text{lab}}{=} \frac{\nu}{E} \quad , \quad (2.7)$$

$$x = \frac{Q^2}{2p \cdot q} \stackrel{\text{lab}}{=} \frac{Q^2}{2m_n\nu} \quad (0 \leq x \leq 1) \quad . \quad (2.8)$$

The x is known as Bjorken's x and represents the momentum fraction carried by the parton in question. The variables defined in Equations (2.3)-(2.8) are Lorentz invariant. In a fixed target experiment, both x and y can be calculated from the kinematics of the outgoing lepton. This enables a structure measurement of the nucleon by detecting simply the scattered lepton, i.e. inclusive measurement.

2.2 Cross section and structure functions in unpolarized DIS

By evaluating the Feynman diagram in Figure 2.1, the inclusive DIS cross section can be written as a matrix product of the lepton tensor $L_{\mu\nu}$ and the hadron tensor $W^{\mu\nu}$ (see for instance [9, 10, 11]). The differential cross section in the lab frame is

$$\frac{d^2\sigma}{dE'd\Omega} = \frac{\alpha_e}{m_n Q^4} \frac{E'}{E} L_{\mu\nu} W^{\mu\nu} \quad , \quad (2.9)$$

where Ω is the solid angle in the lab frame. α_e is the fine structure constant (electromagnetic coupling constant) $\alpha_e = e^2/4\pi \sim 1/137$. The tensor $L_{\mu\nu}$ describes the interaction at the leptonic vertex in the one-photon exchange

and can be written with the gamma matrices γ_μ and spinor u of a positron or a positive muon (see for instance [12]),

$$L_{\mu\nu} = \sum_{s'_\ell} \bar{u}(k', s'_\ell) \gamma_\nu u(k, s_\ell) \bar{u}(k, s_\ell) \gamma_\mu u(k', s'_\ell) \quad . \quad (2.10)$$

The spin four-vector s'_ℓ of the incoming lepton is defined by

$$s'_\ell = \frac{1}{2} \bar{u}(k, s_\ell) \gamma^\nu \gamma^5 u(k, s_\ell) \quad (2.11)$$

and it can be set as $s'_\ell = (0, \vec{s}_\ell)$ in the rest frame of the incoming lepton. Employing trace theorem and summing over the unobserved spin orientations s'_ℓ of the final state, Equation (2.10) becomes

$$\begin{aligned} L_{\mu\nu} &= \text{Tr} \left[(\not{k}' + m_\ell) \gamma_\nu (\not{k} + m_e) \frac{m_\ell + \gamma^5 \not{s}'_\ell}{2m_\ell} \gamma_\mu \right] \\ &= 2(k'_\mu k'_\nu + k'_\nu k'_\mu - g_{\mu\nu} (k \cdot k' - m_\ell^2)) - i\epsilon_{\mu\nu\alpha\beta} q^\alpha s'^\beta_\ell \\ &\approx 2(k'_\mu k'_\nu + k'_\nu k'_\mu - g_{\mu\nu} k \cdot k' - i\epsilon_{\mu\nu\alpha\beta} q^\alpha s'^\beta_\ell) \\ &= L_{\mu\nu}^{(S)} - iL_{\mu\nu}^{(A)}, \end{aligned} \quad (2.12)$$

where the following definitions are used before the last line,

$$L_{\mu\nu}^{(S)} = 2(k'_\mu k'_\nu + k'_\nu k'_\mu - g_{\mu\nu} k \cdot k') \quad , \quad (2.13)$$

$$L_{\mu\nu}^{(A)} = 2\epsilon_{\mu\nu\alpha\beta} q^\alpha s'^\beta_\ell \quad . \quad (2.14)$$

The part $L_{\mu\nu}^{(S)}$ is symmetric in $\mu\nu$ and does not depend on the spin of the incident lepton while the other part $L_{\mu\nu}^{(A)}$ is antisymmetric and depends on the spin.

While the lepton tensor can be calculated analytically, the hadronic tensor $W^{\mu\nu}$ can not be calculated from the first principles. Experimental measurement is the only way to know the hadronic vertex information. In order to connect the theory to the experiment, a general expression for $W^{\mu\nu}$ was made based on the fact that it can only depend on p^ν , q^ν , and the polarization vector of spin- $\frac{1}{2}$ target s_n^ν . According to time-reversal invariance, parity conservation of the strong interaction, and the current conservation at the hadronic vertex, the hadronic tensor can be generally expressed as

$$W_{\mu\nu} = W_{\mu\nu}^{(S)} + W_{\mu\nu}^{(A)} \quad (2.15)$$

with

$$W_{\mu\nu}^{(S)} = F_1 \cdot \left(\frac{q_\mu q_\nu}{q^2} - g_{\mu\nu} \right) + F_2 \cdot \frac{1}{p \cdot q} \left(p_\mu - \frac{p \cdot q}{q^2} q_\mu \right) \left(p_\nu - \frac{p \cdot q}{q^2} q_\nu \right) , \quad (2.16)$$

$$W_{\mu\nu}^{(A)} = g_1 \cdot \frac{1}{p \cdot q} \epsilon_{\mu\nu\alpha\beta} q^\alpha s_n^\beta + g_2 \cdot \frac{1}{(p \cdot q)^2} \epsilon_{\mu\nu\alpha\beta} q^\alpha \left(p \cdot q s_n^\beta - s_n \cdot q p^\beta \right) . \quad (2.17)$$

F_1 , F_2 , g_1 and g_2 are called *structure functions* and they are generally the function of the proving scale Q^2 and the momentum fraction x of the involved parton in the scattering. The structure functions contain the actual information (distribution of partons) inside the nucleon while the other variables in Equations (2.16) and (2.17) can be determined by the kinematics of the incoming muon, outgoing muon, and the initial nucleon. Again, $W_{\mu\nu}^{(S)}$ is spin-independent and $W_{\mu\nu}^{(A)}$ is spin-dependent. For these reasons, F_1 and F_2 are referred as *unpolarized structure functions* or *spin-independent structure functions* and g_1 and g_2 as *polarized structure functions* or *spin-dependent structure functions*.

The unpolarized DIS cross section can be expressed as

$$\frac{d^2\sigma_{\text{unpol}}}{dE' d\Omega} = \frac{4\alpha_e^2 E'^2}{Q^4} \left(\frac{2F_1(x, Q^2)}{m_n} \sin^2 \frac{\theta}{2} + \frac{F_2(x, Q^2)}{\nu} \cos^2 \frac{\theta}{2} \right) . \quad (2.18)$$

A series of DIS experiments has mapped the structure function F_2 for the proton and the deuteron in a wide kinematic range of $10^{-3} < x < 0.9$ and $0.1 < Q^2 \text{ (GeV}^2) < 10^3$. A compilation of the world data can be found in Ref. [13]

2.3 Cross section and structure functions in polarized DIS

One way to measure the spin-dependent structure functions is to use the longitudinally polarized lepton beam and the polarized target. The difference of the cross section between the opposite target spin (\vec{s}_n and $-\vec{s}_n$) is (see for example, [14, 15])

$$\begin{aligned} & \frac{d^2\sigma(\beta)}{dE' d\Omega} - \frac{d^2\sigma(\beta + \pi)}{dE' d\Omega} \\ &= \frac{4\alpha_e^2}{Q^2 m_n \nu} \frac{E'}{E} \left[g_1(x, Q^2) \cdot (E \cos \beta + E' \cos \vartheta) \right] \end{aligned}$$

$$+g_2(x, Q^2) \cdot \frac{2EE'}{\nu} (\cos \vartheta - \cos \beta) \Big] \quad , \quad (2.19)$$

where $\cos \vartheta = \sin \theta \sin \beta \cos \phi + \cos \theta \cos \beta$ and β is the angle between the incoming lepton direction and the target spin \vec{s}_n (see Figure 2.1 (Right)) in the lab frame. The ϕ is the azimuthal angle ϕ between the scattering plane and the target polarization plane. From experimental point of view, the interesting and useful cases are $\beta = 0$ and $\beta = \pi/2$. In the case $\beta = 0$, the target spin is parallel ($\vec{\Rightarrow}$) or antiparallel ($\vec{\Leftarrow}$) to the beam spin, Equation (2.19) is simplified to

$$\frac{d^2 \Delta \sigma_{\parallel}}{dE' d\Omega} \equiv \frac{d^2 \sigma^{\vec{\Leftarrow}}}{dE' d\Omega} - \frac{d^2 \sigma^{\vec{\Rightarrow}}}{dE' d\Omega} = \frac{4\alpha_e^2}{Q^2 m_n \nu} \frac{E'}{E} \left[g_1 \cdot (E + E' \cos \theta) + g_2 \cdot \frac{Q^2}{\nu} \right] \quad . \quad (2.20)$$

In the case $\beta = \pi/2$, the target spin is perpendicular ($\vec{\Downarrow}$ or $\vec{\Uparrow}$) to the beam spin, Equation (2.19) becomes

$$\frac{d^2 \Delta \sigma_{\perp}}{dE' d\Omega} \equiv \frac{d^2 \sigma^{\vec{\Downarrow}}}{dE' d\Omega} - \frac{d^2 \sigma^{\vec{\Uparrow}}}{dE' d\Omega} = \frac{4\alpha_e^2}{Q^2 m_n \nu} \frac{E'^2 \sin \theta \cos \phi}{E} \left[g_1 + g_2 \cdot \frac{2E}{\nu} \right] \quad . \quad (2.21)$$

The cross section for $\beta = \pi/2$ depends on the azimuthal angle ϕ . And the spin-dependent cross section terms, Equation (2.20) and (2.21), make only a small contribution to the total cross section which is dominated by the unpolarized cross sections. For such reasons, the determination of g_1 and g_2 directly from Equations (2.20) and (2.21) is not practical.

The spin-dependent structure functions g_1 and g_2 has been determined from cross section asymmetries in conjunction with the approach of photon-nucleon Compton process. In the Weizsäcker-Williams approach [16, 17], the Feynman diagram in Figure 2.1 is viewed as the virtual photon absorption by the nucleon. The cross section can be factorized into two parts, a virtual photon flux $\Gamma(\nu, Q^2)$ emitted from the incoming lepton and the virtual photon absorption cross section. In this approach, the unpolarized DIS cross section can be expressed by the sum of the transverse virtual photon-nucleon DIS cross section $\sigma_T(x, Q^2)$ and the longitudinal one $\sigma_L(x, Q^2)$,

$$\begin{aligned} \frac{d^2 \sigma}{dE' d\Omega} &= \Gamma(\nu, Q^2) [\sigma_T(x, Q^2) + \epsilon \sigma_L(x, Q^2)] \\ &= \frac{\alpha_e^2 K}{2\pi^2 Q^2} \frac{E'}{E} \frac{1}{1 - \epsilon} [\sigma_T(x, Q^2) + \epsilon \sigma_L(x, Q^2)] \quad . \quad (2.22) \end{aligned}$$

The choice of factor K is not unique but is conventionally set to $K =$

$\nu - \frac{Q^2}{2m_n}$ [18]. The polarization parameter ε of the virtual photon is [19]

$$\varepsilon = \frac{1 - y - \frac{1}{4}\gamma^2 y^2}{1 - y + \frac{1}{4}y^2(\gamma^2 + 2)} \quad (2.23)$$

for the case $Q^2 \gg m_\ell^2$, where $\gamma^2 = Q^2/\nu^2$.

According to the optical theorem, the cross section of the photon absorption is related to the imaginary part of the forward Compton scattering $\gamma_h + N_H \rightarrow \gamma' + N_{H'}$, where h (h') and H (H') denotes the helicities of the photon and nucleon in the initial (final) state. The axis of quantization is chosen to be along the virtual photon's traveling direction. The cross section is proportional to the imaginary part of the helicity-dependent amplitude $M_{hH;h'H'}$ [11, 14],

$$\sigma_{\frac{1}{2}}^T \propto \frac{1}{2\pi} \text{Im}(M_{+1-\frac{1}{2};+1-\frac{1}{2}}) = F_1 + g_1 - \frac{4m_n^2 x^2}{Q^2} g_2 \quad , \quad (2.24)$$

$$\sigma_{\frac{3}{2}}^T \propto \frac{1}{2\pi} \text{Im}(M_{+1+\frac{1}{2};+1+\frac{1}{2}}) = F_1 - g_1 + \frac{4m_n^2 x^2}{Q^2} g_2 \quad , \quad (2.25)$$

$$\sigma_{\frac{1}{2}}^L \propto \frac{1}{2\pi} \text{Im}(M_{0\frac{1}{2};0\frac{1}{2}}) = -F_1 + \frac{F_2}{2x} \left(1 + \frac{4m_n^2 x^2}{Q^2}\right) \quad , \quad (2.26)$$

$$\sigma_{\frac{1}{2}}^{TL} \propto \frac{1}{2\pi} \text{Im}(M_{+1-\frac{1}{2};0-\frac{1}{2}}) = \frac{2m_n x}{Q} (g_1 + g_2) \quad . \quad (2.27)$$

The cross section $\sigma_{\frac{1}{2}}^T$ ($\sigma_{\frac{3}{2}}^T$) refers to the absorption of a transversely polarized photon by a nucleon which is longitudinally polarized in anti-parallel (parallel) to the photon's traveling direction. The third one $\sigma_{\frac{1}{2}}^L$ refers to that of a longitudinally polarized virtual photon. The last one $\sigma_{\frac{1}{2}}^{TL}$ is so-called interference term (single spin flip) and is suppressed by a factor $m_n x/Q$ compared to the others.

An interesting and commonly used ratio is

$$R(x, Q^2) = \frac{\sigma^L(x, Q^2)}{\sigma^T(x, Q^2)} = (1 + \gamma^2) \frac{F_2(x, Q^2)}{2xF_1(x, Q^2)} - 1 \quad , \quad (2.28)$$

where $\sigma^T = \frac{1}{2}(\sigma_{\frac{1}{2}}^T + \sigma_{\frac{3}{2}}^T)$ and $\sigma^L = \sigma_{\frac{1}{2}}^L$. In the limit of high Q^2 , the ratio $R_{DIS}(x, Q^2)$ is measured to go to zero [20, 21], which supports the Callan-Gross relation [22]

$$\lim_{Q^2 \rightarrow \infty} F_2(x) = 2xF_1(x) \quad . \quad (2.29)$$

The underlying reason of this relation is that the DIS in Figure 2.1 can be understood as the elastic scattering off a point-like spin- $\frac{1}{2}$ constituent of the nucleon.

With Equations (2.24)-(2.27), the the photoabsorption asymmetries A_1 and A_2 on the longitudinally and transversely polarized nucleon are

$$A_1(x, Q^2) = \frac{\sigma_T^{\frac{1}{2}} - \sigma_T^{\frac{3}{2}}}{\sigma_T^{\frac{1}{2}} + \sigma_T^{\frac{3}{2}}} = \frac{g_1 - \gamma^2 g_2}{F_1} \quad , \quad (2.30)$$

$$A_2(x, Q^2) = \frac{2\sigma_{TL}}{\sigma_T^{\frac{1}{2}} + \sigma_T^{\frac{3}{2}}} = \frac{\gamma(g_1 + g_2)}{F_1} \quad . \quad (2.31)$$

The experimentally observable asymmetries in lepton-nucleon scattering are

$$A_{\parallel} = \frac{\Delta\sigma_{\parallel}}{2\bar{\sigma}} \quad \text{and} \quad A_{\perp} = \frac{\Delta\sigma_{\perp}}{2\bar{\sigma}} \quad . \quad (2.32)$$

Here, $\Delta\sigma_{\parallel}$ and $\Delta\sigma_{\perp}$ are the short notations of the cross section differences in Equation (2.20) and (2.21), respectively. The notation $\bar{\sigma}$ denotes the unpolarized cross section in Equation (2.18). The experimental asymmetries A_{\parallel} and A_{\perp} are related to the photoabsorption cross sections A_1 and A_2 as

$$A_{\parallel} = D(A_1 + \eta A_2) \quad \text{and} \quad A_{\perp} = d(A_2 + \zeta A_1) \quad (2.33)$$

with the kinematic factors

$$\begin{aligned} D &= \frac{1 - \varepsilon \frac{E'}{E}}{1 + \varepsilon} \quad \text{and} \quad d = D \sqrt{\frac{2\varepsilon}{1 + \varepsilon}} \quad , \\ \eta &= \frac{\sqrt{Q^2}}{E - \varepsilon E'} \quad \text{and} \quad \zeta = \frac{\eta(1 + \varepsilon)}{2\varepsilon} \quad , \\ \varepsilon &= \frac{1}{1 + 2\left[1 + \frac{\nu^2}{Q^2}\right] \tan^2\left(\frac{\theta}{2}\right)} \quad . \end{aligned} \quad (2.34)$$

The mixture of the A_1 and A_2 originates from the fact that the emitted virtual-photons are not completely aligned. This complication has been solved as below. From Equations (2.30), (2.31) and (2.33) one can express A_1 in terms of g_1 and A_2 , then the following relation for the experimental longitudinal asymmetry can be found.

$$\frac{A_{\parallel}}{D} = (1 + \gamma^2) \frac{g_1}{F_1} + (\eta - \gamma) A_2 \quad . \quad (2.35)$$

The virtual photon asymmetries A_1 and A_2 are bound by the positive relations $|A_1| \leq 1$ and $|A_2| \leq \sqrt{R}$ [23, 24]. When the terms proportional to A_2 are neglected in Equations (2.33) and (2.35), which indeed justified experimentally, the A_1 and g_1 can be determined by the experimentally observable asymmetry A_{\parallel} by the relations

$$A_1 \simeq \frac{A_{\parallel}}{D}, \quad \frac{g_1}{F_1} \simeq \frac{1}{1 + \gamma^2} \frac{A_{\parallel}}{D} \quad . \quad (2.36)$$

The asymmetry A_2 can be decided from A_{\parallel} and A_{\perp} from

$$A_2 = \frac{1}{1 + \eta\zeta} \left(\frac{A_{\perp}}{d} + \zeta \frac{A_{\parallel}}{D} \right) \quad . \quad (2.37)$$

Then the g_2 can be decided from A_{\parallel} and A_{\perp} by Equations (2.30) and (2.31).

The measurements from the experiments at CERN (EMC and SMC), DESY (Hermes) and SLAC (E80, E130, E142, E143, and E154) has determined the structure function of proton g_1^p covering the kinematic range of $0.0001 < x < 0.8$ and $0.02 < Q^2(\text{GeV}^2) < 30$. A compilation of the world data can be found in Ref. [13]. The spin-dependent structure function g_2 has been measured on the proton and on the neutron in a kinematic range of $0.01 < x < 0.8$ and $1 < Q^2(\text{GeV}^2) < 30$. The A_2 has been measured and turned out to be very small and even consistent with zero [25, 26, 27, 28, 29].

2.4 Structure functions and spin puzzle in Parton Model picture

Historically, the baryon spectroscopy motivated the idea that the nucleon has 'internal' structure and its constituent partons are named 'quark'. The study of the unpolarized structure function F_1 and F_2 from DIS was the quantitative proof that the electrically and massively responsible constituent partons are indeed the quarks, i.e. point-like spin- $\frac{1}{2}$ fermion with the fractional electric charge ($2/3$ for u and $-1/3$ for d). This approach, *Parton Model* [30, 31], was taken for the study of the polarized structure functions, which should contain the internal spin information. These aspects are reviewed in this section. The Parton Model in this Section is sometimes referred as naive Parton Model because the roles of the strong field boson 'gluon' are not counted. However, the discussion here gives the basic ideas. The non-naive Parton Model, referred as QCD improved/evolved Parton Model or Parton Model with perturbative QCD, is presented in the next section.

2.4.1 Parton distribution

In the limit of high Q^2 and ν , the structure functions F_1 and F_2 become a function of only x . This phenomenon is called Bjorken scaling,

$$\lim_{Q^2, \nu \rightarrow \infty} F_{1,2}(x, Q^2) = F_{1,2}(x) \quad . \quad (2.38)$$

The underlying reason of this relation is that the DIS in Figure 2.1 can be understood as the elastic scattering off a point-like spin- $\frac{1}{2}$ constituent of the nucleon. This can be seen by comparing Equation (2.18) with the $e\text{-}\mu$ cross section (for example [10]) or inserting 'structure functions' for Dirac point particles (charge e_q) into Equation (2.18),

$$F_1^{\text{point}} = e_q^2 \frac{Q^2}{4m_n} \delta\left(\nu - \frac{Q^2}{2m^q}\right) = \frac{1}{2} e_q^2 x \delta\left(1 - \frac{x}{x_{\text{Bj}}}\right) \quad , \quad (2.39)$$

$$F_2^{\text{point}} = e_q^2 \nu \delta\left(\nu - \frac{Q^2}{2m^q}\right) = e_q^2 \delta\left(1 - \frac{x}{x_{\text{Bj}}}\right) \quad . \quad (2.40)$$

An intuitive understanding is that these partons carry a fraction x_{Bj} of the four-momentum of the nucleon $p_q = x_{\text{Bj}} p_n$ in the infinite momentum frame as shown in Figure 2.2 (Left). In the Parton Model, the partons are identified as the quarks in the nucleon. Such a parton picture allows the derivation of the four-momentum fraction that the struck quark carries in the nucleon from the kinematics of the scattered nucleon.

The Parton Model describes the deep inelastic scattering on a nucleon as incoherent elastic scattering on non-interacting point-like quarks. This picture leads to the definition of parton distribution function q_f for each quark (and antiquark) flavor f which assembles to F_2 when summed up,

$$F_2(x) = 2xF_1 = \sum_f e_f^2 x q_f(x) \quad , \quad (2.41)$$

where e_f is the electric charge of the quark flavor q_f . The formalism can be extended to the scattering of a polarized photon on a polarized quark (Figure 2.2 (Right)) . Helicity conservation dictates that the photon can be absorbed only by a quark with its spin opposite to the direction of the photon spin. Thus, by flipping the spin of the target, either the quarks with spin parallel $q^+(x)$ or anti-parallel $q^-(x)$ to the nucleon spin are selectively probed. The structure functions are written as follows in the Parton Model.

$$F_1(x) = \frac{1}{2} \sum_f e_f^2 \left(q_f^+(x) + q_f^-(x) + \bar{q}_f^+(x) + \bar{q}_f^-(x) \right)$$

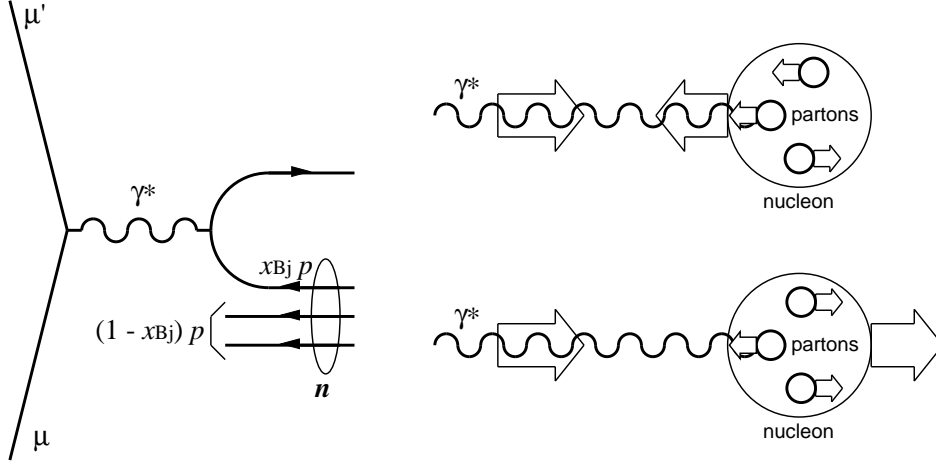


Fig. 2.2: (Left) DIS in the infinite momentum frame. The quark that carries the fraction x_{Bj} of the parent nucleon's momentum turns around when hit by the virtual photon. (Right) Polarized DIS in the infinite momentum frame. The polarized virtual photon hits a parton with spin parallel (top) or anti-parallel (bottom) to the nucleon spin, depending on the orientation of the target nucleon spin.

$$= \frac{1}{2} \sum_f e_f^2 (q_f(x) + \bar{q}_f(x)) \quad , \quad (2.42)$$

$$\begin{aligned} F_2(x) &= \sum_f e_f^2 x (q_f^+(x) + q_f^-(x) + \bar{q}_f^+(x) + \bar{q}_f^-(x)) \\ &= \sum_f e_f^2 x (q_f(x) + \bar{q}_f(x)) \quad , \end{aligned} \quad (2.43)$$

$$\begin{aligned} g_1(x) &= \sum_f e_f^2 (q_f^+(x) - q_f^-(x) + \bar{q}_f^+(x) - \bar{q}_f^-(x)) \\ &= \frac{1}{2} \sum_f e_f^2 \Delta q_f(x) \quad , \end{aligned} \quad (2.44)$$

$$g_2(x) = (\text{No transverse components in naive Parton Model.}) \quad , \quad (2.45)$$

where $q_f = q_f^+(x) + q_f^-(x)$ (*quark distribution function*) and $\Delta q_f = q_f^+(x) - q_f^-(x) + \bar{q}_f^+(x) - \bar{q}_f^-(x)$ (*polarized quark distribution function*). In the Parton Model, the integral of the quark density q_f in proton is normalized as

$$\int_0^1 dx (u(x) + \bar{u}(x)) = \int_0^1 dx u_v(x) = 2 \quad , \quad (2.46)$$

$$\int_0^1 dx (d(x) + \bar{d}(x)) = \int_0^1 dx d_v(x) = 1 \quad , \quad (2.47)$$

$$\int_0^1 dx (s(x) + \bar{s}(x)) = \int_0^1 dx s_v(x) = 0 \quad . \quad (2.48)$$

The functions $u_v(x)$, $d_v(x)$ and $s_v(x)$ are the distribution functions of the valence quarks (u , d , and s , respectively) inside a proton. The assumption of isospin symmetry between a proton and a neutron leads to the relations (the superscripts p and n denote a proton and a neutron, respectively)

$$u(x) \equiv u_p(x) = d_n(x) \quad , \quad (2.49)$$

$$d(x) \equiv d_p(x) = u_n(x) \quad , \quad (2.50)$$

$$s(x) \equiv s_p(x) = s_n(x) \quad . \quad (2.51)$$

The experiments have shown the quarks carry only a half of the nucleon momentum. The rest is considered to be carried by gluons,

$$\int_0^1 dx x \left[g(x) + \sum_f q_f(x) \right] = 1 \quad , \quad (2.52)$$

where $g(x) = g^+(x) + g^-(x)$ is the gluon density in the nucleon, which cannot be measured by the Feynman diagram in Figure 2.1

2.4.2 Spin puzzle in Parton Model picture

For the understanding of the spin structure of a nucleon, the Parton Model was first used for the data taken at CERN and SLAC. From experiments, one can calculate the first moment of the spin-dependent structure function g_1 for a proton and a neutron,

$$\Gamma_1^p \equiv \int_0^1 g_1^p dx = \frac{1}{2} \left(\frac{4}{9} \Delta u + \frac{1}{9} \Delta d + \frac{1}{9} \Delta u \right) \quad , \quad (2.53)$$

$$\Gamma_1^n \equiv \int_0^1 g_1^n dx = \frac{1}{2} \left(\frac{1}{9} \Delta u + \frac{4}{9} \Delta d + \frac{1}{9} \Delta u \right) \quad , \quad (2.54)$$

where $\Delta q_f = \int_0^1 \Delta q_f(x) dx$. From the view of naive Parton Model, the first moments can be expressed as

$$\Gamma_1^{p(n)} = \pm \frac{1}{12} a_3 + \frac{1}{36} a_8 + \frac{1}{9} a_0 \quad , \quad (2.55)$$

where a_0 , a_3 and a_8 are respectively the Gell-Mann SU(3) flavor singlet, octet isotriplet and octet isosinglet combinations of the first moments of the quark distributions

$$a_0 = \Delta u + \Delta d + \Delta s \quad , \quad (2.56)$$

$$a_3 = \Delta u - \Delta d \quad , \quad (2.57)$$

$$a_8 = \Delta u + \Delta d - 2\Delta s \quad . \quad (2.58)$$

(For the discussion of SU(3) symmetry applicability, see Ref. [32].) The values of a_3 and a_8 are known assuming the SU(3) assignments for the baryon octet [33]

$$a_3 = F + D \quad , \quad a_8 = \frac{1}{\sqrt{3}}(3F - D) \quad . \quad (2.59)$$

The hyperon beta decay data show [34]

$$F = 0.477 \pm 0.012 \quad , \quad D = 0.756 \pm 0.0011 \quad . \quad (2.60)$$

Solving the Equations (2.55)-(2.58) for the EMC results [4]

$$\Gamma_1^p = 0.128 \pm 0.013 \pm 0.019 \quad \text{at} \quad Q^2 = 10.7 \text{ GeV}^2 \quad (2.61)$$

leads to [35]

$$\Delta u = 0.79 \pm 0.03 \pm 0.04 \quad , \quad (2.62)$$

$$\Delta d = -0.47 \pm 0.06 \pm 0.04 \quad , \quad (2.63)$$

$$\Delta s = -0.26 \pm 0.06 \pm 0.09 \quad . \quad (2.64)$$

The quark contributions $\Delta\Sigma$ a to the nucleon spin is

$$\Delta\Sigma = a_0 = 0.06 \pm 0.12 \pm 0.17 \quad . \quad (2.65)$$

The prediction by the Parton Model is [61]

$$\Delta u = \frac{4}{3} \quad , \quad \Delta d = -\frac{1}{3} \quad , \quad \Delta s = 0 \quad , \quad \Delta\Sigma = 1 \quad . \quad (2.66)$$

A general remark is that Δu and Δd is qualitatively consistent in their signs and the size. However, the polarization of the strange quark is unexpected and the experimentally measured $\Delta\Sigma$ seems to be too small.

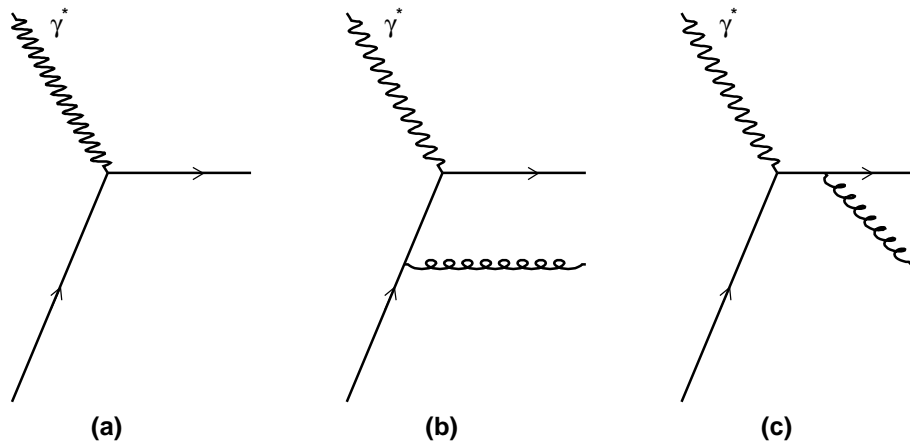


Fig. 2.3: Amplitudes of DIS off a quark.

2.5 Structure functions and spin puzzle in QCD evolved Parton Model

The structure of the nucleon cannot be explained without understanding the role of the gluon. The details of how the strong field quanta carry the momentum and the spin of the nucleon lead to deep insights of the mechanisms of the strong interactions. Experimental results is a test and an input for QCD which to date always turned out to be a correct framework in the fundamental sense but showed many difficulties in the practical calculations or predictions. In this section, the structure functions and the spin puzzle are discussed in the perturbative QCD framework.

2.5.1 Unpolarized structure functions

From the view of 'Parton Model + perturbative QCD', the DIS process can be considered as the interaction between a virtual photon and partons.

The Feynman diagrams of DIS off a quark are shown in Figure 2.3. The diagrams Figure 2.3 (b) and (c) involve the gluon emission from a quark, i.e. $\gamma^* + q \rightarrow g + q$. The squares of the Feynman diagrams of Figure 2.3 (b) and (c) are illustrated in Figure 2.4. In the calculation of the bare (a parton is considered as a target, rather than a proton) structure function \hat{F}_2 , the diagram of Figure 2.4 (a) gives the logarithmic infinite divergence and the diagrams of Figure 2.4 (b) (c) (d) give the finite corrections. The

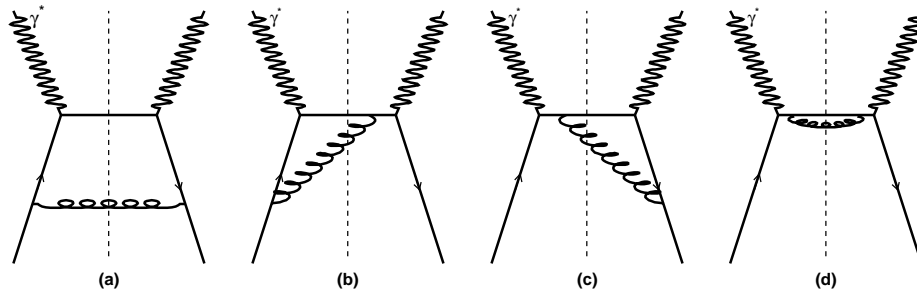


Fig. 2.4: Squares of the Feynman diagram involving real gluon emission.

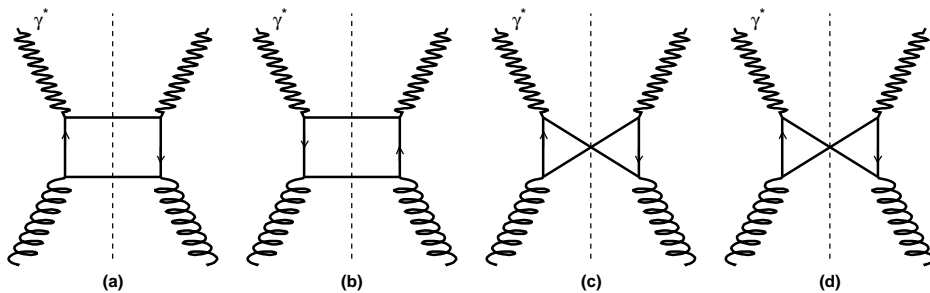


Fig. 2.5: Squares of the Feynman diagrams with a initial gluon.

logarithmic infinite divergence is caused by the quark with small transverse momentum ($k_T \rightarrow 0$), which has emitted the gluon parallel to the beam. The limit $k_T^2 \rightarrow 0$ corresponds to a long-range (soft) part of the strong interaction where one can not apply perturbation technique. Such a case is called *collinear divergence* or *collinear singularity*. One common approach to handle the collinear divergence is the dimensional regularization, which is a convenient method to handle ultraviolet divergences in the renormalization of the coupling constant.

One must also counts the virtual radiation, specifically the inclusion of self-energy insertions on the quark legs and the photon vertex correction. [36]

In order to obtain a complete description of the structure functions in terms of parton distributions, there is one further contributions which must be included, the $\mathcal{O}(\alpha_s)$ contributions from the $\gamma^*g \rightarrow q\bar{q}$ process shown in Figure 2.5. In this calculation, there is again a collinear singularity from

vanishing quark virtuality, $|k^2| \rightarrow 0$. The logarithmic infinite divergence can be handled in the same manner for that from Figure 2.4 (a).

From these considerations, the quark distribution functions $q(x, Q^2)$ and the structure function F_2 are expressed as (see for example [37])

$$\begin{aligned}
 q(x, \mu^2) = & q_0(x) + \frac{\alpha_s}{2\pi} \int_x^1 \frac{d\xi}{\xi} q(\xi, Q^2) q_0(\xi) \left[P_{qq}^{\overline{\text{MS}}} \left(\frac{x}{\xi} \right) \ln \frac{\mu^2}{\kappa^2} + C_q^{\overline{\text{MS}}} \left(\frac{x}{\xi} \right) \right] \\
 & + \frac{\alpha_s}{2\pi} \int_x^1 \frac{d\xi}{\xi} q(\xi, Q^2) g_0(\xi) \left[P_{qg}^{\overline{\text{MS}}} \left(\frac{x}{\xi} \right) \ln \frac{\mu^2}{\kappa^2} + C_g^{\overline{\text{MS}}} \left(\frac{x}{\xi} \right) \right] \\
 & + \dots \quad , \quad (2.67)
 \end{aligned}$$

$$\begin{aligned}
 F_2(x, Q^2) = & x \sum_{q, \bar{q}} e_q^2 \int_x^1 \frac{d\xi}{\xi} q(\xi, Q^2) \left[\delta \left(1 - \frac{x}{\xi} \right) + \frac{\alpha_s}{2\pi} C_q^{\overline{\text{MS}}} + \dots \right] \\
 & + x \sum_{q, \bar{q}} e_q^2 \int_x^1 \frac{d\xi}{\xi} g(\xi, Q^2) \left[\frac{\alpha_s}{2\pi} C_g^{\overline{\text{MS}}} + \dots \right] \quad . \quad (2.68)
 \end{aligned}$$

In analogy to the renormalization of the coupling constant, the collinear divergence is absorbed into the bare quark (gluon) distribution q_0 (g_0) at a 'factorization scale' μ . Here, κ is the cut-off parameter. The superscript $\overline{\text{MS}}$ refers to the *modified minimal subtraction scheme* discussed in Section 2.5.2.

The $P_{ab}(\frac{x}{\xi})$ are called *splitting functions*, which correspond to the probability that a parton a with momentum fraction x is radiated off from a parton b with momentum fraction ξ ($\xi > x$). The integrals above can be understood to collect all possibilities of a quark with momentum fraction x that could have emitted from another quark or gluon with momentum fraction from x to 1. The several splitting processes considered are illustrated in Figure 2.6

The functions C_q and C_g correspond to the finite contribution from the gluon emission process.

2.5.2 Factorization schemes

The ability to separate or factorize the long (collinear divergence) and short distance (finite) contributions to the physical quantity (e.g. parton distribution functions) is the property of the theory. The factorization provides a prescription for dealing with the logarithmic divergence and there is an arbitrariness in how the finite (short-distance) contributions are treated. How much finite contributions are factored out is called the *factorization*

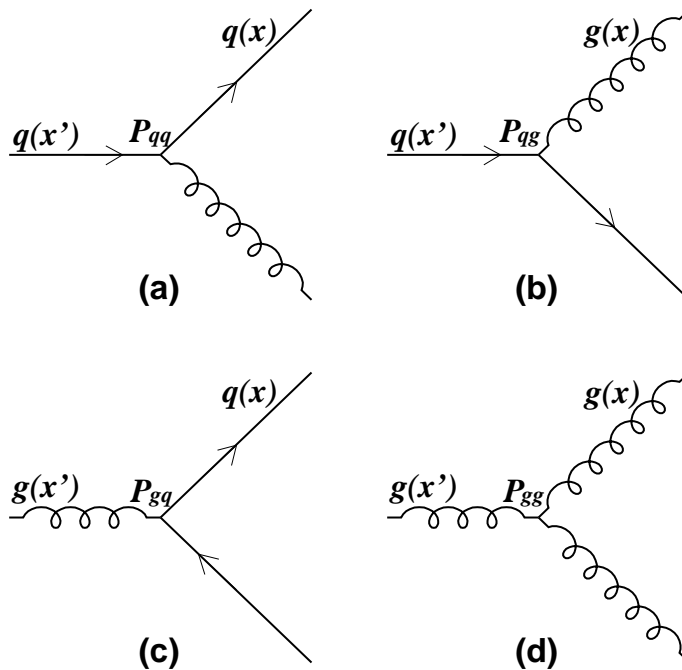


Fig. 2.6: Illustration of the QCD processes corresponding to the four splitting functions P_{qq} , P_{qg} , P_{gq} and P_{gg} . In each process, a parton with the momentum fraction x emerges from a parton with a larger momentum fraction ξ

scheme. One of the common choice is the $\overline{\text{MS}}$ (modified minimal subtraction) scheme [38, 39], where only the ubiquitous ' $\ln 4\pi - \gamma_E$ ' term (γ_E is the Euler constant), again in analogy to the renormalization of the coupling constant, is counted into C_q . The other choices are DIS scheme where all the gluon contribution is counted into the quark distribution and $F_2(x, Q^2) = x \sum_{q, \bar{q}} e_q^2 q(x, Q^2)$, AB scheme [40] and so on. It might at first sight appear that the arbitrariness in defining the factorization scheme removes the any predictive power from the theory, but this is not the case. Once one fixes the scheme, that scheme must be used in all the related calculations. Equivalently, one can in principle convert a certain quantity from one scheme to another.

In this thesis, $\overline{\text{MS}}$ scheme is used except in Section 2.6.2.

2.5.3 DGLAP equation and Scaling violation

The scaling of the parton distribution Eq. (2.38) as motivated by the naive Parton Model is only approximately true. As can be found in Ref. [13], the structure function F_2 varies slowly with Q^2 . This phenomena are called scaling violations, and can be explained in QCD by the interaction of quarks and gluons, and are in turn the input to understand the behavior of the gluon.

The evolution of the parton densities can be described by Dokshitzer-Gribov-Lipatov-Altarelli-Parisi (DGLAP) Equation which is a $(2n_f + 1)$ dimensional matrix equation in the space of quarks, antiquarks and gluons [36, 41, 42]

$$t \frac{\partial}{\partial t} \begin{pmatrix} q_i(x, t) \\ g(x, t) \end{pmatrix} = \frac{\alpha_s}{2\pi} \sum_j \int_x^1 \frac{d\xi}{\xi} \begin{pmatrix} P_{q_i q_j}(\frac{x}{\xi}, \alpha_s(t)) & P_{q_i g}(\frac{x}{\xi}, \alpha_s(t)) \\ P_{g q_j}(\frac{x}{\xi}, \alpha_s(t)) & P_{g g}(\frac{x}{\xi}, \alpha_s(t)) \end{pmatrix} \times \begin{pmatrix} q_j(\xi, t) \\ g(\xi, t) \end{pmatrix}, \quad (2.69)$$

where $t = Q^2$. The splitting functions in Eq. (2.69) can be expressed in an analytical expression at leading order and becomes dependent on the factorization scheme after next leading order (see for example [39, 43]).

A general remark on DGLAP equations is that they can describe the interconnection of the parton distributions but they cannot provide the absolute value on the actual parton distributions at a certain x and Q^2 without knowing the shape at some other Q^2 .

With an ansatz for the shape of the parton distributions and the splitting functions P_{ij} , the gluon density $g(x, Q^2)$ as well as the quark distribution can be retrieved via implicit fitting of Eq. (2.69) and the measured data on F_2 over a broad range in x and Q^2 [44]. The parton distributions are fixed at some arbitrary input scale Q_0^2 and then evolved to any given $Q^2 > Q_0^2$. It is found that the DGLAP evolution indeed matches the scaling violations observed, which in turn means DGLAP equation is the useful tool. There are a variety of fitting results [71, 46, 47, 48, 45, 49, 50]. The gluon density $g(x, Q^2)$ increases with higher Q^2 since more and more splittings in the parton cloud are resolved. For the same reason, $g(x, Q^2)$ increases rapidly when x approaches to 0. The accuracy of the gluon density obtained from fits to F_2 is limited due to the precision of the data and the systematic bias of the evolution analysis. The latter arises from the assumptions on the parton density shapes and higher order corrections.

2.5.4 Spin-dependent structure functions and polarized DGLAP equation

As has been seen for F_2 , the spin-dependent structure function g_1 also evolves with Q^2 .

$$\begin{aligned}
g_1(x, Q^2) &= \frac{1}{2} \sum_q e_q^2 \int_x^1 \frac{d\xi}{\xi} \Delta q\left(\frac{x}{\xi}, Q^2\right) \left[\delta(1-\xi) + \frac{\alpha_s}{2\pi} \Delta C_q(\xi) + \dots \right] \\
&\quad + \sum_q e_q^2 \int_x^1 \frac{d\xi}{\xi} \Delta g\left(\frac{x}{\xi}, Q^2\right) \left[\frac{\alpha_s(Q^2)}{2\pi} \Delta C_g(\xi) + \dots \right].
\end{aligned} \tag{2.70}$$

And its first moment becomes [51]

$$\begin{aligned}
\Gamma_1^{\text{p(n)}}(Q^2) &= \int_0^1 g_1^{\text{p(n)}}(x, Q^2) dx \\
&= \left[1 - \left(\frac{\alpha_s(Q^2)}{\pi}\right) - 3.58 \left(\frac{\alpha_s(Q^2)}{\pi}\right)^2 - 20.21 \left(\frac{\alpha_s(Q^2)}{\pi}\right)^3 + \dots \right] \\
&\quad \times \left(\pm \frac{1}{12} a_3 + \frac{1}{36} a_8 \right) \\
&\quad + \left[1 - \left(\frac{\alpha_s(Q^2)}{\pi}\right) - 1.09 \left(\frac{\alpha_s(Q^2)}{\pi}\right)^2 + \dots \right] \frac{1}{9} \Delta\Sigma(Q^2).
\end{aligned} \tag{2.71}$$

In other words, the experimentally measured $\Gamma_1^{\text{p(n)}}$ is not simple like Eq. (2.55) any more in the QCD picture. The experimental data with this perturbative corrections show

$$\Delta u = 0.83 \pm 0.03 \pm 0.03, \tag{2.72}$$

$$\Delta d = -0.43 \pm 0.06 \pm 0.03, \tag{2.73}$$

$$\Delta s = -0.10 \pm 0.06 \pm 0.03, \tag{2.74}$$

$$\tag{2.75}$$

and

$$\Delta\Sigma = \Delta u + \Delta d + \Delta s = 0.31 \pm 0.07 \tag{2.76}$$

at $Q^2 = 10 \text{ GeV}^2$ [52]. A general remark is that $\Delta\Sigma$ is increased with the perturbative corrections compared to the naive Parton Model analysis (Eq. (2.65)) but is still too small compared to the prediction by the naive Parton Model (Eq. (2.66)). Although there is no principal reason why $\Delta\Sigma$ should be unity, it seems unnatural that the quarks should carry so little of the nucleon spin. As one may think from the Equation (2.1), the gluons

as well as the angular momentum of the partons can carry a part of the nucleon spin.

The DGLAP equations for the evolution of the polarized quark and gluon distributions are

$$t \frac{\partial}{\partial t} \begin{pmatrix} \Delta q_i(x, t) \\ \Delta g(x, t) \end{pmatrix} = \frac{\alpha_s}{2\pi} \sum_j \int_x^1 \frac{d\xi}{\xi} \begin{pmatrix} \Delta P_{q_i q_j}(\frac{x}{\xi}, \alpha_s(t)) & \Delta P_{q_i g}(\frac{x}{\xi}, \alpha_s(t)) \\ \Delta P_{g q_j}(\frac{x}{\xi}, \alpha_s(t)) & \Delta P_{g g}(\frac{x}{\xi}, \alpha_s(t)) \end{pmatrix} \times \begin{pmatrix} \Delta q_j(\xi, t) \\ \Delta g(\xi, t) \end{pmatrix}. \quad (2.77)$$

The splitting functions ΔP_{ij} can be found in Ref. [36] at the leading order and in Ref. [53, 54, 55] at NLO. At NLO, the splitting functions are dependent on factorization scheme.

In analogy to the extraction of the unpolarized gluon density, the polarized quark densities $\Delta q_i(x, Q^2)$ and gluon density $\Delta g(x, Q^2)$ can in principle be derived from the scaling violations of g_1 , i.e. slow logarithmic evolution of g_1 with Q^2 . However, the polarized gluon density has not been clearly determined because the mapping of g_1 with Q^2 and x is still limited (see [13]) and the shape (x -dependence) of the polarized parton distributions are based on the assumption, especially at high x and small x . Overall, the polarized gluon density $\Delta g(x, Q^2)$ is not constrained at all [71, 46, 47, 48, 45, 50, 49].

2.6 Interpretation of small $\Delta\Sigma$. Is gluon contribution large?

The discussion in this section contains some speculations and assumptions to try to interpret the small $\Delta\Sigma$. The truth is that the spin puzzle is still a 'puzzle'.

The unexpectedly small $\Delta\Sigma$ gives rise to several questions,

- (a) The SU(3) Gell-Mann approach is really applicable?
- (b) As the nature of the QCD, the discussion at $\leq Q^2$ meaningful?
- (c) Is there any candidate to explain small $\Delta\Sigma$?

and so on. Concerning (a), the rigorous discussions can be found in Ref. [32]. A general remark is that there is no good reason to give up this approach, which is one of the basis of the today's Standard Model. And the experimental analysis for Δu , Δd (Eq. (2.72) and (2.73)) is not too far away from the expectation (Eq. (2.66)).

Concerning (b), it is true that QCD theory loses its power in the calculation. But the Bjorken sum rule discussed below shows that perturbative QCD is working within the theoretical/experimental errors.

Concerning (c), there are several theoretical models which can potentially accommodate the small $\Delta\Sigma$, for instance, Chiral soliton model sometimes referred as skyrmion model [56], the suppression of the QCD topological susceptibilities [57, 58, 59], and axial anomaly [62, 63, 64].

In this section, two sum rules are discussed for the understanding of the spin puzzle. Then, the idea of the axial anomaly is presented as one of the candidates which might explain the small $\Delta\Sigma$, since this idea gives an intuitive interconnection between the naive Parton Model and the gluon polarization and the axial anomaly seems to be supported by many researchers.

2.6.1 Sum rules

Bjorken Sum rule

Taking the difference between the first moment of a proton Γ_1^p and that of a neutron Γ_1^n gives the *Bjorken sum rule* [6, 7],

$$\Gamma_1^p - \Gamma_1^n = \frac{1}{6}(\Delta u + \Delta d) = \frac{1}{6}a_3 = \frac{1}{6} \left| \frac{g_A}{g_V} \right| . \quad (2.78)$$

where g_A and g_V are the axial- and vector-coupling constant respectively and those are measured by the neutron and hyperon β decay. In perturbative QCD, one must apply the corrections [60]

$$\begin{aligned} \Gamma_1^p(Q^2) - \Gamma_1^n(Q^2) &= \frac{1}{6} \left| \frac{g_A}{g_V} \right| \left[1 - \frac{\alpha_s(Q^2)}{\pi} + \left(\frac{\alpha_s(Q^2)}{\pi} \right)^2 \left\{ -\frac{55}{12} + n_f \frac{1}{3} \right\} \right. \\ &\quad + \left(\frac{\alpha_s(Q^2)}{\pi} \right)^3 \left\{ -\frac{13841}{216} - \frac{44}{9} \zeta(3) + \frac{55}{2} \zeta(5) \right. \\ &\quad \left. \left. + n_f \left(\frac{10339}{1296} + \frac{61}{54} \zeta(3) + \frac{5}{3} \zeta(5) \right) - n_f^2 \frac{115}{648} \right\} \right] . \end{aligned} \quad (2.79)$$

In the Bjorken sum rule, the gluon contribution cancels. The Bjorken sum rule with the perturbative correction is consistent with the experimental data. (Or in other words, solving the Eq. (2.79) for the experimental data gives $\alpha_s(2.5\text{GeV}^2) = 0.375_{-0.081}^{+0.062}$ which evolves to $\alpha_s(M_Z) = 0.122_{-0.009}^{+0.005}$ [52]. This value is inside the variation of the world data on α_s which were decided by the various processes [13].) The validity of the Bjorken sum rule probably

means that the spin balance between Δu and Δd can be understood in the framework of 'Gell-Mann SU(3) approach + perturbative QCD'.

Ellis-Jaffe sum rule

The *Ellis-Jaffe sum rule* [5] is the prediction for the first moment of g_1 , assuming $\Delta s = 0$ and SU(3) symmetry. In the naive Parton Model, the heart of the Ellis-Jaffe sum rule has already appeared in the context above (Eq. (2.53) and (2.53)) and its numerical predictions are

$$\Gamma_1^p = 0.185 \pm 0.003 \quad , \quad (2.80)$$

$$\Gamma_1^n = -0.024 \pm 0.003 \quad . \quad (2.81)$$

One of the compiles of the experimental measurements [61] gives

$$\Gamma_1^p = 0.142 \pm 0.008(stat.) \pm 0.011(sys.) \quad (Q^2 = 10 \text{ GeV}^2) \quad . \quad (2.82)$$

The prediction by the Ellis-Jaffe sum rule is larger than the experimental data. Even applying the perturbative QCD correction to the Ellis-Jaffe sum rule as in Eq. (2.71), the measured value is still below the theoretical predictions.

The possible explanation for the discrepancy even after perturbative QCD corrections is that not only gluons but also the strange quark might have a subtle contributions. Indeed, the Gell-Mann SU(3) approach analysis with the experimental data shows that $\Delta s = -0.10 \pm 0.06 \pm 0.03$ at $Q^2 = 10 \text{ GeV}^2$ (Eq. (2.74)), which is not consistent with the assumption of the Ellis-Jaffe sum rule. The reason the s quark has a finite negative spin contribution is still not clear.

2.6.2 Axial anomaly

Axial anomaly is one of the candidates to explain the unexpectedly small $\Delta\Sigma$. In this section, the idea and the outline of the axial anomaly is presented in AB scheme. A rigorous discussion can be found for example in Ref. [62, 63, 64].

While the first moment of g_1 which is the spin structure of the proton can be understood in the terms of the Gell-Mann SU(3) matrices (Eq. (2.55)) in naive Parton Model, the identification of a_0 with $\Delta\Sigma$ (the sum of quark contribution to the nucleon spin) is not straightforward in QCD because of so-called *axial anomaly*. The axial anomaly was originally found in QED calculations by Adler, Bell and Jackiw [65, 66].

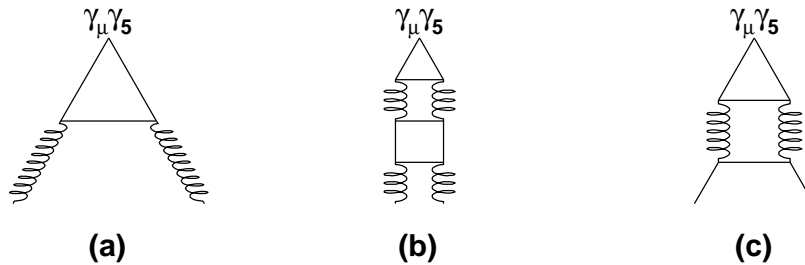


Fig. 2.7: (a) Triangle Diagram giving causing the axial anomaly. (b) Diagram causing to the renormalization of the axial anomaly. (c) Diagram causing the renormalization of the axial current.

The axial current operator J_5 is defined as

$$J_5^{k\mu} = \frac{1}{2} \bar{\psi}_i \gamma^\mu \gamma^5 \lambda_k^{ij} \psi_j , \quad k = 0, 1, \dots, 8 \quad , \quad (2.83)$$

where $\lambda_k^{ij} = \delta^{ij} / \sqrt{6}$ are the SU(3) generator matrices in Gell-Mann representation and ψ describes the quark field. $J_5^{k\mu}$ expresses the quark spin state, in analogy to QED (see Eq. (2.11)). The axial current a_k , which is Lorentz invariant scalars, is proportional to the expectation value of the axial-vector currents J_5 ,

$$a_k = \frac{\langle p_n, s_n | J_5^{k,\mu} | p_n, s_n \rangle}{(1 + \delta_{0i}) s_n^\mu m_n} , \quad (2.84)$$

for a proton with four-vector p_n and the spin vector s_n .

In naive Parton Model where the quarks are free and their interaction is not considered, the Dirac equation of motion is

$$\partial^\mu J_{5\mu}^f = 2im_q \bar{\psi}_f \gamma_5 \psi_f \quad (m_q : \text{quark mass}) \quad . \quad (2.85)$$

In the chiral limit $m_q \rightarrow 0$, $J_{5\mu}^f$ is conserved. However, $J_{5\mu}^f$ is not conserved once the triangle interaction of quarks via bosons, Figure 2.7 (a), is taken into account,

$$\partial^\mu J_{5\mu}^f = \frac{\alpha_s(Q^2)}{8\pi} G^{a\mu\nu} \epsilon_{\mu\nu\rho\sigma} G_a^{\rho\sigma} \neq 0 \quad , \quad (2.86)$$

where G^a is the strong tensor and a is the color index. The non-conservation of $J_{5\mu}^f$ is the source of the term *anomaly*. The result of Eq. (2.86) is multiplied

by

$$T\left(\frac{m_q^2}{q_g^2}\right) = 1 - \frac{2m_q^2/q_g^2}{\sqrt{1+4m_q^2/q_g^2}} \ln\left(\frac{\sqrt{1+4m_q^2/q_g^2}+1}{\sqrt{1+4m_q^2/q_g^2}-1}\right) . \quad (2.87)$$

where q_g is the four-momentum of the gluon. The anomaly manifests itself ($T \rightarrow 1$) for the off-shell gluon ($m_q^2/q_g^2 \rightarrow 0$) while it does not ($T \rightarrow 0$) for the on-shell gluon ($m_q^2/q_g^2 \rightarrow 1$). Counting the off-shell gluon in the calculation of the matrix element a_0 ($J_{5\mu}^0$), one obtains the contribution from the gluons as well as that of the quarks,

$$\langle q_g, h_g | J_{5\mu}^f | q_g, h_g \rangle = \frac{i\alpha_s}{2\pi} \epsilon_{\mu\nu\rho\sigma} q_g^\nu \epsilon^{*\rho}(h_g) \epsilon^\sigma(h_g) T(m_q^2/q_g^2) , \quad (2.88)$$

where h_g is the gluon helicity and one may take

$$S_\mu^g(q_g, h_g) \approx h_g q_{g\mu} \quad (2.89)$$

as the spin vector of the nearly massless gluons. The calculation of the gluon contribution to the hadronic expectation value $\langle P, S | J_{5\mu}^0 | P, S \rangle$ (P stands for the proton state) with

$$T = 1 \quad \text{for } u, d, s \quad \text{and} \quad T = 0 \quad \text{for } c, t, d \quad (2.90)$$

Eq. (2.88) results in the relation

$$a_0^{gluons}(Q^2) = -3 \frac{\alpha_s}{2\pi} \int_0^1 dx \Delta g(x, Q^2) = -3 \frac{\alpha_s}{2\pi} \Delta g(Q^2) . \quad (2.91)$$

One may rewrite a_0 as

$$\Delta \Sigma^{\text{exp}} = a_0(Q^2) = \Delta \Sigma^{\text{AB}} - \frac{n_f \alpha_s(Q^2)}{2\pi} \Delta g^{\text{AB}}(Q^2) , \quad (2.92)$$

where n_f is the number of the considered quark flavors ($n_f = 3$). In this picture, a_0 is modified by an anomalous gluon contribution which is proportional to $\Delta g(Q^2)$. Thus, the smallness of the measured value of $\Delta \Sigma^{\text{exp}}$ could be explained by a positive value of Δg .

Although the consideration above was for the triangle diagram Figure 2.7 (a), it has been proved that the anomaly result is not influenced by higher order corrections [65, 67]. The 3-loop diagram of Figure 2.7 (b) effectively multiplies the anomaly result by a cut-off dependent constant. But this constant is the same as the one shown by Adler to renormalize $J_{5\mu}^0$ via

Figure 2.7 (c). Consequently, the Eq. (2.86) and (2.92) are unchanged in analogy to the QED discussion [65, 66, 68].

The discussion in this section is scheme dependent and the equations in this section is given in AB scheme, where the off-shell gluons are separated from the quarks [65, 66]. In AB scheme, $\Delta\Sigma^{\text{AB}}$ is independent of Q^2 and should correspond to the value expected in the naive Parton Model, i.e. $\Delta\Sigma^{\text{AB}} = 1$. In $\overline{\text{MS}}$ scheme, that the gluon anomaly is 'absorbed' into $\Delta\Sigma^{\overline{\text{MS}}}$ and does not explicitly appear,

$$\Delta\Sigma^{\text{exp}} = a_0^{\overline{\text{MS}}}(Q^2) = \Delta\Sigma^{\overline{\text{MS}}}(Q^2) \quad . \quad (2.93)$$

The general remark is that the axial anomaly tells that quarks do not have to carry the entire nucleon spin. However, the analysis with the experimental data to date does not quantitatively solve the spin puzzle because of the systematic bias in the analysis models and the limited range of data.

3. COMPASS EXPERIMENT

The EMC results [3, 4] that the quarks carry unexpectedly small fraction of the nucleon spin led to the extensive experimental and theoretical works. The precise measurements by SMC at CERN, a series of experiments at SLAC, and HERMES at DESY with perturbative QCD analysis show that the quarks carry 20-30 % of the parent nucleon spin at $Q^2 = 10 \text{ GeV}^2$, as has been seen in Chapter 2. Following these results, the gluon spin is considered to be one of the candidates to explain the missing spins and various theoretical models and parameterizations have been developed. However, the polarized gluon distribution function $\Delta g(\eta, Q^2)$ is hardly constrained, as some of them are shown in Figure 3.1. In order to clarify the spin structure of the nucleon, the direct experimental measurements of Δg is awaited.

One of the main goals of the COMPASS experiment is to measure $\Delta g/g$. In this chapter, how the COMPASS experiment can access the gluon polarization is presented. The expected accuracy is shown and is compared with those of the other experiments. Then, the experimental setup of the COMPASS experiment is described in the general terms.

In this chapter, the positive sign of the helicity corresponds to the traveling direction of the muon beam unless stated.

3.1 Open charm lepto-production via photon-gluon fusion

One of the direct methods to measure the gluon polarization $\Delta g/g$ in the nucleon is to study the open charm leptonproduction (OCLP) via photon-gluon fusion (PGF) process, as suggested by Ref. [63, 69]. The COMPASS experiment explores $\Delta g/g$ with this method. The leading order Feynman diagram is shown in Figure 3.1. In this process, a charm-anticharm pair is produced in back-to-back in the center of mass system of the photon and the gluon. As the PGF process was first suggested by Babcock, Siverson and Wolfram [70] in order to explain the charm production by QCD effect, this process is a clean channel. In the COMPASS experiment, a virtual photon emitted from the longitudinally polarized positive muon beam interacts with a gluon in a nucleon in the fixed, longitudinally polarized target. The

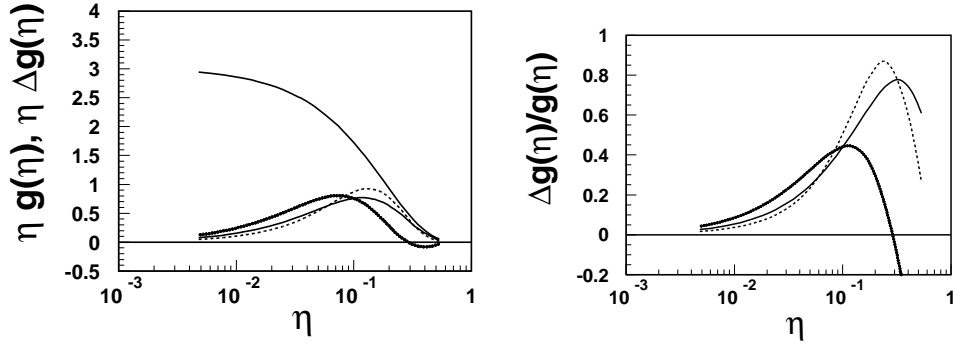


Fig. 3.1: Example of the possible shapes of the polarized gluon distribution function as a function of the gluon momentum fraction η from Ref. [71]: set A (solid), B (dashed), and C (thick). (Left) $\eta\Delta G(\eta)$, together with $\eta g(\eta)$ from Duke & Owens set 1.1 (upper curve). (Right) $\Delta g(\eta)/g(\eta)$.

quantity to determine is the double spin asymmetry of OCLP

$$A^{\mu n \rightarrow c\bar{c}X} = \frac{\sigma_{c\bar{c}}^{\rightarrow\leftarrow} - \sigma_{c\bar{c}}^{\leftarrow\leftarrow}}{\sigma_{c\bar{c}}^{\rightarrow\leftarrow} + \sigma_{c\bar{c}}^{\leftarrow\leftarrow}}, \quad (3.1)$$

where $\sigma_{c\bar{c}}^{\rightarrow\leftarrow}$ ($\sigma_{c\bar{c}}^{\leftarrow\leftarrow}$) is the cross section of OCLP in the antiparallel (parallel) spin configuration between the beam and the target. The double spin asymmetry in Eq. (3.1) is related to the experimentally measurable double spin asymmetry

$$A^{\text{exp}} = \frac{N_{c\bar{c}}^{\rightarrow\leftarrow} - N_{c\bar{c}}^{\leftarrow\leftarrow}}{N_{c\bar{c}}^{\rightarrow\leftarrow} + N_{c\bar{c}}^{\leftarrow\leftarrow}} \quad (3.2)$$

by the relation

$$A^{\text{exp}} = P_B P_T f A^{\mu n \rightarrow c\bar{c}X}, \quad (3.3)$$

where $N_{c\bar{c}}^{\rightarrow\leftarrow}$ ($N_{c\bar{c}}^{\leftarrow\leftarrow}$) is the counting rate of OCLP in the antiparallel (parallel) spin configuration, P_B is the beam polarization, P_T is the target polarization and f is the dilution factor discussed in Section 4.4.1.

How $\Delta g/g$ can be extracted from the double spin asymmetry $A^{\mu n \rightarrow c\bar{c}X}$ is presented in the rest of the section. The variables involved in this section is summarized in Appendix A.

The polarized cross sections of OCLP, $\sigma_{c\bar{c}}^{\rightarrow\leftarrow}$ and $\sigma_{c\bar{c}}^{\leftarrow\leftarrow}$, can be expressed as a convolution of the PGF subprocess cross section $d\hat{\sigma}$ and the gluon

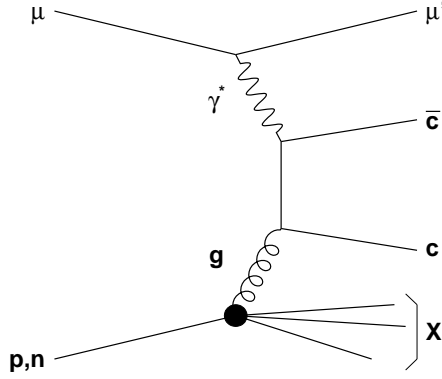


Fig. 3.2: The leading order Feynman diagram of open charm lepton production via photo-gluon fusion.

distribution function $g(\eta, \hat{s})$,

$$\sigma_{c\bar{c}}^{\leftrightarrow} = f_{-/-} d\hat{\sigma}^{-+} g_{+/+} + f_{-/-} d\hat{\sigma}^{--} g_{-/+} + f_{+/-} d\hat{\sigma}^{++} g_{+/+} + f_{+/-} d\hat{\sigma}^{+-} g_{-/+} \quad , \quad (3.4)$$

$$\sigma^{\uparrow\uparrow} = f_{-/-} d\hat{\sigma}^{--} g_{-/-} + f_{-/-} d\hat{\sigma}^{-+} g_{+/-} + f_{+/-} d\hat{\sigma}^{+-} g_{-/-} + f_{+/-} d\hat{\sigma}^{++} g_{+/-} \quad . \quad (3.5)$$

Here, $d\hat{\sigma}^{ab}$ is the cross section of the PGF subprocess $\gamma^* g \rightarrow c\bar{c}$ in the spin configuration a and b , where a (b) is the sign of the virtual photon helicity (the gluon helicity). By parity, $d\hat{\sigma}^{++} = d\hat{\sigma}^{--}$ and $d\hat{\sigma}^{+-} = d\hat{\sigma}^{-+}$. The variable $g_{a/b}(\eta, \hat{s})$ is the gluon density function for the spin configuration a and b , where a is the sign of gluon helicity inside the nucleon with the sign b . g is the function of the probe energy \hat{s} as well as the gluon momentum fraction η . By parity, $g_{+/+} = g_{-/-}$ and $g_{-/+} = g_{+/-}$.

The function $f_{\lambda_{\gamma^*}/\lambda_{\mu}}$ corresponds to the virtual photon intensity by the muon bremsstrahlung according to

$$f_{\lambda_{\gamma^*}/\lambda_{\mu}}(\nu, E_{\mu}) = \frac{\alpha_e}{4\pi} \left[\frac{1 + (1-y)^2}{y} + \lambda_{\gamma^*} \lambda_{\mu} \frac{1 - (1-y)^2}{y} \right] \cdot \ln \frac{E_{\mu}^2}{m_{\mu}^2} \quad , \quad (3.6)$$

where λ_{γ^*} and λ_{μ} is the sign of the virtual photon helicity and that of muon, respectively.

The cross sections $d\hat{\sigma}^{ab}$ can be calculated in the laboratory (nucleon rest) frame [72]. The gluon is taken as on-shell ($q_g^2 = 0$). It is assumed that an

off-shell gluon contribution would be suppressed by the propagator [73]. As a high energy approximation, the muon mass is neglected and the quark mass is retained.

$$\frac{d\hat{\sigma}^{\lambda_\gamma^* \lambda_g}}{dQ^2 dv d\phi} = e_c^2 \frac{\alpha_s \alpha_e}{4\pi} \frac{1}{SQ^2 E_\mu} \int d\beta g \frac{4m_c^2 + Q^2(1 - \beta^2)}{2\nu m_n(1 - \beta^2)} \frac{8m_c^2 |M|^2}{(4m_c^2 + Q^2(1 - \beta^2))^2} , \quad (3.7)$$

where the amplitude squared $|M|^2$ is given as

$$\begin{aligned} |M|^2 = & \frac{1}{1 - \varepsilon} \left[(1 + \varepsilon \cos 2\phi) \left[\frac{16m_c^2}{W} \beta (Q^2 - 2m_c^2) \right. \right. \\ & \left. \left. + \left(\frac{16m_c^4(3 + \beta^2)}{W} - 8m_c^2 \right) \ln \frac{(1 + \beta)}{(1 - \beta)} \right] \right. \\ & + 2\lambda_{\gamma^*} \lambda_g \frac{\sqrt{1 - \varepsilon^2}}{(1 - \beta^2)} \left[\left(4m_c^2 - Q^2(1 - \beta^2) \right) \ln \frac{(1 + \beta)}{(1 - \beta)} \right. \\ & \left. \left. - 12\beta m_c^2 + Q^2 \beta (1 - \beta^2) \right] \right. \\ & + \frac{4\varepsilon Q^2}{W} \left[12m_c^2 \beta - 2m_c^2(3 - \beta^2) \ln \frac{(1 + \beta)}{(1 - \beta)} \right] \\ & - \frac{4Q^2(1 - \varepsilon)}{W} \left[2m_c^2(1 + \beta^2) \ln \frac{(1 + \beta)}{(1 - \beta)} - 4m_c^2 \beta \right] \\ & \left. + \frac{2W}{(1 - \beta^2)} \left[\ln \frac{(1 + \beta)}{(1 - \beta)} - \beta \right] \right] . \quad (3.8) \end{aligned}$$

Here, ε is the polarization parameter of the virtual photon Eq. (2.23) and S is the center of mass energy of the muon and the nucleon $S = (k + p_n)^2$. The cross sections $d\hat{\sigma}^{ab}$ decrease very rapidly with Q^2 due to the photon propagator and it is encouraging to concentrate on the pure or quasi-real photoproduction situation ($Q^2 \sim 0$). Then the cross sections $d\hat{\sigma}^{ab}$ can be expressed in a rather simpler way. The spin averaged cross section $d\hat{\sigma}^{ab}$ and the difference of the polarized cross sections $\Delta d\hat{\sigma}^{ab}$ are

$$d\hat{\sigma} \equiv \frac{1}{2}(d\hat{\sigma}^{-+} + d\hat{\sigma}^{--}) = \frac{4}{9} \frac{2\pi\alpha_e\alpha_s(\hat{s})}{\hat{s}} \left[\beta(2 - \beta^2) + \frac{1}{2}(3 - \beta^4) \ln \frac{1 + \beta}{1 - \beta} \right] , \quad (3.9)$$

$$\Delta d\hat{\sigma} \equiv (d\hat{\sigma}^{-+} - d\hat{\sigma}^{--}) = \frac{4}{9} \frac{2\pi\alpha_e\alpha_s(\hat{s})}{\hat{s}} \left[3\beta - \ln \frac{1 + \beta}{1 - \beta} \right] . \quad (3.10)$$

By employing the conventional definitions,

$$\bar{f} \equiv f_{-/-} + f_{+/-} , \quad (3.11)$$

$$\Delta f \equiv f_{-/-} - f_{+/-} \quad , \quad (3.12)$$

$$D \equiv \frac{\Delta f}{f} = \frac{1 + (1 - y)^2}{1 + (1 + y)^2} \quad , \quad (3.13)$$

$$g \equiv g_{+/+} + g_{-/+} \quad , \quad (3.14)$$

$$\Delta g \equiv g_{+/+} - g_{-/+} \quad , \quad (3.15)$$

the double spin asymmetry Eq. (3.1) becomes

$$A^{\mu n \rightarrow c\bar{c}X} = D(y) \frac{\Delta g(\eta, \hat{s}) \Delta d\hat{\sigma}(\hat{s})}{g(\eta, \hat{s}) d\hat{\sigma}(\hat{s})} \quad . \quad (3.16)$$

In the real experiments, one can not select a monochromatic \hat{s} value or y value. The observed counting rates are the integrated ones over \hat{s} and the averaged ones over the virtual photon intensity y , i.e.

$$A^{\mu n \rightarrow c\bar{c}X} = \bar{D} \frac{\int_a^b \Delta g(\eta, \hat{s}) \Delta d\hat{\sigma}(\hat{s}) d\hat{s}}{\int_a^b g(\eta, \hat{s}) d\hat{\sigma}(\hat{s}) d\hat{s}} \quad , \quad (3.17)$$

with

$$\eta \equiv \hat{s}/s = 2m_n E_\gamma = \hat{s}/(2m_n E y) \quad , \quad (3.18)$$

$$a = m_{J/\psi}^2 \quad , \quad b = (2m_D)^2 \quad , \quad (3.19)$$

for the study of the lowest state of $c\bar{c}$. With local approximation [74], the convoluted integrations in Eq. (3.17) can be avoided,

$$A^{\mu n \rightarrow c\bar{c}X} \simeq \bar{D} \frac{\int_a^b d\hat{s} \Delta \hat{\sigma}(\hat{s})}{\int_a^b d\hat{s} \hat{\sigma}(\hat{s})} \frac{\Delta g(m_{c\bar{c}}^2/s', m_{c\bar{c}}^2)}{g(m_{c\bar{c}}^2/s', m_{c\bar{c}}^2)} \quad , \quad (3.20)$$

where s' is the center of mass energy of the virtual photon and the nucleon $s' = 2m_n E_\gamma = 2m_n E_\mu y$. From this relation, one can extract $\Delta g/g$.

3.2 Expectations

In the COMPASS experiment, the evaluation of the counting rate of OCLP $N_{c\bar{c}}^{\rightarrow\rightarrow}$ ($N_{c\bar{c}}^{\leftarrow\leftarrow}$) is based on the invariant mass reconstruction of the short life time hadrons which contain charm flavor. In this section, the expected statistical accuracy is shown. The details of the Monte Carlo simulation can be found in Ref. [75].

3.2.1 Luminosity

The number of the scattering centers in the target, i.e. number of the nucleons there, intercepted by the beam is

$$N_{\text{sc}} = \frac{S\ell\kappa\rho N_A N_n}{M_m} = 2.6 \times 10^{26} \quad , \quad (3.21)$$

for the target cell with a cross section $S = \pi \cdot (0.015 \text{ m})^2$ and a length $\ell = 2 \times 0.6 \text{ m}$, target material (${}^6\text{LiD}$) density $\rho = 0.84 \cdot 10^3 \text{ kg/m}^3$, target packing factor $\kappa = 0.6$, Avogadro number $N_A = 6.0 \cdot 10^{23}$, number of nucleons per unit molecule $N_n = 8$, and molecular weight of the unit molecule $M_m = 8.0 \cdot 10^{-3} \text{ kg}$.

The beam intensity is $I_B = 2 \cdot 10^8 \text{ muons/spill}$, corresponding to $I_B = 1.2 \cdot 10^{12} \text{ muons/day}$ for the case that the accelerator cycle is 14.4 seconds. The beam flux F_B is

$$F_B = \frac{I_B}{S} = 1.6 \cdot 10^{11} \text{ muons cm}^{-2} \text{ day}^{-1} \quad . \quad (3.22)$$

The luminosity \mathcal{L} is

$$\mathcal{L} = F_B N_{\text{sc}} = 4.3 \cdot 10^{37} \text{ cm}^{-2} \text{ day}^{-1} \quad . \quad (3.23)$$

Taking into account an estimated combined efficiency of 0.25 for the accelerator operation, the spectrometer, and the reconstruction efficiency, the effective luminosity is $\mathcal{L} = 1.6 \text{ fb}^{-1}/\text{year}$ for the accelerator operation of 150 days/year.

3.2.2 Reconstruction of the open charm events

In Table 3.2.2, summarized are the cross sections of the open charm photo-production and the total DIS cross section of a photon. These cross sections are based on the measurements in Ref. [76].

ν GeV	$\sigma^{c\bar{c}}$ nb	Q_{\min}^2 GeV ²	Q_{\max}^2 GeV ²	$\Delta\nu \int_{Q_{\min}^2}^{Q_{\max}^2} \frac{d\sigma^{c\bar{c}}}{dQ^2 d\nu} dQ^2$ nb	D	$\int \sigma_{\gamma}$ μb	$R = \frac{\int \sigma^{c\bar{c}}}{\int \sigma_{\gamma}}$
35-45	186	0.0029	15.0	0.543	0.470	0.184	$2.95 \cdot 10^{-3}$
45-55	234	0.0055	12.5	0.456	0.600	0.117	$3.90 \cdot 10^{-3}$
55-65	276	0.0089	10.0	0.375	0.724	0.077	$4.87 \cdot 10^{-3}$
65-75	309	0.0180	7.5	0.298	0.835	0.052	$5.73 \cdot 10^{-3}$
75-85	341	0.0353	5.0	0.229	0.923	0.033	$6.94 \cdot 10^{-3}$
35-85				1.9	$\bar{D}=0.66$	0.463	$\bar{R}=4.1 \cdot 10^{-3}$

Tab. 3.1: Numerical presentation of the cross sections for 100 GeV muon beam. $\sigma^{c\bar{c}}$ denotes the cross section for the open charm photo-production ($\gamma n \rightarrow c\bar{c} + X$), $\int \sigma_{\gamma}$ is the short expression of the formulae in the fifth column with $\sigma^{c\bar{c}}$ replaced by σ_{γ} , where σ_{γ} is the total DIS cross section of the photon.

The number of the open charm events from the range $35 \text{ GeV} < \nu < 85 \text{ GeV}$ is $N^{c\bar{c}} = 4.3 \cdot 10^{37} (\text{cm}^{-2} \text{ day}^{-1}) \cdot 1.9 (\text{nb}) = 82 \cdot 10^3 (\text{day}^{-1})$, while that of DIS events is $N^{\mu} = 4.3 \cdot 10^{37} (\text{cm}^{-2} \text{ day}^{-1}) \cdot 0.463 (\mu\text{b}) = 20 \cdot 10^6 (\text{day}^{-1})$.

Since it is not pragmatic to evaluate $N_{c\bar{c}}^{\rightarrow}$ and $N_{c\bar{c}}^{\leftarrow}$ in Eq. (3.2) by identifying all the fragmentation channels of $c\bar{c}$ from such a large target, what is studied is the selected clean channels, mainly

$$D^0 \rightarrow K^- + \pi^+ \quad \text{and} \quad \bar{D}^0 \rightarrow K^+ + \pi^- \quad . \quad (3.24)$$

The probability that a $c\bar{c}$ event produces D^0 or \bar{D}^0 is $N^{D^0}/N^{c\bar{c}} = 1.23$. Hereafter, the charge conjugate (\bar{D}^0) channel is implicitly considered. The branching ration that D^0 decays into K^- and π^+ is 4.0 %.

The traveling distance of D^0 is $c\tau = 123.7 \mu\text{m}$, which is not measurable in the setup of the COMPASS experiment. Instead, the strategy to evaluate the number of D^0 events is the reconstruction of the invariant D^0 mass from the decay particles (K^- and π^+).

Although the production of D^0 must be uniquely from open charm lepto-production, there are background events in the mass window $m_D \pm 20 \text{ MeV}$, assuming a practical mass resolution of $\sigma_M = 10 \text{ MeV}$). The background is called combinatorial background, i.e. a pair of K^- and π^+ from a DIS event accidentally matches to the D^0 invariant mass. The suppression of the background can be done by the kinematical cuts ' $z_{D^0} = E_{D^0}/\nu > 0.25$ AND $|\cos \theta^*| < 0.5$ ', where θ^* is the flight angle of the decay particle (K^-

or π^+) with respect to the flight line of D^0 . The first cut is based on the nature that large fraction of the photon energy is used for the production of $c\bar{c}$ in the open charm events. The second cut is based on the nature that the production angles of K^- and π^+ from D^0 are distributed rather uniformly while they from the combinatorial background concentrate in the forward direction. The first cut reduces the open charm detection by a factor 0.71 and the second does by another factor 0.5.

For the reconstruction of D^0 , both K^- and π^+ must travel inside the detector acceptance and K^- should not decay before the RICH detector which identifies the particle. Combining the kinematical cuts, $\pm 2\sigma$ mass window selection, the spectrometer acceptance and the constrain on the K decay, the overall acceptance for the D^0 reconstruction is $a_{D^0} = 0.29$. The open charm detection probability is

$$\varepsilon^{c\bar{c}} = \frac{N^{D^0}}{N^{c\bar{c}}} \cdot BR \cdot a_{D^0} = 0.0014 \quad . \quad (3.25)$$

The probability to accidentally find K^- and π^+ in the mass window after applying the criteria is

$$\varepsilon^{\text{BG}} = 2.27 \cdot 10^{-4} \quad , \quad (3.26)$$

normalized to the total DIS events.

In addition, the effect of the reinteraction of K^- and π^+ in the long target cell reduces the open charm detection probabilities by a factor $\varepsilon_{\text{target}}^S = 0.76$. Similarly, the detection probability of the background events decreases by $\varepsilon_{\text{target}}^S = 0.80$. The shadowing in the photoproduction cross section also reduces the background events by a factor $r_s = 0.95$.

Summarizing, the counting rate of the open charm event is

$$N^S = N^{c\bar{c}} \cdot \varepsilon^{c\bar{c}} \varepsilon_{\text{target}}^S = 887 \text{ (day}^{-1}\text{)} \quad (3.27)$$

and that of the combinatorial background is

$$N^S = N^{c\bar{c}} \cdot \varepsilon^{c\bar{c}} \varepsilon_{\text{target}}^S = 3450 \text{ (day}^{-1}\text{)} \quad . \quad (3.28)$$

3.2.3 Statistical accuracy

The statistical accuracy of the double spin asymmetry of $\gamma n \rightarrow c\bar{c}X$ is

$$\delta A^{\gamma n \rightarrow c\bar{c}X} = \frac{1}{P_T P_B f \bar{D}} \frac{1}{\sqrt{N^S}} \sqrt{1 + \frac{N^{\text{BG}}}{N^S}} \quad , \quad (3.29)$$

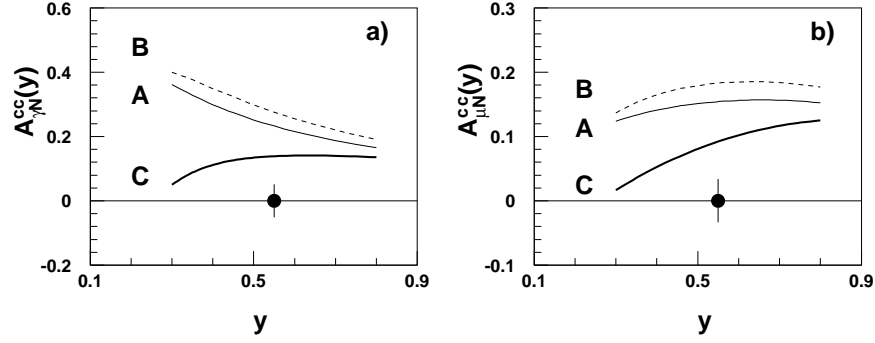


Fig. 3.3: (Left) Asymmetry $A^{\gamma n \rightarrow c\bar{c}X}$. (Right) asymmetry $A^{\mu n \rightarrow c\bar{c}X}$ for the open charm events as a function of y . The curves refer to the three sets of Δg from Ref. [71] as in Figure 3.1. The projected precision of the measurement in the range $0.35 < y < 0.85$ is indicated by the error bar at an arbitrary value $A = 0$.

where N^S is the count of the open charm events, and N^{BG} is that of the accidental background. Here, the relation

$$A^{\mu n \rightarrow c\bar{c}X} = \bar{D} A^{\gamma n \rightarrow c\bar{c}X} \quad (3.30)$$

and Eq. (3.2)-(3.3) are used.

Running the experiment for 2 years (150 days/year) with a moderate accelerator and spectrometer efficiency of 0.25, the count of the open charm events is $N^S \simeq 66$ k and that of the background is $N^{BG} = 260$ k. Assuming the experimental conditions $P_T = 0.45$, $P_B = 0.75$, $f = 0.5$, and $\bar{D} = 0.66$, The statistical accuracy of $A^{\gamma n \rightarrow c\bar{c}X}$ is

$$\delta(A^{\gamma n \rightarrow c\bar{c}X}) \simeq 0.08 \quad . \quad (3.31)$$

In the COMPASS experiment, improvement of the statistical accuracy is foreseen by tagging D^{*+} and its charge conjugate D^{*-} . The basic idea is shown here and the details can be found in Ref. [75]. About 33 % of the D^0 events comes from the decay chain

$$D^{*+} \rightarrow D^0 \pi_S^+ \rightarrow (K^- \pi^+) \pi_S^+ \quad , \quad (3.32)$$

where subscript S refers to the soft (small momentum) pion. The difference of the invariant mass $\Delta M = m(K^- \pi^+ \pi_S^+) - m(K^- \pi^+) = 145$ MeV is mostly carried by the mass of $\pi_S \approx 140$ MeV, therefore π_S has a small

momentum. It is expected that the measured ΔM distribution will show a sharp peak ($1\sigma \simeq 2.5 \text{ MeV}$) at $\Delta M = 145 \text{ MeV}$ on a small background ($N^{BG}/N^S \simeq 0.15$) because of the small kinematic phase space [77, 78] and the suppression of the combinatorial background by requiring 3 particles. Counting D^{*+} events in such a clean environment leads to a smaller statistical error. Combining D^{*+} tagged analysis with the non-tagged events, the statistical accuracy becomes

$$\delta(A^{\gamma n \rightarrow c\bar{c}X}) \simeq 0.05 \quad . \quad (3.33)$$

In Figure 3.3, this statistical accuracy is shown together with the predictions from the different polarized gluon distribution functions $g(\eta, \mu^2)$. With the data from COMPASS experiment, one can constrain $g(\eta, \mu^2)$ and can select the right models or descriptions.

The sensitivity to measure $\Delta g/g$ is

$$\delta\left(\frac{\Delta g}{g}\right) \simeq 0.14 \quad (3.34)$$

in the accessible η range and assuming $\int_a^b d\hat{s} \Delta\sigma(\hat{s}) / \int_a^b d\hat{s} \sigma(\hat{s}) \simeq 0.35$ in Eq. (3.20).

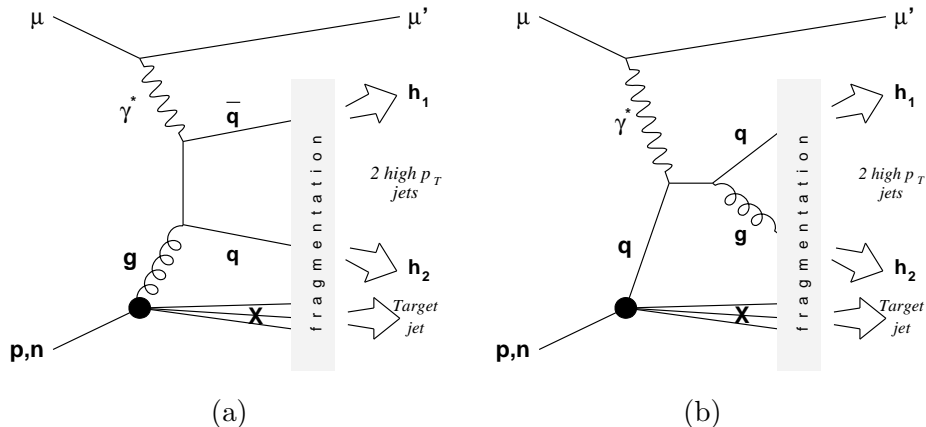


Fig. 3.4: (a) High p_T pair jets from Photo-gluon fusion process. (b) High p_T jet pair from QCD Compton process.

3.3 Comparison with the other experiments on Δg

In order to pin down the polarized gluon distribution function $\Delta g(\eta, \mu^2)$, variable approaches and several experiments are being prepared or taking data. The E161 experiment at SLAC is aiming at the $\Delta g/g$ measurement via open charm lepto-production using polarized real photon beam (35, 40 and 45 GeV) with the fixed polarized target [79]. In the COMPASS experiment, another approach to access $\Delta g/g$, namely *high p_T hadron pairs*, is proposed. In this section, the projected accuracy of the on-going and future experiments are presented after a brief introduction of those approaches.

3.3.1 High p_T hadron pairs

The polarized gluon distribution function Δg can be studied by tagging the high transverse momentum (high p_T) hadron pairs as first suggested by Bravar, Harah and Kotzinian [80]. The elementary process of interest is the photon-gluon fusion illustrated in Figure 3.4 (a). Unlike Section 3.1, the quark pair $q\bar{q}$ can be any flavor, practically all the light quark flavors (u , d and s), not only the charm flavor. This approach is based on the nature that the correlated hadron pairs from the open quark pair $q\bar{q}$ have high p_T compared to the hadrons from DIS events.

The double spin asymmetry of the correlated high p_T hadron pair $h_1 h_2$ is related to Δg as

$$A^{\ell n \rightarrow h_1 h_2}$$

$$= \frac{\sum_q \left[\Delta g \otimes D \otimes \Delta \hat{\sigma}^{\gamma^* g \rightarrow q\bar{q}} \otimes D_{q,\bar{q}}^{h_1+h_2} \right] + \sum_q \left[\Delta q \otimes D \otimes \Delta \hat{\sigma}^{\gamma^* q \rightarrow qg} \otimes D_{q,\bar{g}}^{h_1+h_2} \right]}{\sum_q \left[g \otimes \hat{\sigma}^{\gamma^* g \rightarrow q\bar{q}} \otimes D_{q,\bar{q}}^{h_1+h_2} \right] + \sum_q \left[q \otimes \hat{\sigma}^{\gamma^* q \rightarrow qg} \otimes D_{q,\bar{g}}^{h_1+h_2} \right]}, \quad (3.35)$$

where the process $\gamma^* q \rightarrow qg$ is called *QCD Compton process* which is illustrated in Figure 3.4 (b), $\hat{\sigma}$ ($\Delta\hat{\sigma}$) is the bare cross section (difference of the bare polarized cross section) of the parton process (γg or γq), D is the depolarization factor of virtual photon, $D_{a,b}^{h_1+h_2}$ is the fragmentation function from ab pair to the final state including $h_1 + h_2$, and \otimes refers to convoluted integration. The extraction of $\Delta g/g$ from this relation is complicated, because QCD Compton process $\gamma q \rightarrow q\bar{q}$ can not be separated from photon-gluon fusion $\gamma^* g \rightarrow q\bar{q}$ experimentally and the fragmentation functions $D_{a,b}^{h_1+h_2}$ are not analytical. These complications can be resolved by Monte Carlo simulations, introducing the theoretical errors due to the model- and description-dependence. Overall precision of 5%, together with statistical errors and systematic errors, to extract $\Delta g/g$ is projected at 4 bins in η in the COMPASS experiment [80].

In the same approach, the HERMES experiment at DESY is studying $\Delta g/g$ with limited statistics and the theoretical errors using 28 GeV positron beam [81]. In the future, TESLA-N project will pin down $\Delta g/g$ precisely using 250 and 500 GeV electron beam [82].

3.3.2 $p\bar{p}$ collision

The gluon polarization $\Delta g/g$ can also be accessed through prompt photon production in polarized proton-proton or proton-antiproton scattering. The processes of interest are $q\bar{q} \rightarrow \gamma g$ (quark-antiquark annihilation, inverse photon-gluon fusion) and $qg \rightarrow \gamma q$ as shown in Figure 3.5. In $p\bar{p}$ collision at $\sqrt{200}$ GeV, the quark-antiquark annihilation contributes only 10% since the antiquark density is smaller than the gluon density. The process (a) in Figure 3.5 produces a double spin asymmetry in the channel $p\bar{p} \rightarrow \gamma + jet + X$

$$A \simeq \frac{\Delta \hat{\sigma}(qg \rightarrow \gamma q)}{\hat{\sigma}(qg \rightarrow \gamma q)} \cdot \frac{\Delta g}{g} \cdot \frac{\sum_f e_f^2 \Delta q_f}{\sum_f e_f^2 q_f} \quad (3.36)$$

One of the subtle aspects which introduces the systematic errors in the extraction of the $\Delta g/g$ is the variation of $\Delta \hat{\sigma}(qg \rightarrow \gamma q)/\hat{\sigma}(qg \rightarrow \gamma q)$ in the measured kinematic range. The suppression of γ from π or η in the fragmenting jets is one of the technical challenges.

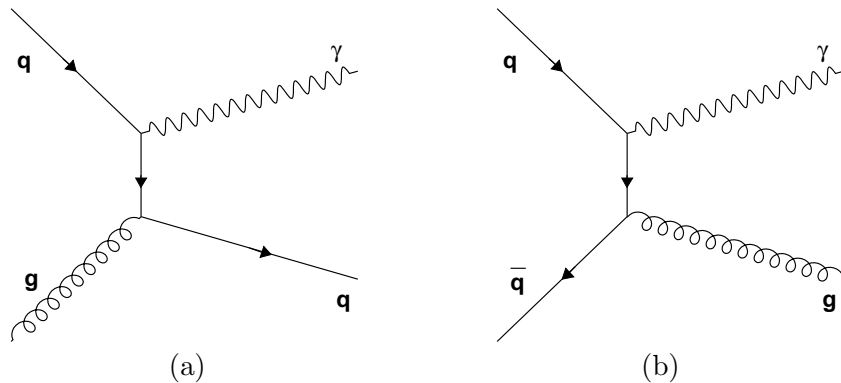


Fig. 3.5: Feynman diagram of the γ production in pp or $p\bar{p}$ collisions. (a) Prompt gamma production from a quark and a gluon. (b) Quark-antiquark annihilation (inverse photo-gluon fusion).

The STAR [83] and PHENIX [84] experiment at BNL-RHIC will determine $\Delta g/g$ in this approach using the pp collider with $\sqrt{s} = 200$ and 400 GeV.

3.3.3 Comparison of the expected precisions and the kinematic ranges

In Figure 3.6, shown are the expected precisions from various experiments on the measurement of $\Delta g/g$ vs gluon momentum fraction η , together with the HERMES data [81]. These experiments are complementary each other in the kinematic regions (η and μ^2) and offer cross checks via different measurement approaches.

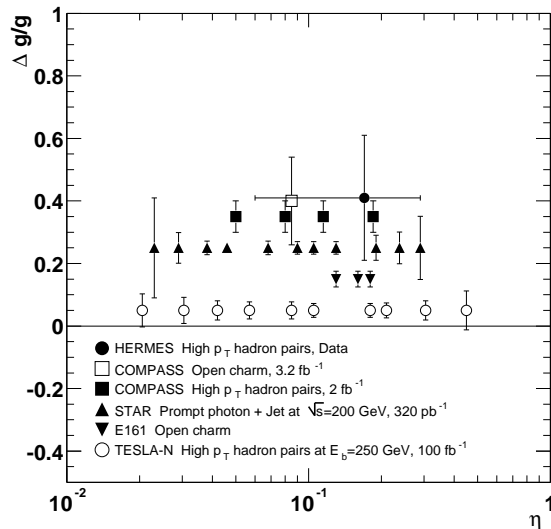


Fig. 3.6: Measured and projected accuracies on the measurement of $\Delta g/g$. Only HERMES data is measured [81] and its error bar includes only the statistical and systematic errors, not the theoretical errors due to model- and description-dependence. The projected precisions of COMPASS [75, 80], STAR [83, 82], E161 [79], and TESLA-N [82] are shown with the arbitrary values of $\Delta g/g$ for illustration.

3.4 Experimental setup

In this section, the experimental setup of the COMPASS experiment with the muon beam is described in the general terms.

The basic ideas in the COMPASS experiment are as follows.

- (a) Both the muon beam and the target nucleons must be polarized and the spin reversal of the target must be done in order to measure the double spin asymmetry in Eq. (3.2).
- (b) High intensity muon beam $2 \cdot 10^8$ muons/spill is used. The duration of the 1 spill was 5.1 (4.4) seconds in the SPS accelerator cycle of 16.8 (16.4) seconds in 2001 (2002). The scattered muons in the events of interest are only slightly separated from the non-scattered beam even after the spectrometer magnets. It is unavoidable to look at the scattered muons practically in the beam region.

- (c) The evaluation of the counting rate $N_{c\bar{c}}^{\rightarrow}$ and $(N_{c\bar{c}}^{\leftarrow})$ in Eq. (3.2) is based on the invariant mass reconstruction of the short-living hadrons (e.g. D^0) from their decay particles ($D^0 \rightarrow K^- + \pi^+$), it is essential to minimize the amount of materials in order to avoid the multiple scattering.
- (d) The kinematic of the muons, before and after the scattering, in triggered events must be determined.
- (e) The particle identification among π , K and proton, must be done by Ring Imaging CHerenkov (RICH) detector.
- (f) The outgoing particles of interest spread over wide opening angle (The largest opening angle of the polarized target apparatus is 169 mrad, from the downstream end of the target cell.)) and over wide momentum range from a few GeV to more than 100 GeV. These particles must be detected for better statistics and systematics.
- (g) The trigger for the measurement of $\Delta g/g$ is 'scattered muon + hadron detection'. The hadron calorimeter information is included into the trigger.

A lot of challenges has been done to fulfill these ideas and practically all the detectors had been newly developed or improved for the COMPASS experiment. The details of the spectrometer can be found in [75, 85].

The requirements above also impose the fast data acquisition and data analysis system. The data acquisition system of new generation has been developed [86], which can deal with an average data flow of 35 MBytes/s. The computing farm with object-oriented softwares has been built up [87]. The details can be found in the corresponding references.

3.4.1 Polarized muon beam

The COMPASS muon program uses the polarized muon (μ^+) beam from CERN M2 beam line [88]. The beam line can also transport secondary hadrons up to 300 GeV for the COMPASS hadron program by removing the absorbers and re-tuning the magnets. In this section, only the muon beam is mentioned.

The origin of the the polarized muon beam is the protons (max. $E = 450$ GeV) in CERN SPS (Super Proton Synchrotron) accelerator. The scheme of M2 beam line is shown in in Figure 3.7.

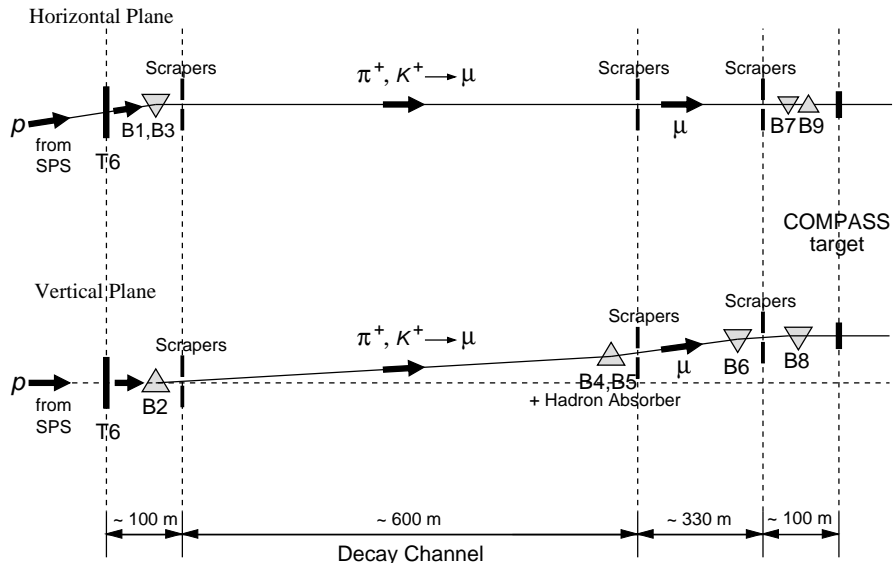


Fig. 3.7: Scheme of the M2 polarized muon beam line.

The protons in SPS are extracted to M2 beam line. The duration of the extraction, which corresponds to the duration of the spill in the experiment, was 5.1 (4.4) seconds in the so-called SPS accelerator cycle of 16.1 (16.8) seconds in 2001 (2002). The extracted protons are bombarded to T6 production target made of beryllium, producing charged pions and kaons. The intensity of the incident proton beam is about $1 \cdot 10^{13}$ protons/spill. The intensity of the final muon beam can be adjusted by changing the thickness of the production target. For the nominal intensity of $2 \cdot 10^8 \mu^+$ /spill, the thickness of beryllium target is tuned to be 500 mm.

A set of bending magnets and the scrapers (specially designed collimators) select the produced hadrons which have a momentum of $177 \text{ GeV}/c \pm 10\%$. The selected hadrons are transported to a 600 m long decay channel, in which about 5% of the hadrons decay into muons and neutrinos. After the decay channel, the remaining hadrons are absorbed in the hadron absorber which is 9.9 m long beryllium. The muons with a momentum of $160 \text{ GeV}/c \pm 3\% \text{ RMS}$ are selected by the bending magnets B4 and B5 and the scrapers in the next 330 m section.

The muon beam production above is done in the underground while the COMPASS experiment hall is located on the surface of the earth. The

muon energy	160 ± 5 GeV
beam intensity	$2 \cdot 10^8$ μ^+ /spill
beam polarization	-0.75 ± 0.04
beam size at the COMPASS target	$\sigma_x \sim \sigma_y \sim 8$ mm
beam divergence	$\sigma_{\theta_x} \sim 0.5$ mrad and $\sigma_{\theta_y} < 1$ mrad

Tab. 3.2: Nominal parameters of the polarized muon beam. The duration of the 1 spill was 5.1 (4.4) seconds in the SPS accelerator cycle of 16.8 (16.4) seconds in 2001 (2002).

muon beam is guided upward by the bending magnets B4 and B5, which are located about 15 m below the surface, and bent back by the bending magnet B6 so that it travels almost horizontally towards the COMPASS polarized target.

With the bending by B6, the momentum of each muon is measured by Beam Momentum Station (BMS), which consists of the 4 planes of the the scintillator hodoscope. The muon beam energy in the events of interest can be found by linking the timing of the scintillating fiber detectors in the COMPASS experiment hall to that of BMS hit timing. This method is used since BMS is located 100 upstream of the COMPASS target and the spatial correlation approach is not practical.

At about 20 m upstream of the COMPASS target, the beam spot size and the divergence of the muon beam is tuned by the bending magnets B7-B9 together with the multiple quadrupole magnets.

The polarization of the muon is naturally obtained, based on the parity violation in the weak decay of the charged pions or kaons. The polarization of the muon depends on the decay angle in the pion or kaon rest frame with respect to its traveling direction of motion in the Lab frame. Therefore, the sign and degree of the muon polarization can be chosen by selecting the corresponding muon energy. The polarization P_μ of the positive muon in the Lab frame can be calculated by [89]

$$P_\mu = -\frac{m_{\pi,K}^2 + (1 - 2\frac{E_{\pi,K}}{E_\mu})m_\mu^2}{m_{\pi,K}^2 - m_\mu^2} . \quad (3.37)$$

The real situation is complicated and Monte Carlo simulation is necessary to know the final beam intensity and the polarization, because the energies of pions and kaons are not monochromatic and the final muon polarization also depends on the ratio of the number of pion decay in the decay channel

to that of kaon. The measurements by the SMC experiment have established a good agreement with the results obtained by the Monte Carlo simulations of the beam transport [90, 91]. In the COMPASS experiment, the beam energy of 160 GeV and the beam polarization of -0.75 ± 0.04 were chosen as the best optimization of the beam intensity, the beam polarization and the spectrometer setup in 2001 and 2002.

The beam spot size at the COMPASS polarized target is of great importance because it decides the diameter of the target cells, which should be minimized in order to avoid the multiple scattering of the produced particles for efficient mass reconstruction of the short living hadrons. The beam size is about $\sigma_x \sim \sigma_y \sim 8$ mm, which is considerably reduced compared to that in the SMC experiment ($\sigma \sim 16$ mm) by adding the bending magnets B7-B9 and the quadrupole magnets near them. The nominal beam parameters are summarized in Table 3.2.

3.4.2 Polarized target

The small cross section of open charm lepto-production, and the limited beam intensity make it necessary to use a large solid state polarized target for the COMPASS muon program. On the other hand, the detection of short living hadrons demands the minimum non-target materials in the target apparatus for efficient invariant mass reconstruction. The details of the polarized target is described in Chapter 4. In this section, its characteristics in the spectrometer are presented.

The experimental goal for the extraction of $\Delta g/g$ is to measure the double spin asymmetry in Eq. (3.2) precisely. The sign of the target polarization must be flipped since the beam polarization is fixed. (Technically, it is in principle possible to extract the positively polarized muon beam by selecting the different muon energy according to Eq. (3.37). But such an approach would be useless since the kinematic region covered by the spectrometer setup would be completely changed and making the discussion of the asymmetry impossible.)

The double target cell configuration is employed as indicated in Figure 3.8 in order to reduce the systematic error due to the time-dependent variation in the beam intensity. The two target cells, namely upstream cell and downstream cell, have an identical dimension, a diameter of 30 mm and a length of 600 mm, and they are separated by 100 mm gap. The diameter is chosen to be consistent with beam size, covering $\sim \sigma \pm 2\sigma$ and the gap is chosen to be sufficient to identify by vertex reconstruction in which cell the events of interest took place.

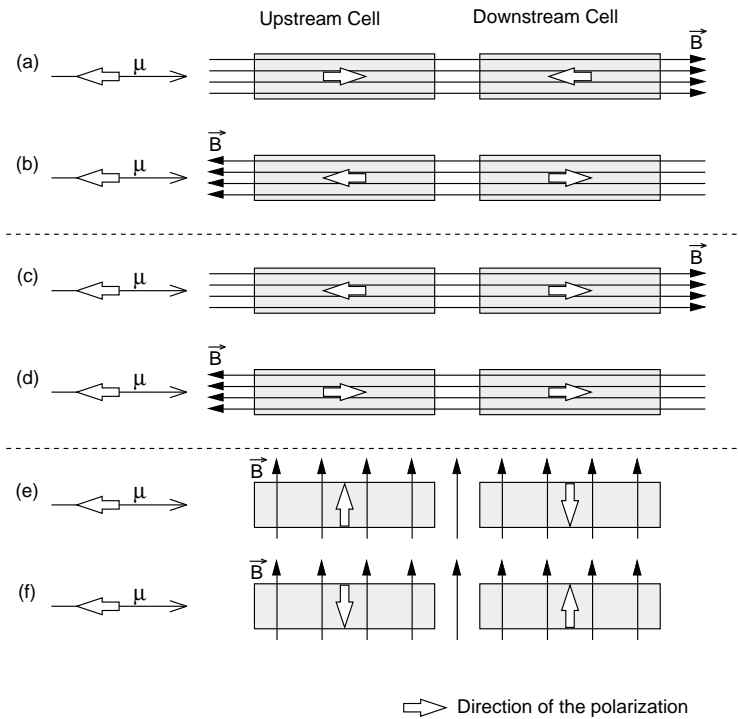


Fig. 3.8: 6 spin configurations in the COMPASS experiment. The negatively polarized muon beam traverses from the left side in the figure.

Lithium-6 deuteride (${}^6\text{LiD}$) is chosen as the target material for its high figure of merit. (It is foreseen to use ammonia NH_3 in the future to see a possible nuclei dependence of $\Delta g/g$, if any.) The material is beads shape with a typical dimension of a few millimeters for efficient cooling and they are filled into the target cells. The packing factor,

$$\frac{\text{volume occupied by the target material}}{\text{volume of the target cell}}, \quad (3.38)$$

was ~ 0.50 and ~ 0.45 in the upstream cell and in the downstream cell, respectively in 2001. From the run of 2002, larger packing factor is foreseen by changing the shape of the NMR coils which are embedded inside the target cells to measure the target polarization.

The two target cells are polarized longitudinally with respect to the traveling direction of the muon beam, as shown in either of Figure 3.8 (a)-(d). They are polarized in the opposite signs each other by dynamic nuclear

polarization (DNP) technique using microwaves. The typical deuteron polarization of ${}^6\text{LiD}$ was about 54 % when polarized in parallel to the external magnetic field (referred as positive polarization) and was about 48 % when polarized in anti-parallel (negative polarization).

One of the special features in the COMPASS polarized target is the spin reversal by so-called field rotation, which can be performed in about 30 min. The spin reversal by field rotation is based on the nature that the nuclear spin follows the direction of the external magnetic field which is rotating slowly compared to the Larmor frequency of the nuclear spin. By field rotation, the spin configuration can be changed from (a) to (b) (or from (c) to (d)) in Figure 3.8 and vice-versa. The field rotation is performed every 5-8 hours in order to reduce the systematic error due to the time-dependent variation in the spectrometer efficiency and that due to the different acceptance and the slightly different amount of the materials between the two cells.

The spin reversal by DNP technique needs about 1 week to reach the maximum polarization and is not adequate for the frequent spin reversal like several times per day. However, it is performed at least once in the annual beam time in order to change the spin configuration from (a) to (c) in Figure 3.8 (or from (c) to (d)) and vice-versa. The spin reversal by DNP helps in the suppression of the possible systematic error due to the magnetic field direction dependence of the spectrometer efficiency, if any.

The COMPASS muon program also contains the measurement of the transverse spin-dependent structure function with a transversely polarized target. Such a spin configuration can be realized by pausing the field rotation in the middle of it and holding the nuclear polarization in the so-called frozen spin mode with low temperature (80-100 mK) and with a transverse magnetic field (0.4-0.5 T). Spin configuration (e) in Figure 3.8 can be obtained from (a) or (b) in about 15 min. Similarly, (f) can be obtained from (c) or (d).

3.4.3 COMPASS spectrometer

The COMPASS spectrometer includes various kinds of detectors which requires the cutting edge technologies. The efforts to complete the proposed spectrometer in Ref. [75] are going on to achieve full COMPASS physics program.

In this section, the general design concept is presented, referring to the layout of the COMPASS spectrometer in 2001 which is shown in Figure 3.9. One of the characteristic features is the two-stage forward magnetic spec-

trometers based on the magnetic bending by the spectrometer magnet SM1 with a bending power of $1.0 \text{ T} \cdot \text{m}$ and SM2 with $4.4 \text{ T} \cdot \text{m}$. Both SM1 and SM2 bends the positive charge particles to the Jura side.

Incoming muon

The energy of the incoming muon is measured by BMS which is located at the end of the beam line (see Section 3.4.1) with a time resolution of 260 ps.

The scintillating fiber detectors FI01 and FI02, [92] each of which has the two planes (x - and y -sensitive) and covers the square of $40 \text{ mm} \times 40 \text{ mm}$. The pitch of the detection channel is 0.41 mm, giving the angular resolution of about 0.1 mrad. The time resolution of the FI01 and FI02 is about 500 ps. The muon energy in the events of interest can be determined by linking the FI01 and FI02 timing with the BMS timing.

Scattered muon

The scattered muon is separated from other produced particles with $\mu\text{Filter1}$ and $\mu\text{Filter2}$ which use the nature that muons can penetrate the thick materials most in the charged particles. $\mu\text{Filter1}$ is 1 m thick iron and is sandwiched by the detectors based on Plastic Iarocci Tubes (PIT) denoted as MA01 and MA02 in Figure 3.9. $\mu\text{Filter2}$ is the 2 m thick iron and is followed by the large drift tube MB01. ($\mu\text{Filter2}'$ and $\mu\text{Filter3}$ are the concrete blocks which protects the trigger hodoscopes HM05, HL05 and HI05 from the hadrons which have traveled through the central holes of $\mu\text{Filter2}$.)

The scattered muon is tracked back from MB01, located about 35 m downstream of the target, to the target region based on the hits in the numerous planes of detectors and based on the 'bridging' through SM1 and SM2. The scattered muons which are interesting for the measurement of $\Delta g/g$ are only slightly separated from the beam region because such events are related to small Q^2 and the scattered muons carry a large fraction of the initial energy. Such scattered muons are mainly detected by the scintillating fibers FI03-08 that are installed inside or near the beam region.

The vertex reconstruction is done by linking the incoming muon with the scattered muon and any produced particle. In the vertex reconstruction, the information from the detectors between the target and SM1 play an important role. In this zone, FI03 and FI04 (scintillating fiber detectors) cover the beam region and Micromega1-3 (Micro Mesh Gas Structure detector, high spatial resolution gas-wire chambers) cover outside the beam region, The spatial resolution of the vertex reconstruction along the beam

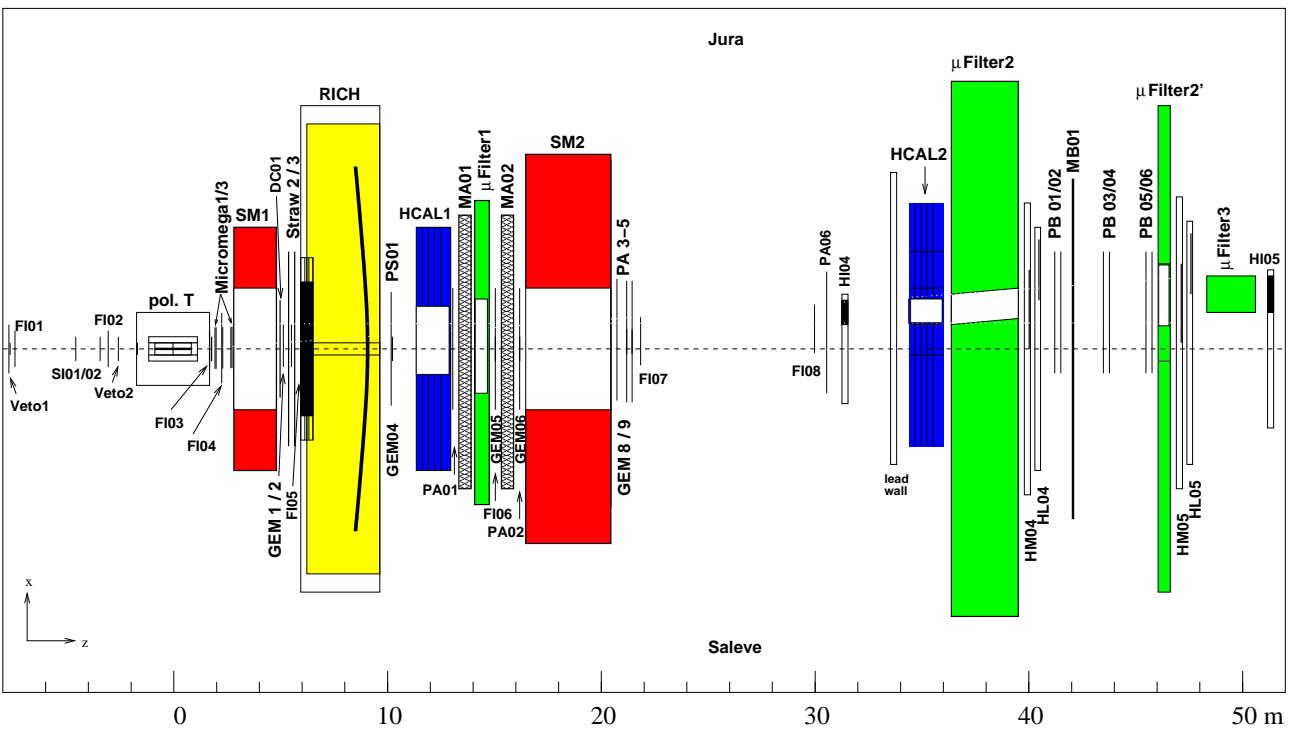


Fig. 3.9: Top view of the COMPASS spectrometer during the 2001 and 2002 data taking. The polarized muon beam enters from the left in this Figure (from the bottom in this page). Jura and Saleve are the name of mountains which are used to define the horizontal direction (x).

direction z , which is important to identify in which cell the events of interest took place, is a few centimeters and varies depending on the angle of the scattered muon.

Produced particles and hadron identification

The momentum of the produced particle with a large (small) outgoing angle and/or with a low (high) momentum are analyzed by the detectors located near SM1 (SM2). The trajectory of the particles is determined by the numerous detectors, FI03-08, Micromega1-3, GEM1-9 (Gas Electron Multiplier, gas-wire detectors), DC01 (Drift Chamber), MWPC's (Multi Wire Proportional Chambers) denoted as PS01, PA01-06, PB01-06 in the figure, and Straw2-3 (straw tube detectors), which are covering the beam region to the large angle,

The hadrons are identified by asking the following criteria 'stopped in μ Filter1 (μ Filter2) + a certain energy deposit in HCAL1 (HCAL2)'. Here HCAL stands for Hadron CALorimeter and HCAL1 (HCAL2) consists of the multiple sandwiches of 20 (25) mm thick iron and 5 (3) mm thick scintillator. The signals from hadron calorimeters are included in the trigger for the measurement of $\Delta g/g$. In the offline, RICH (Ring Imaging CHerenkov detector) identifies the particles, mainly among pions, kaons, and protons.

Triggers

There are several triggers in the COMPASS muon program. Here the triggers for the measurement of $\Delta g/g$ is presented.

The event which is interesting for the measurement of $\delta g/g$ is called *Quasi-real photon events*, because the large fraction of the events comes from small η region and the scattered muons naturally have small Q^2 (quasi-real-photon), practically $Q^2 < 0.5 \text{ GeV}^2$. For efficient measurement, it is desired to select the high photon polarization (small depolarization effect) region, i.e. $y > 0.3$. The trigger so-called it Inner Trigger (IT) is formed by detecting the slightly scattered muon which is bended by SM1 and SM2 slightly more than the beam muons, practically by the dedicated scintillator hodoscopes HI04 and HI05. Similarly, *Ladder Trigger* (LT) is formed by HL04 and HL06. Usage of two planes (one in upstream of SM2 and the other in downstream of it) for each trigger suppress the contamination from the muons which is not interesting but is deflected in the target only by multiple scattering. IT is designed to cover the kinematic region $y < 0.5$ AND $Q^2 < 0.5 \text{ GeV}^2$, while LT is to cover the region ' $y > 0.5$ AND $Q^2 < 0.5 \text{ GeV}^2$ '.

The main background events in IT and LT are hard photon radiation events, Möller scattering with a electron in the target substance, ($\mu^+ + e^- \rightarrow \mu^{+'} + e^-$), and slightly low energy halo muon which is bended like a scattered muon. In order to suppress such events, a minimum energy deposit in one of the hadron calorimeters (HCAL1 or HCAL2) is ANDed to IT and LT. The improved triggers are abbreviated as ITC and MTC, respectively.

There still is a contamination in the ITC and MTC, which is due to the halo muon that is located around the nominal beam region and/or has the large incoming angle, eventually hitting hit the trigger hodoscopes. Such halo muons are suppressed by NANDing the hits in the veto counters denoted as Veto1-2 and also by NANDing that in the veto counter installed at the end of the beam line. In addition, a incoming muon with large angle is suppressed by using the angle information obtained from the selected channels of FI01 and FI02. Resulting veto trigger is denoted as \bar{V} , where $\bar{}$ refers to NAND.

ITC \bar{V} and LTC \bar{V} are the trigger which is mainly used for the investigation of $\Delta g/g$ via photo-gluon fusion process in the COMPASS experiment.

4. POLARIZED TARGET

The polarized target is an essential and crucial apparatus in the COMPASS experiment as can be seen in Chapter 3. The COMPASS muon program can not be started without a large and high performance polarized target. In addition, the determination of the polarization of the target must be done precisely because it affects the evaluation of the gluon polarization $\Delta g/g$.

The author contributed to the preparation, the installation, and the commissioning of the COMPASS polarized target, which successfully started its operation in 2001. This chapter is devoted to the description of the COMPASS polarized system.

Section 4.1 is the theoretical description of the dynamic nuclear polarization (DNP), based on which a high nuclear polarization can be obtained.

Section 4.2 explains how to determine the target polarization, including the electronics to detect the nuclear magnetic resonance (NMR) signal which contains the information of the polarization.

In Section 3.4, the apparatus of the COMPASS polarized target is described by dividing it into four sub-systems, the dilution refrigerator, the superconducting magnet, the microwave system, and the nuclear magnetic resonance system. One of the challenges in the COMPASS experiment was to minimize the non-target materials and it is reported in the context of the microwave cavity design.

In Section 4.4, the target material ${}^6\text{LiD}$ is described. ${}^6\text{LiD}$ is chosen for its high figure of merit, specifically its large fraction of the polarizable nucleons and its high polarization. Owing to this high figure of merit, one can save the beam time.

In Section 4.5, reported is the the results from the polarized target, including the high deuteron polarization and the procedure for the precise measurements. The equal spin temperature theory was tested and confirmed. Its validity provides a significant benefit to the experiments.

4.1 Dynamic nuclear polarization

High target polarization is realized via dynamic nuclear polarization (DNP) process in which microwaves are used to artificially enhance the polarization above the *thermal equilibrium* value. For this purpose, the material must have *unpaired electrons*, referred also as *paramagnetic centers*. Due to their large magnetic moments, unpaired electrons have a polarization of 96 % at a magnetic field of 2.5 T and at temperature of 1 K while those of nuclei are below 1 %. The heart of DNP is to transfer the high electron polarization to nuclear spins.

This section is devoted to the description of the DNP mechanism through quantum mechanical approach. First of all, the definition of the polarization is clarified in Section 4.1.1. The key ideas related to the DNP mechanism are

- (1) Thermal equilibrium polarization (Section 4.1.2),
- (2) Zeeman splitting (Section 4.1.3),
- (3) Simultaneous spin flips of an electron and a nucleus via dipolar-dipolar interaction (Section 4.1.4),
- (4) Relaxation of spins (Section 4.1.4),
- (5) Spin diffusion and differential solid effect (Section 4.1.5).

In addition to dipolar-dipolar interaction effect in (3) above, DNP via hyperfine interaction effect in our ${}^6\text{LiD}$ material is discussed in Section 4.1.6. The concept *equal spin temperature* is introduced in Section 4.1.7.

In this thesis, only the basics and the results of the theories on DNP are discussed with the orientation of its application to COMPASS polarized target case. More general and detailed description covering the aspects behind the DNP can be found, for example, in Ref. [93, 94, 95, 96].

4.1.1 Definition of polarization

Throughout this thesis, the term *polarization* refers *vector polarization* which is defined for spin system I by the formula

$$P = \frac{\langle m \rangle}{I} = \frac{\sum_{m=-I}^I m n(m)}{I \sum_{m=-I}^I n(m)} \quad , \quad (4.1)$$

where $m = -I, -I + 1, \dots, I$ is the magnetic quantum number and $n(m)$ is the population of the spin state m . $\langle m \rangle$ is macroscopically the average value of m in the spin ensemble.

For an intuitive understanding, it is useful to write down the Eq. (4.1) for the cases spin- $\frac{1}{2}$, -1 and $-\frac{3}{2}$, that are considered in this thesis.

$$\text{spin} - \frac{1}{2} \quad P = \frac{n_+ - n_-}{n_+ + n_-} \quad (4.2)$$

$$\text{spin} - 1 \quad P = \frac{n_+ - n_-}{n_+ + n_0 + n_-} \quad (4.3)$$

$$\text{spin} - \frac{3}{2} \quad P = \frac{3n(+\frac{3}{2}) + n(+\frac{1}{2}) - n(-\frac{1}{2}) - 3n(-\frac{3}{2})}{3 \left[n(+\frac{3}{2}) + n(+\frac{1}{2}) + n(-\frac{1}{2}) + n(-\frac{3}{2}) \right]} \quad (4.4)$$

Here, the spin state populations $n(m)$ are expressed in a short-hand form for spin- $\frac{1}{2}$ and spin-1 since they can be identified uniquely.

4.1.2 Thermal equilibrium polarization

The *thermal equilibrium* (TE) state is the beginning of the solid state polarized target in many aspects, while one can easily see that TE polarization is not large enough for the particle physics experiments.

The term *thermal equilibrium* means the state that the spin system is in the equilibrium with the rest of the world and is governed by the lattice temperature. In such a state, the population distribution of the spin system follows the Boltzmann statistics. When non-interacting spins with magnetic moment $\vec{\mu}$ are placed in a magnetic field \vec{B}_0 pointing along the z -axis, there will be a Zeeman splitting where the energy level of the spin- I is splitted into $2I + 1$ sublevels separated by quanta of $\hbar\omega_0 = \mu B_0/I$ in energy. $\omega_0/2\pi$ is called the Larmor frequency, at which the spin precesses about the magnetic field direction. The energy of the sublevels is expressed by $E_m = -\hbar\omega_0 m$, where $m = -I, -I + 1, \dots, I - 1, I$ is the magnetic quantum number. Following the Boltzmann statistics analysis, the spin polarization in a substance of temperature T is given by the Brillouin function [97]

$$P = B_I(\alpha) = \frac{1}{I} \left[\left(I + \frac{1}{2} \right) \coth \left(\left(I + \frac{1}{2} \right) \alpha \right) - \frac{1}{2} \coth \left(\frac{\alpha}{2} \right) \right], \quad (4.5)$$

where $\alpha = \hbar\omega_0/k_B T = \mu B_0/Ik_B T$ with Boltzmann constant k_B . For the cases of spin- $\frac{1}{2}$ and spin-1, Equation (4.5) is simplified to

$$\text{spin} - \frac{1}{2} \quad P = \tanh \left(\frac{\hbar\omega_0}{2k_B T} \right) \quad (4.6)$$

$$\text{spin} - 1 \quad P = \frac{4 \tanh\left(\frac{\hbar\omega_0}{2k_B T}\right)}{3 + \tanh\left(\frac{\hbar\omega_0}{2k_B T}\right)} . \quad (4.7)$$

By these formula, one can calculate the TE polarization of nuclei. In a practical experimental condition, at a magnetic field $B_0 = 2.5$ T and at temperature $T = 1.0$ K, the polarizations of proton (spin- $\frac{1}{2}$), deuteron (spin-1), ^6Li (spin-1), ^7Li (spin- $\frac{3}{2}$) are 0.25 %, 0.052 %, 0.050 %, and 0.17 %, respectively. Apparently, the polarization needs to be largely enhanced for particle physics experiments. In contrast to the nuclei, electrons have high polarization, 96 % in the same condition, due to its large magnetic moment. The DNP mechanism makes use of the high electron polarization.

In the experiment, TE polarization plays an important role in the calibration of polarization measurement by nuclear magnetic resonance, which is described in Section 4.2.3.

4.1.3 Zeeman splitting

Consider an electron with a magnetic moment $\vec{\mu}_e$ and a nucleus with a magnetic moment $\vec{\mu}_I$. In the discussion, the nuclear spin $I = 1$ is considered because the target material ^6LiD contains principally spin-1 nuclei, i.e. D and ^6Li . When the electron and the nucleus do not interact each other, the Hamiltonian for such a pair is

$$\mathcal{H} = -\vec{\mu}_e \cdot \vec{B}_0 - \vec{\mu}_I \cdot \vec{B}_0 = \hbar\omega_e M - \hbar\omega_I m \quad , \quad (4.8)$$

where M and m are the magnetic quantum number of the electron and the nuclear spin respectively, and

$$\hbar\omega_e = |2\mu_e B_0|, \quad \hbar\omega_I = \frac{\mu_I B_0}{I} . \quad (4.9)$$

Zeeman splitting produces 6 eigen-states of this system, denoted by $|Mm\rangle$, which have the following eigen-energies

$$\begin{aligned} \langle + - | \mathcal{H} | + - \rangle &= E_{+-} = +\frac{1}{2}\hbar\omega_e + \hbar\omega_I \\ \langle + 0 | \mathcal{H} | + 0 \rangle &= E_{+0} = +\frac{1}{2}\hbar\omega_e \\ \langle + + | \mathcal{H} | + + \rangle &= E_{++} = +\frac{1}{2}\hbar\omega_e - \hbar\omega_I \\ \langle - - | \mathcal{H} | - - \rangle &= E_{--} = -\frac{1}{2}\hbar\omega_e + \hbar\omega_I \end{aligned} \quad (4.10)$$

$$\begin{aligned} \langle -0 | \mathcal{H} | -0 \rangle &= E_{-0} = -\frac{1}{2} \hbar \omega_e \\ \langle -+ | \mathcal{H} | -+ \rangle &= E_{-+} = -\frac{1}{2} \hbar \omega_e - \hbar \omega_I \quad . \end{aligned}$$

The nuclear (electron) spin can be flipped by irradiating the system with an rf field. The Hamiltonian for such an rf field is expressed as

$$\mathcal{H}_{rf} = (\hbar \omega / 2) [I_+ e^{-i\omega t} + I_- e^{i\omega t}] \quad (4.11)$$

with $\omega = \omega_I$ (ω_e). The rate of spin flip, i.e. transition probability from state k to state i is given as

$$Pr.(k \rightarrow i) = \frac{2\pi}{\hbar} \left| \langle \mathcal{H}_{rf} | \right|^2 \delta(|E_k - E_i| - \hbar \omega) \quad (4.12)$$

by Fermi's Golden Rule [98]. No net polarization of an ensemble of nucleus (or electron) spin is achieved because the spin flipping rate is equal in either direction, for example $Pr.(+0 \rightarrow ++)$ = $Pr.(++ \rightarrow +0)$. In addition, there is no chance to flip both spins simultaneously because probabilities like $|\langle ++ | \mathcal{H}_{rf} | 00 \rangle|^2$ are zero. Such transitions are called the forbidden transitions but they will be found possible via interaction between the nuclear spin and the electron spin.

4.1.4 Dipolar-dipolar interaction

The dipolar-dipolar interaction between a electron and a nucleus produces the mixing of the pure eigen-states in Eq. (4.10), which allows the simultaneous spin flipping. Its quantum mechanical descriptions are considered in this section.

The magnetic dipole field of a nucleus positioned at the origin is [99]

$$\vec{B}_I = -\frac{\mu_0}{4\pi} \frac{\vec{\mu}_I - 3\hat{r} \cdot \vec{\mu}_I}{r^3} = -\frac{\mu_0}{4\pi} g_I \mu_N \frac{\vec{I} - 3\hat{r} \cdot \vec{I}}{r^3} \quad . \quad (4.13)$$

The electron magnetic moment $\vec{\mu}_e$ interacts with this additional field and one more term must be considered in Hamiltonian in addition to Eq. (4.8),

$$\mathcal{H}_{DDI} = -\vec{\mu}_e \cdot \vec{B}_I = -\frac{\mu_0}{4\pi} \frac{g_e \mu_B g_I \mu_N}{r^3} \left[(\vec{S} \cdot \vec{I}) - 3(\hat{r} \cdot \vec{S})(\hat{r} \cdot \vec{I}) \right] \quad . \quad (4.14)$$

Since the electron Zeeman energy is much larger than dipolar-dipolar interaction in the usual magnetic field, the Hamiltonian \mathcal{H}_{DDI} can be treated as a perturbation. Now the vector \vec{r} is pointing from the nuclear spin to the

electron spin. Taking z -axis along the external magnetic field \vec{B}_0 , employing a polar-coordination expression for \vec{r}

$$\begin{aligned}\hat{r}_+ &= \hat{r}_x + i\hat{r}_y = e^{i\phi} \sin(\theta) \\ \hat{r}_- &= \hat{r}_x - i\hat{r}_y = e^{-i\phi} \sin(\theta) \\ \hat{r}_z &= \cos(\theta) \quad ,\end{aligned}\tag{4.15}$$

and using the usual expressions of the spin operators for the electron spin S and the nuclear spin I

$$S_+ = S_x + iS_y, \quad S_- = S_x - iS_y, \quad S_z = S_z \quad ,\tag{4.16}$$

$$I_+ = I_x + iI_y, \quad I_- = I_x - iI_y, \quad I_z = I_z \quad ,\tag{4.17}$$

the evaluation of the Hamiltonian \mathcal{H}_{DDI} in Eq. (4.14) reads

$$\begin{aligned}\mathcal{H}_{\text{DDI}} &= -\frac{\mu_0}{4\pi} g_e \mu_B g_I \mu_N \times \\ &\left[\left(1 - 3 \cos^2(\theta)\right) S_z I_z \right. \\ &\quad - \frac{3}{2} \sin(\theta) \cos(\theta) e^{-i\phi} S_z I_+ - \frac{3}{2} \sin(\theta) \cos(\theta) e^{i\phi} S_z I_- \\ &\quad - \frac{3}{2} \sin(\theta) \cos(\theta) e^{-i\phi} S_+ I_z - \frac{3}{2} \sin(\theta) \cos(\theta) e^{i\phi} S_- I_z \\ &\quad - \frac{3}{4} \sin^2(\theta) e^{-2i\phi} S_+ I_+ - \frac{3}{4} \sin^2(\theta) e^{2i\phi} S_- I_- \\ &\quad \left. + \left(\frac{1}{2} - \frac{3}{4} \sin^2(\theta)\right) S_+ I_- + \left(\frac{1}{2} - \frac{3}{4} \sin^2(\theta)\right) S_- I_+ \right] .\end{aligned}\tag{4.18}$$

The new eigen-states and the new eigen-energies of the system can be found by a perturbative expansion of the Zeeman system. For simplicity, let $|n^0\rangle$ ($n = 1, 2, \dots, 6$) denote the the Zeeman states $|Mm\rangle$, making $|1^0\rangle$ refer the highest energy state, $|2^0\rangle$ the second highest, ..., and $|6^0\rangle$ the lowest energy state (see Eq. (4.10)) The new state kets are calculated in the first order perturbation theory with [98]

$$|n\rangle = |n^0\rangle + \sum_{k \neq n} \frac{|k^0\rangle \langle k^0 | \mathcal{H}_{\text{DDI}} | n^0 \rangle}{E_n^0 - E_k^0} \quad ,\tag{4.19}$$

and the new eigen-energies are calculated with

$$E_n = E_{n^0} + \langle n | \mathcal{H}_{\text{DDI}} | n \rangle = E_{n^0} + \langle n^0 | \mathcal{H}_{\text{DDI}} | n^0 \rangle + \sum_{k^0 \neq n^0} \frac{|\langle k^0 | \mathcal{H}_{\text{DDI}} | n^0 \rangle|^2}{E_{n^0} - E_{k^0}} \quad ,\tag{4.20}$$

where E_n^0 refers to the unperturbed energy in Eq. (4.10). As an example, the new perturbed state $|2\rangle$ of the Zeeman state $|2^0\rangle$ is

$$\begin{aligned}
|2\rangle = & | + 0 \rangle \\
& + \frac{\mu_0 g_e \mu_B}{4\pi B_0 r^3} \left[\frac{3\sqrt{2}}{4} \sin(\theta) \cos(\theta) e^{i\phi} | + - \rangle - \frac{3\sqrt{2}}{4} \sin(\theta) \cos(\theta) e^{-i\phi} | + + \rangle \right. \\
& \quad + \frac{3\sqrt{2}}{4} \frac{\hbar\omega_I}{\hbar\omega_e - \hbar\omega_I} \sin^2(\theta) e^{2i\phi} | - - \rangle \\
& \quad \left. - \sqrt{2} \left(\frac{1}{2} - \frac{3}{4} \sin^2(\theta) \right) \frac{\omega_I}{\hbar\omega_e + \hbar\omega_I} | - + \rangle \right] . \quad (4.21)
\end{aligned}$$

The last two terms (perturbation with $\Delta M = 1$) is smaller than the other two perturbation terms ($\Delta M = 0$) by a factor $\mathcal{O}(\omega_I/\omega_e) \sim 10^{-3}$, such terms can be ignored and Eq. (4.18) can be simplified to

$$\begin{aligned}
\mathcal{H}_{\text{DDI}} = & -\frac{2\sqrt{2}}{3} \eta \hbar\omega_I \left[(1 - 3 \cos^2(\theta)) S_z I_z - \frac{3}{2} \sin(\theta) \cos(\theta) e^{-i\phi} S_z I_+ \right. \\
& \quad \left. - \frac{3}{2} \sin(\theta) \cos(\theta) e^{i\phi} S_z I_- \right] , \quad (4.22)
\end{aligned}$$

where $\eta = \frac{\mu_0 3\sqrt{2} g_e \mu_B}{4\pi 4B_0 r^3}$. Renormalizing the new state kets so that $\langle n|n\rangle = 1$, they are

$$\begin{aligned}
|1\rangle & = (| + - \rangle - \epsilon^* | + 0 \rangle) / \sqrt{1 + |\epsilon|^2} \\
|2\rangle & = (| + 0 \rangle + \epsilon | + - \rangle - \epsilon^* | + + \rangle) / \sqrt{1 + 2|\epsilon|^2} \\
|3\rangle & = (| + + \rangle + \epsilon | + 0 \rangle) / \sqrt{1 + |\epsilon|^2} \\
|4\rangle & = (| - - \rangle + \epsilon^* | - 0 \rangle) / \sqrt{1 + |\epsilon|^2} \\
|5\rangle & = (| - 0 \rangle - \epsilon | - - \rangle + \epsilon^* | - + \rangle) / \sqrt{1 + 2|\epsilon|^2} \\
|6\rangle & = (| - + \rangle - \epsilon | - 0 \rangle) / \sqrt{1 + |\epsilon|^2} , \quad (4.23)
\end{aligned}$$

where $\epsilon = \eta \sin(\theta) \cos(\theta) e^{i\phi}$. The new eigen-energies corresponding to $|1\rangle$, $|2\rangle$, ..., $|6\rangle$ are

$$\begin{aligned}
E_1 & = \frac{1}{2} \hbar\omega_e + \left[1 + \frac{2}{3} \eta (3 \cos^2(\theta) - 1) \right] \hbar\omega_I \\
E_2 & = \frac{1}{2} \hbar\omega_e
\end{aligned}$$

$$\begin{aligned}
E_3 &= \frac{1}{2}\hbar\omega_e - \left[1 + \frac{2}{3}\eta(3\cos^2(\theta) - 1)\right]\hbar\omega_I \\
E_4 &= -\frac{1}{2}\hbar\omega_e + \left[1 - \frac{2}{3}\eta(3\cos^2(\theta) - 1)\right]\hbar\omega_I \\
E_5 &= -\frac{1}{2}\hbar\omega_e \\
E_6 &= -\frac{1}{2}\hbar\omega_e - \left[1 - \frac{2}{3}\eta(3\cos^2(\theta) - 1)\right]\hbar\omega_I \quad .
\end{aligned} \tag{4.24}$$

One can see that η is a dimension less coefficient which represents the strength of the perturbation relative to the Zeeman state. The numerical value of η of the target material ${}^6\text{LiD}$ at an external magnetic field $B_0 = 2.5 \text{ T}$ is $9.8 \cdot 10^{-2}$ for $r = 2.0 \cdot 10^{-10} \text{ m}$, which is the distance from the unpaired electron to the neighbor ${}^6\text{Li}$ nuclei, and is $1.2 \cdot 10^{-2}$ for $r = 4.0 \cdot 10^{-10} \text{ m}$, which is that to the nearest deuterons.

Now look at the possibilities of simultaneous spin flips of the electron and the nucleus by an rf field. The transition probabilities and the rf frequencies which induce such forbidden transitions can be calculated by Eq. (4.12)

$$\begin{aligned}
Pr.(6 \rightarrow 2) &= W_2 \quad \text{at} \quad \omega_{rf} = \omega_e + \left[1 - \frac{2}{3}\eta(3\cos^2(\theta) - 1)\right]\omega_I \\
Pr.(5 \rightarrow 1) &= W_2 \quad \text{at} \quad \omega_{rf} = \omega_e + \left[1 + \frac{2}{3}\eta(3\cos^2(\theta) - 1)\right]\omega_I \\
Pr.(4 \rightarrow 2) &= W_2 \quad \text{at} \quad \omega_{rf} = \omega_e - \left[1 - \frac{2}{3}\eta(3\cos^2(\theta) - 1)\right]\omega_I \\
Pr.(5 \rightarrow 3) &= W_2 \quad \text{at} \quad \omega_{rf} = \omega_e - \left[1 + \frac{2}{3}\eta(3\cos^2(\theta) - 1)\right]\omega_I \quad ,
\end{aligned} \tag{4.25}$$

with

$$W_2 \simeq 4|\epsilon|^2 \frac{2\pi}{\hbar} \frac{(\hbar\omega_{rf})^2}{4} \quad . \tag{4.26}$$

On the other hand, the allowed transitions (only the electron spin flips) occurs as follows,

$$\begin{aligned}
Pr.(4 \rightarrow 1) &= W_1 \quad \text{at} \quad \omega_{rf} = \omega_e + 2\frac{2}{3}\eta(3\cos^2(\theta) - 1)\omega_I \\
Pr.(5 \rightarrow 2) &= W_1 \quad \text{at} \quad \omega_{rf} = \omega_e \\
Pr.(6 \rightarrow 3) &= W_1 \quad \text{at} \quad \omega_{rf} = \omega_e - 2\frac{2}{3}\eta(3\cos^2(\theta) - 1)\omega_I \quad ,
\end{aligned} \tag{4.27}$$

with

$$W_1 \simeq \frac{2\pi}{\hbar} \frac{(\hbar\omega_{rf})^2}{4} \quad . \tag{4.28}$$

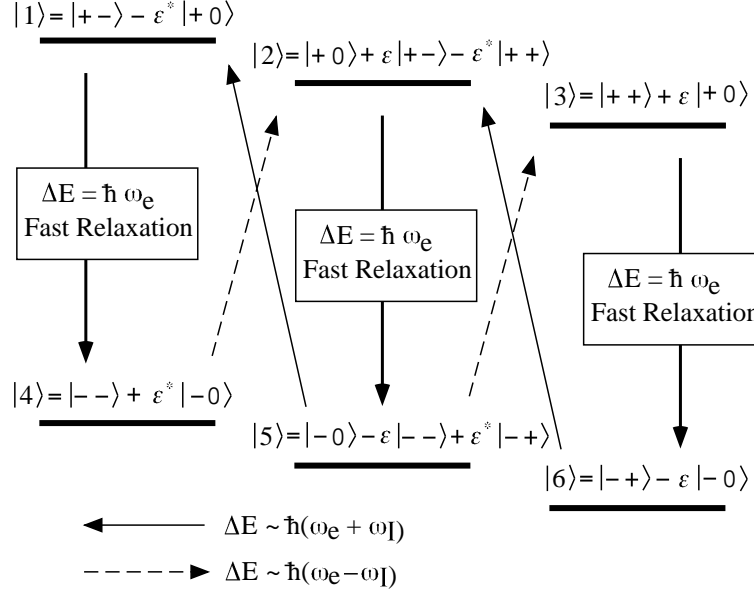


Fig. 4.1: Illustration of the spin states and the DNP mechanism via dipolar-dipolar interaction in a pair of a electron spin and a nuclear spin. For simplicity, the spin states are indicated without renormalization. The spin states with renormalization can be found in Eq. (4.23).

The simultaneous spin flipping is less probable than the allowed transitions by a factor $4|\varepsilon|$, but is still possible. (For an numerical information, $4|\varepsilon|^2 = 9.6 \cdot 10^{-3}$ for a pair which is separated by $r = 2.0 \cdot 10^{10}$ m and $4|\varepsilon|^2 = 1.4 \cdot 10^{-4}$ for that separated by $r = 4.0 \cdot 10^{10}$ m.)

Figure 4.1 is the illustration of the DNP mechanism. In an experimental condition, for example at external magnetic field of 2.5 T and at a temperature of 0.5 K, the electrons are polarized more than 99% while the nuclear polarizations are less than 1% (see Section 4.1.2). Thus the population at the state $|1\rangle$, $|2\rangle$ and $|3\rangle$ are virtually zero and those at $|4\rangle$, $|5\rangle$ and $|6\rangle$ are approximately equal, i.e. each of state $|4\rangle$, $|5\rangle$ and $|6\rangle$ has 1/3 of the total population. By irradiating the spin system with an rf field of $\hbar\omega_{rf} \sim \hbar\omega_e - \hbar\omega_I$, one can induce the the forbidden transitions $|4\rangle \rightarrow |2\rangle$ and $|5\rangle \rightarrow |3\rangle$. (Strictly speaking, the rf frequency must fulfill the conditions in Eq. (4.25). But practically in the ensemble of such spins, the energy levels are not sharp as indicated in Figure 4.1 any more because the angle θ takes a random value (the material beads are filled without preferred orien-

tations) and the dipolar-dipolar interaction between the unpaired electrons broadens the energy levels. Thus the rf field of $\hbar\omega_{rf} \sim \hbar\omega_e - \hbar\omega_I$ can induce those transitions as a net.) Then the fast relaxation of the electron spin, $M = +\frac{1}{2} \rightarrow M = -\frac{1}{2}$, occurs because electron has a large magnetic moment and its relaxation time is about a millisecond. On the other hand, the relaxation time of a nuclear spin is of the order of second or more. Before the nuclear spin relaxes back to the thermal equilibrium state, the electron can relax to $M = -\frac{1}{2}$ and couple to another nucleus. Then the transitions $|4\rangle \rightarrow |2\rangle$ and $|5\rangle \rightarrow |3\rangle$ take place in the new pair, followed by the fast relaxation of the electron spin. In this manner, the spin system which was initially at the state $|4\rangle$ ($|5\rangle$) moves to the state $|5\rangle$ ($|6\rangle$) via state $|2\rangle$ ($|3\rangle$). Keeping trace the nuclear spin state m , such a process means the change from $m = -1$ ($|4\rangle$) to $m = 0$ ($|5\rangle$) and from $m = 0$ ($|5\rangle$) to $m = +1$ ($|4\rangle$), which is the enhancement of the positive polarization. Similarly, the negative polarization can be obtained by irradiating the system with an rf field of $\omega_{rf} \sim \omega_e + \omega_I$ inducing the forbidden transitions $|6\rangle \rightarrow |2\rangle$ and $|5\rangle \rightarrow |1\rangle$.

This mechanism gives one important implication for the material preparation, the typical amount of unpaired electrons. The key question is 'how many nuclei should one electron couple to while one nuclear spin thermally relaxes?'. The answer is the ratio of the relaxation time of a electron spin to that of a nuclear spin, (milliseconds)/(order of seconds) $\sim 10^{-4} - 10^{-3}$. The typical concentration of the paramagnetic center is 10^{-4} - 10^{-3} unpaired electrons/nuclei.

4.1.5 Macroscopic effects

The DNP mechanism in the previous section works only between the nucleus and the electron which are located closely because the transition probability is proportional to $|\varepsilon|^2 \propto r^{-6}$. However, there is a dipolar-dipolar spin coupling between nuclei also. The simultaneous spin flipping of two nuclear spins, where the change of the one spin state is $\Delta m = +1$ and that of the other is $\Delta m = -1$, is possible. The probability of such simultaneous spin flipping is considered to be rather high because the energy is conserved, i.e. one nuclear spin loses the energy $\hbar\omega_I$ and the other gains $\hbar\omega_I$. In this way, the enhanced nuclear polarization near the electron is distributed throughout the material. This phenomenon is called *spin diffusion*. If the spin diffusion is too slow, the entire polarization of the material is limited and there will be an inhomogeneity in the material.

In the previous section, it is mentioned that the energy levels are not sharp anymore taking the dipolar-dipolar interaction between the electrons

and the random orientation of the material. Information on this aspect can be obtained by electron paramagnetic resonance (EPR) technique which shows the microwave absorption by electron spins (transitions involving electron spin flip) in a certain magnetic field. If peaks corresponding to the allowed or forbidden transitions are overlapped in the EPR spectrum (which means the energy levels of $|1\rangle$, $|2\rangle$, and $|3\rangle$ are widened and overlapped each other. And those of $|4\rangle$, $|5\rangle$, and $|6\rangle$ are too.), a rf field with a certain frequency induces the forbidden transitions both for positive DNP and for negative as well as the allowed transitions at the same time. In such a case, the maximum achievable polarization is reduced because the positive and negative DNP compete each other and the rf pumping is not efficient. If the peaks in the EPR spectrum are well separated, preferred transitions can be chosen by a single rf frequency. The DNP in such a case is called *resolved solid effect*. If the peaks are slightly overlapped, it is called *differential solid effect* or *partial solid effect*. The most of the polarized target material used so far, including that for the COMPASS experiment, are considered to be polarized by differential solid effect.

The discussion in the previous paragraph imposes some requirements on the experimental hardware. The overlaps of the energy levels should be minimized. This means that the homogeneity of the magnetic field must be better than $\sim \hbar\omega_I/\hbar\omega_e \sim 2 \cdot 10^{-4}$ over the target material volume. This is one main argument why the magnetic field homogeneity for polarized target is usually specified to be better than $1 \cdot 10^{-4}$. Similarly, the rf field, practically the microwave source, must have sharp monochromatic spectrum better than $\sim \hbar\omega_I/\hbar\omega_e \sim 2 \cdot 10^{-4}$ in order not to induce unwanted transitions.

4.1.6 Hyperfine interaction

The DNP process of the polarized target material so far is usually explained via dipolar-dipolar interaction between the nuclear and the electron spins described in Section 4.1.4. Here, I would like to discuss the possibility and the characteristics of DNP works keeping the relation

A motivation to discuss the DNP process via HFI is the EPR (Electron Paramagnetic Resonance) spectrum in Figure 4.14. The paramagnetic center in ${}^6\text{LiD}$ is considered as the F-center, i.e. an unpaired electron captured in a deuterium site. The 13-line pattern corresponds to the total magnetic quantum number of the six adjacent ${}^6\text{Li}$ nuclei, which can be $-6, -5, \dots, +6$. The interval of the lines is about 0.38 mT. This can be considered as the size of HFI. For a detailed discussion of paramagnetic resonance of

F-center, see Ref. [101, 103].

The possibility that such a 13-line pattern is produced by Zeeman splitting or by a dipolar-dipolar interaction can be eliminated as follows.

The Zeeman splitting for an electron spin and a nuclear spin causes the 6 energy levels shown in Eq. (4.10). The 3 allowed transitions where only electron spins flip $(\pm\frac{1}{2}, m) \rightarrow (\mp\frac{1}{2}, m)$ have one common energy gap $\hbar\omega_e$. In other words, the resonance lines corresponding to these 3 allowed transitions are overlapped in EPR spectrum. Same is true when one electron spin and six adjacent ${}^6\text{Li}$ spins are considered. Zeeman splitting does not produce multiple lines in EPR spectrum.

The dipolar-dipolar interaction between nuclear and electron spins could produce 13-line pattern, but it would be narrower than the spectrum seen in Figure 4.14 and would be practically invisible due to the continuous shape. The additional local field dB_I at a electron spin produced by one of the neighbor nuclear spins is [100]

$$dB_I = \frac{\mu_0}{4\pi} \frac{3 \cos^2(\theta) - 1}{r_j^3} \sqrt{I(I+1)} \mu_I \frac{m_I}{I} \quad , \quad (4.29)$$

where θ is the angle between the external field B_0 and the vector \vec{r}_j which points from the electron to the nuclei. In the case of ${}^6\text{LiD}$, the nuclei in question is ${}^6\text{Li}$ ($I = 1$) located $2 \cdot 10^{-10}$ m away from the electron, resulting in $dB_I = 1.5 \cdot 10^{-4}$ T. The allowed transition will appear in the EPR spectrum with an interval of $2dB = 2.9$ mT for the case $\theta = 0$, which could give the maximum interval. In addition, the sample material used for the EPR measurement of Figure 4.14 can be considered to be the composition of the random combination of regular sub-crystals and the EPR spectrum is considered to be the integral over the angle θ . Thus the measured interval 3.8 mT is too large to explain by the dipolar-dipolar interaction.

The dipolar-dipolar broadening is not the subject of this section but is worthwhile to look at for better understanding of EPR spectrum. The width of the dipolar-dipolar broadening is analyzed in [102]. The EPR spectrum of F-centers in ${}^6\text{LiD}$ can be considered as the case that the material has a regular lattice structure and contains sections which are oriented randomly. The breadth σ_B (one sigma of Gaussian) of EPR spectrum is

$$\sigma_B = \sqrt{\langle(\sigma_B)^2\rangle_{{}^6\text{Li}} + \langle(\sigma_B)^2\rangle_{\text{D}} + \langle(\sigma_B)^2\rangle_{\text{e}}} \quad (4.30)$$

with

$$\langle(\sigma_B)^2\rangle_X = \frac{4}{15} \left(\frac{\mu_0}{4\pi} g_X \mu_N \right)^2 I_X(I_X + 1) \sum_j \frac{1}{r_{Xj}^6} \quad (4.31)$$

$$\langle(\sigma_B)^2\rangle_e = \frac{3}{5} \left(\frac{\mu_0}{4\pi} g_e \mu_B \right)^2 S(S+1) \sum_k \frac{1}{r_{ek}^6} , \quad (4.32)$$

where X refers deuterons or ${}^6\text{Li}$, I_X is the spin of nuclei X (here, $I_X = 1$), and r_X is the distance from a unpaired electron to the nuclei at j -th site. Similarly, S is the electron spin, i.e. $1/2$, and r_E is the distance from an unpaired electron to the one of the other unpaired electron at k -th site. Here, it is assumed that the unpaired electrons are distributed uniformly at equal distance of $15.7b$ following the F-center concentration $2 \cdot 10^{-19}/\text{g}$, where $b = 2.0 \cdot 10^{-10}$ m is the distance between a deuteron site to the neighbor ${}^6\text{Li}$ site. The calculation gives $\Delta B = 0.16$ mT, which is consistent with the breadth of each structure of 13-line pattern in Figure 4.14.

From now on, the possibility of DNP via HFI is discussed in a similar manner to Section 4.1.4. The Hamiltonian counting the Zeeman splitting and HFI between an unpaired electron spin S and a neighbor nuclear spin I (${}^6\text{Li}$ with $I = 1$) is [94]

$$\mathcal{H} = g_{\parallel} \mu_B B_0 M - g_I \mu_N B_0 m + AmM + \frac{1}{2} A' (S_- I_+ + S_+ I_-) \quad (4.33)$$

for a simple case that the one of the principal axes of the lattice z' is parallel to the external magnetic field B_0 , where z' is defined by g_{\parallel} parallel g-factor of the electron. As a general discussion, a possible anisotropy is considered but the context does not change. The last terms expresses the HFI

$$\mathcal{H}_{\text{HFI}} = AmM + \frac{1}{2} A' (S_- I_+ + S_+ I_-) . \quad (4.34)$$

The HFI admixes the pure Zeeman states slightly. Since the electron Zeeman energy is larger than HFI energy by a factor 100 or more, the perturbation theory can be applied and the Zeeman pure state kets $|M, m\rangle$ can be used as zero-order state kets. Like in Section 4.1.4, let $|n^0\rangle$ ($n = 1, 2, \dots, 6$) denote the pure Zeeman state $|Mm\rangle$, making $|1^0\rangle$ refer the highest energy state, $|2^0\rangle$ the second highest ..., and $|6^0\rangle$ the lowest energy state.

The first-order perturbed states $|n\rangle$ can be calculated by Eq. (4.19) with a replacement $\mathcal{H}_{\text{DDI}} \rightarrow \mathcal{H}_{\text{HFI}}$. After renormalization so that $\langle n|n\rangle = 1$, they are

$$\begin{aligned} |1\rangle &= (|+-\rangle + q|-0\rangle)/\sqrt{1+q^2} \\ |2\rangle &= (|+0\rangle + q|--\rangle)/\sqrt{1+q^2} \\ |3\rangle &= |++\rangle \end{aligned}$$

$$\begin{aligned}
|4\rangle &= |--\rangle \\
|5\rangle &= (|-0\rangle + q|+-\rangle)/\sqrt{1+q^2} \\
|6\rangle &= (|-+\rangle + q|+0\rangle)/\sqrt{1+q^2} \quad ,
\end{aligned} \tag{4.35}$$

where $q = \frac{A'}{\sqrt{2g_{\parallel}\mu_B B_0}}$. The perturbed energy $E_n = \langle n|\mathcal{H}|n\rangle$ are by Eq. (4.20)

$$\begin{aligned}
E_1 &= \frac{1}{2}g_{\parallel}\mu_B B_0 + g_I\mu_N B_0 - \frac{A}{2} + \frac{A'^2}{2g_{\parallel}\mu_B B_0} \\
E_2 &= \frac{1}{2}g_{\parallel}\mu_B B_0 + \frac{A'^2}{2g_{\parallel}\mu_B B_0} \\
E_3 &= \frac{1}{2}g_{\parallel}\mu_B B_0 - g_I\mu_N B_0 + \frac{A}{2} \\
E_4 &= -\frac{1}{2}g_{\parallel}\mu_B B_0 + g_I\mu_N B_0 + \frac{A}{2} \\
E_5 &= -\frac{1}{2}g_{\parallel}\mu_B B_0 - \frac{A'^2}{2g_{\parallel}\mu_B B_0} \\
E_6 &= -\frac{1}{2}g_{\parallel}\mu_B B_0 - g_I\mu_N B_0 - \frac{A}{2} - \frac{A'^2}{2g_{\parallel}\mu_B B_0} \quad .
\end{aligned} \tag{4.36}$$

Now learn the value A from Figure 4.14. The peaks of allowed transitions $(\frac{1}{2}, m) \leftrightarrow (-\frac{1}{2}, m)$ that appear in the EPR spectrum should have the shifts ΔB from the nominal center

$$\Delta B \sim \frac{E_n - E_{n+3}}{g_{\parallel}\mu_B B_0} - B_0 \quad (n = 1, 2, 3) \quad , \tag{4.37}$$

which are specifically

$$\Delta B \sim -\frac{A}{g_{\parallel}\mu_B B_0} + \frac{1}{2}\left(\frac{A'}{g_{\parallel}\mu_B B_0}\right)^2 \quad \text{for the transition } |1\rangle \leftrightarrow |4\rangle \tag{4.38}$$

$$\Delta B \sim \left(\frac{A'}{g_{\parallel}\mu_B B_0}\right)^2 \quad \text{for the transition } |2\rangle \leftrightarrow |5\rangle \tag{4.39}$$

$$\Delta B \sim +\frac{A}{g_{\parallel}\mu_B B_0} + \frac{1}{2}\left(\frac{A'}{g_{\parallel}\mu_B B_0}\right)^2 \quad \text{for the transition } |3\rangle \leftrightarrow |6\rangle \quad . \tag{4.40}$$

The peaks corresponding to forbidden transitions are much less visible than that for the allowed transitions in the EPR spectrum. Assuming that A' is

at the same order of A and ignoring the term $(A'/g_{\parallel}\mu_B B_0)^2$ in Eq. (4.38)-(4.40), a pair of a electron spin and a spin-1 nuclear spin produces three peaks in the EPR spectrum at $\Delta B = 0$ and $\Delta B = \pm \frac{A}{g_{\parallel}\mu_B B_0}$. The 13 lines in Figure 4.14 can be understood by adding 5 more neighbor ${}^6\text{Li}$ nuclei in Eq. (4.34). The intervals of the lines in Figure 4.14 is about 0.38 mT, which is considered to be equal to $\frac{A}{g_{\parallel}\mu_B B_0}$, giving $A = 7.1 \cdot 10^{-27}$ J. This A value is smaller than the typical values of HFI inside one atom. The reason is considered that an electron in F-center stays in one of the neighbor nuclei at a small probability.

Now look into the probability of the simultaneous spin flipping which is the source of the DNP mechanism. By irradiating the system of one electron spin and one nuclear spin with an rf field,

$$\mathcal{H}_{rf} = g_{\parallel}\mu_B B_{1z}M + \frac{1}{2}g_{\perp}\mu_B \left[(B_{1x} - iB_{1y})S_+ + (B_{1x} + iB_{1y})S_- \right] \quad , \quad (4.41)$$

one can induce the transitions. The probability for forbidden transitions (simultaneous spin flipping), are calculable from Eq. (4.12) and the optimum rf frequency for such transitions are

$$Pr.(6 \rightarrow 2) = W_2 \quad \text{at} \quad \hbar\omega_{rf} = \hbar\omega_e + \hbar\omega_N + \frac{A}{2} + \frac{A'^2}{g_{\parallel}\mu_B B_0} \quad (4.42)$$

$$Pr.(5 \rightarrow 1) = W_2 \quad \text{at} \quad \hbar\omega_{rf} = \hbar\omega_e + \hbar\omega_N - \frac{A}{2} + \frac{A'^2}{g_{\parallel}\mu_B B_0} \quad (4.43)$$

$$Pr.(4 \rightarrow 2) = W_2 \quad \text{at} \quad \hbar\omega_{rf} = \hbar\omega_e - \hbar\omega_N - \frac{A}{2} + \frac{A'^2}{g_{\parallel}\mu_B B_0} \quad (4.44)$$

$$Pr.(5 \rightarrow 3) = W_2 \quad \text{at} \quad \hbar\omega_{rf} = \hbar\omega_e - \hbar\omega_N + \frac{A}{2} + \frac{A'^2}{g_{\parallel}\mu_B B_0} \quad , \quad (4.45)$$

with

$$W_2 \simeq \frac{2\pi}{\hbar} \frac{2g_{\parallel}^2 \mu_B^2 B_{1z}^2}{4} \left(\frac{A'}{g_{\parallel}\mu_B B_0} \right)^2 \quad . \quad (4.46)$$

On the other hand, the transition probability corresponding to the allowed transition where only electron spin flips ($\Delta M = 1$, $\Delta m = 0$) and their optimum frequencies are

$$Pr.(4 \rightarrow 1) = W_1 \quad \text{at} \quad \hbar\omega_{rf} = \hbar\omega_e - A + \frac{A'^2}{2g_{\parallel}\mu_B B_0} \quad (4.47)$$

$$Pr.(5 \rightarrow 2) = W_1 \quad \text{at} \quad \hbar\omega_{rf} = \hbar\omega_e + \frac{A'^2}{g_{\parallel}\mu_B B_0} \quad (4.48)$$

$$Pr.(6 \rightarrow 3) = W_1 \quad \text{at} \quad \hbar\omega_{rf} = \hbar\omega_e + A - \frac{A^2}{2g_{\parallel}\mu_B B_0} \quad (4.49)$$

with

$$W_1 \simeq \frac{2\pi g_{\perp}^2 \mu_B^2 (B_{1x}^2 + B_{2y}^2)}{\hbar} \cdot \quad (4.50)$$

The simultaneous spin flipping is suppressed compared to the allowed transitions by $W_2/W_1 \simeq (A'/g_{\parallel}\mu_B B_0)^2 \simeq 2 \times 10^{-8}$ at $B_0 = 2.5$ T assuming that the anisotropy is very small, i.e. $A \sim A'$ and $g_{\parallel} \simeq g_{\perp} \simeq g_e$, and the random 'mode' in the microwaves, i.e. $B_{1x} \sim B_{1y} \sim B_{1z}$. The probability is very small but is still possible.

The arguments above is for the case $z' \parallel \vec{B}_0$. The other typical case $z' \perp \vec{B}_0$ has the similar context and the transition probabilities W_1 and W_2 are

$$W_1 \simeq \frac{2\pi g_{\parallel}^2 B_{1z}^2 + g_{\perp}^2 B_{1y}^2}{\hbar} \quad (4.51)$$

$$W_2 \simeq \frac{2\pi 2g_{\perp}^2 B_{1z}^2}{\hbar} \left(\frac{A + A'}{2g_{\perp}\mu_B B_0} \right)^2 \quad (4.52)$$

The suppression factor W_2/W_1 is similar to the case $z' \parallel \vec{B}_0$.

As has been seen, the simultaneous spin flipping is suppressed but is still possible. Therefore, DNP can be performed by irradiating the spin system by an rf-field with a right frequency, counting the fast relaxation of electron spins and the slow relaxation of nuclear spins like in the case of DNP via dipolar-dipolar interaction in Section 4.1.4. Since $\hbar\omega_I > \frac{A}{2}$ at $B_0 = 2.5$ T. the right rf frequencies for the positive and negative DNP are

$$\omega_{rf} \simeq \omega_e - \omega_I \quad (4.53)$$

$$\omega_{rf} \simeq \omega_e + \omega_I \quad (4.54)$$

respectively, according to Eq. (4.42)-(4.45) and assuming a reasonable broadening of each energy levels. The DNP mechanism is illustrated in Figure 4.2.

Summarizing, DNP mechanism via HFI does not disturb that via dipolar-dipolar interaction, but is in principle helping, because the optimum microwave frequencies are similar in the two mechanisms (see Section 4.1.4). On the other hand, HFI does not play a dominant role to the total polarization for the following reasons. The transition probability of the forbidden transitions of DNP via HFI is much smaller than that via dipolar-dipolar interaction by factor $(\frac{W_2}{W_1})_{\text{HFI}}/(\frac{W_2}{W_1})_{\text{DDI}} \sim 2 \cdot 10^{-6}$. In addition, DNP via HFI works only between the unpaired electron and the neighbor 6 ^6Li nuclei, not

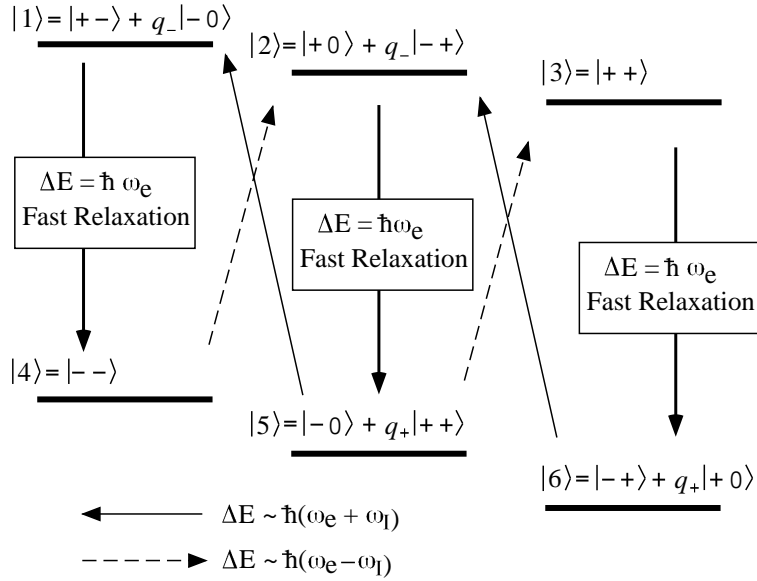


Fig. 4.2: Illustration of the spin states and the DNP mechanism via hyperfine interaction in a pair of an electron spin and a nuclear spin. For simplicity, the spin states are indicated without renormalization. The spin states with renormalization can be found in Eq. (4.35).

between the unpaired electron and the deuterons near-by. And spin diffusion from ${}^6\text{Li}$ nuclei to deuterons are not as efficient as that between the same nuclear species, since the Zeeman energies are slightly different each other. Thus high deuteron polarization can not be expected. Overall, it is reasonable to consider that the high polarization of ${}^6\text{LiD}$ is achieved by DNP via dipolar-dipolar interaction.

4.1.7 Equal spin temperature

If the population distribution of a certain spin system I follows the Boltzmann statistics even after enhancement of the polarization via DNP mechanism, one can use Brillouin function Eq. 4.5 by replacing T with a *spin temperature* T_{ss} . (Practically, the spin temperature T_{ss} can be determined by the actual polarization P .) In the spin- $\frac{1}{2}$ system, there is no need to discuss the applicability of Boltzmann statistics. On the other hand, it is not straightforward for spin system with $I \geq 1$ because the definition of the polarization Eq. 4.1 does not guarantee the Boltzmann statistics. However,

it has been shown experimentally that Boltzmann statistics still hold in the spin-1 system during DNP process in many substances from the analysis of the interaction between the electric quadrupole moment and the electric gradient in the atomic bonds [103, 104, 105, 106].

In the substances which contains multiple nuclear spin species, the polarization values are different each other. From the view of the experimental setup as well as for the better understanding of the characteristics of the spins, there is one important concept *Equal Spin Temperature* (EST) which says all the different spin species share one common spin temperature T_{SS} . Rigorous discussion and the mechanism behind the EST can be found for example in [93, 95, 96, 107]. Its basic idea is that spins are strongly coupled and have the separate reservoir other than the Zeeman reservoir. According to the EST concept, the polarizations of the every nuclear species can be expressed simply by Brillouin function

$$P = B_I(\alpha) = \frac{1}{I} \left[\left(I + \frac{1}{2} \right) \coth \left(\left(I + \frac{1}{2} \right) \alpha \right) - \frac{1}{2} \coth \left(\frac{1}{2} \right) \right] , \quad (4.55)$$

where $\alpha = \hbar\omega_I/k_B T = \mu_I B_0 / I k_B T_{SS}$. In spite of the complications of DNP mechanism, it was found that EST concept holds between ^{14}N (spin-1, $\mu_{^{14}\text{N}} = +0.4037$) and protons p (spin- $\frac{1}{2}$, $\mu_p = +2.793$) in ammonia NH_3 while they have different spin numbers and different magnetic moments [104, 105, 108].

^6LiD used in the COMPASS experiment contains principally deuterons and ^6Li but contains their isotopes proton (0.2-0.3% with respect to the total deuteron sites) and ^7Li (4-5% with respect to the ^6Li sites). By the group of E155 collaboration, EST of ^6LiD is verified below 30% polarization [109]. The validity of the EST concept at higher polarization is tested and the benefits from it are discussed in Section 4.5.4.

4.2 The polarization measurement

4.2.1 Nuclear magnetic resonance

In this section, the basics and the results of the theory of nuclear magnetic resonance (NMR) are presented with an orientation of its application to the COMPASS polarized target system. More general and detail aspects are covered in Ref. [93, 104].

When the nuclei with spin- I are placed in the external magnetic field B_0 pointing along z -axis, Zeeman splitting will occur. The ensemble of the spin dipoles in such a field has a magnetization M per unit volume proportional to the external field B_0 ,

$$M = \chi_0 B_0 \quad , \quad (4.56)$$

where χ_0 is called *static susceptibility*. The magnetization M of the spin system is linked to the polarization P by the relation

$$M = \mu N P \quad , \quad (4.57)$$

where N is the number of dipoles per unit volume. The accuracy to measure the polarization P by Eq. (4.57) is limited by the uncertainty in measuring M and N . Since the magnetization M is too small to measure accurately, such an approach is not useful.

NMR technique is used in order to determine the polarization by measuring the nuclear susceptibility χ accurately and linking it to the polarization. When a small rf field is superimposed onto the static magnetic field B_0 , the susceptibility is not a constant any more but depends on the frequency of the rf field (photons) and has both real and imaginary parts,

$$\chi(\omega) = \chi'(\omega) - \chi''(\omega) \quad , \quad (4.58)$$

where χ' is called *dispersion function* and χ'' is *absorption function*. The magnitude of the susceptibility increases drastically when the rf (photon) frequency is in the region of the Larmor frequency because the photons induce transitions between the energy levels. In such a case, the dipoles can absorb photons and climb up to higher energy levels or emit photons and fall down to lower energy levels with equal probability. If there is positive (negative) polarization of the ensemble, there will be a net absorption (emission) of energy. If the rf field is generated by a coil of wire, the change in the magnetic energy of the ensemble due to the photon absorption (emission) manifests itself as a change in the impedance of the coil. Measuring the change in impedance and relating it to the susceptibility is described in Section 4.2.2.

In the rest of this section, consider the relation between the polarization and the susceptibility. The dispersion function and the absorption function satisfy Kramers-Krönig relation [93],

$$\chi'(\omega) = \frac{1}{\pi} \mathcal{P} \int_{-\infty}^{\infty} \frac{\chi''(\omega')}{\omega' - \omega} d\omega' , \quad \chi''(\omega) = -\frac{1}{\pi} \mathcal{P} \int_{-\infty}^{\infty} \frac{\chi'(\omega')}{\omega' - \omega} d\omega' , \quad (4.59)$$

where the symbol $\mathcal{P} \int$ means that the principal part of the integral should be taken. Calculating the case $\omega = 0$ in the first Kramers-Krönig relation reads

$$\chi'(0) \equiv \chi_0 = \frac{2}{\pi} \mathcal{P} \int_{-\infty}^{\infty} \frac{\chi''(\omega')}{\omega'} d\omega' . \quad (4.60)$$

Remembering that the magnetization is written $M = \chi_0 B_0 = g_I \mu_N N P$ and also that $\hbar \omega_0 I = g_I \mu_N B_0$, the polarization can be written

$$P = \frac{B_0}{g_I \mu_N N} \chi_0 = \left(\frac{2\hbar I}{g_I^2 \mu_N^2 N \pi} \right) \mathcal{P} \int_{-\infty}^{\infty} \frac{\omega_0 \chi''(\omega')}{\omega'} d\omega' \propto \int \frac{\omega_0 \chi''(\omega')}{\omega'} d\omega' . \quad (4.61)$$

Thus, one can measure the polarization by measuring the absorption function where it is non-zero and integrating it. This is the basic idea of the area method summarized in Section 4.2.3.

4.2.2 Detection of the absorption function

The polarization can be determined by the measurement of the absorption function as in Eq. (4.61). In this section, the electronics circuit for the detection of the absorption function and its output signal are described.

series LRC resonance circuit

The absorption function χ'' can be detected through the inductive coupling between the nuclear spins and a coil of wire. Consider the coil surrounds the target material and its axis is along x -axis. A current $i = i_0 e^{i\omega t}$ in a coil produces a rf field $B_{1x} = 2B_1 \text{Re}\{e^{i\omega t}\}$ and also induces the nuclear magnetization $M_x = 2B_1 \text{Re}\{\eta \chi e^{i\omega t}\}$, where η is the volume fraction occupied by the material with respect to the coil volume and is called the effective filling factor. The magnetization of the material changes the magnetic field along x -axis into $B_{1x} + \mu_0 \eta M_x$. The current in the coil results in $I = i_0 \text{Re}\{[1 + \mu_0 \eta \chi] e^{i\omega t}\}$. The total flux of the rf field across the coil is

$$\Phi = LI = i_0 \text{Re}\{L[1 + \mu_0 \eta \chi] e^{i\omega t}\} , \quad (4.62)$$

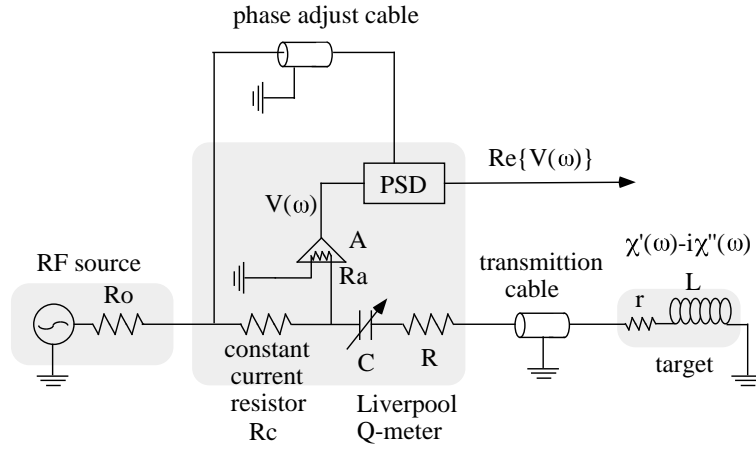


Fig. 4.3: Series LRC resonance circuit for the detection of NMR signals.

which can be interpreted as that the coil inductance L in the absence of any magnetization is changed into

$$L'(\omega) = L[1 + \mu_0\eta\chi(\omega)] \quad (4.63)$$

due to the magnetization of the material. Therefore, the detection of the change in the coil impedance means that of the susceptibility.

Figure 4.3 shows the circuit to detect the absorption function. The change in the coil impedance can be detected by a series RLC resonance circuit with the phase sensitive detector (PSD). For the COMPASS polarized target, so-called Liverpool Q-meter from Ultra-Physics [110] is used. The Q-meter contains the constant current resistor R_c , the variable capacitor C , the dumping resistor R , the rf amplifier with a gain A and the PSD. A frequency synthesizer (denoted as 'RF source' in the figure) sweeps the rf frequency through the Larmor frequency and the Q-meter provides a complex voltage $V = V(\omega, \chi)$, whose real part is selected by the PSD. The Q-meter is tuned with the variable capacitor C so that the resonance condition

$$\omega^2 LC = 1 \quad (4.64)$$

is satisfied at $\omega = \omega_0$, i.e. at the angular Larmor frequency of the nuclear spin.

Counting the resistance r of the coil, the impedance of the coil is

$$Z_c = [r + i\omega L(1 + \mu_0\eta\chi(\omega))] \quad (4.65)$$

The impedance including both the coil and the cable is

$$Z_t = Z_0 \frac{Z_0 \tanh(\gamma l) + Z_c}{Z_0 + Z_c \tanh(\gamma l)} \quad , \quad (4.66)$$

where l is the length of the cable and γ is the complex propagation constant of the cable, which are explained below. The total impedance including the coil, the cable, the dumping resistor R and the capacitor C is

$$Z(\omega, \chi) = R - \frac{i}{\omega C} + Z_t \quad . \quad (4.67)$$

The complex output voltage of the rf-amplifier with a gain A and the input impedance R_a is

$$V(\omega, \chi) = \frac{AV_0}{R_0} \frac{Z(\omega, \chi)}{1 + xZ(\omega, \chi)} \quad , \quad (4.68)$$

where x is the admittance $x = \frac{1}{R_0} + \frac{1}{R_a}$ due to the resistance R_0 and R_a . The length of the phase shifter cable is adjusted so that the PSD should select the real part of the output voltage.

cable effect

Any signal coming from the coil has to go through the transmission cable whose impedance and propagation constant are

$$Z_t = \sqrt{\frac{\mathcal{R} + i\omega\mathcal{L}}{\mathcal{G} + i\omega\mathcal{C}}} \approx \sqrt{\frac{\mathcal{L}}{\mathcal{C}}} = Z_0 = 50\Omega \quad (4.69)$$

and

$$\gamma = \sqrt{(\mathcal{R} + i\omega\mathcal{L})(\mathcal{G} + i\omega\mathcal{C})} \approx \frac{\mathcal{R}}{2Z_0} + i\omega\sqrt{\mathcal{L}\mathcal{C}} \equiv \alpha + i\beta \quad , \quad (4.70)$$

where \mathcal{R} , \mathcal{C} , \mathcal{L} and \mathcal{G} are the resistance, capacitance, inductance and conductance of the cable per unit length. The approximation above is valid when $\mathcal{G} \simeq 0$. The symbols α and β are called *attenuation constant* and *phase constant*, respectively. The phase constant is related to the dielectric constant ϵ_c of the cable by $\beta = \omega\sqrt{\epsilon_c}/c$, where c is the speed of light. The cable used in the COMPASS polarized target has the values $\alpha = 0.024 \text{ m}^{-1}$ and $\epsilon_c = 2.0$. In order to reduce the cable effect, the term $\tanh(\gamma l)$ in Eq. (4.66) should be minimized. With Eq. (4.70), the term $\tanh(\gamma l)$ can be rewritten as

$$\tanh(\gamma l) = \tanh(\alpha l + i\beta l) = \frac{\sinh(2\alpha l) + i \sin(2\beta l)}{\cosh(2\alpha l) + \cos(2\beta l)} \quad . \quad (4.71)$$

The real term increases with l but periodic minima occur when the imaginary part vanishes at $2\beta l = 2n\pi$, where n is an integer. It should be noted that at $2\beta l = (2n + 1)\pi$ minima occur in the numerator while the denominator is very small because $\cos(2\beta l) = -1$ and $\cosh(2\alpha l) \sim 1$. In such a case, the imaginary part of $\tanh(\gamma l)$ changes very rapidly with the sweep of ω , i.e. the sweep of β near $2\beta l = (2n + 1)\pi$. Therefore, the adequate condition for the measurement is not $2\beta l = (2n + 1)\pi$ but $2\beta l = 2n\pi$.

Since the Q-meter sweeps in a small range around the Larmor frequency, the length of the cable should be determined by $2\beta l = 2n\pi$ at the Larmor frequency,

$$l = \frac{n\pi}{\beta} = \frac{n\pi c}{\omega_0 \sqrt{\epsilon_c}} = \frac{n\lambda}{2} \quad , \quad (4.72)$$

where $\lambda = \frac{2\pi c}{\omega_0 \sqrt{\epsilon_c}}$ is the wavelength in the cable. For the measurement of the run 2001 and the run 2002 in the COMPASS polarized target, $n = 1$ is chosen to minimize the attenuation effect in the real part. (Please note that $n=0$ is practically impossible because the target materials are located inside the cryostat.)

Output voltage

The cable effect can be ignored when the cable length is adjusted as $2\beta l = 2n\pi$ and the attenuation factor is very small. For the case that the admittance x is negligible, the output voltage from the Q-meter is

$$\begin{aligned} V(\omega, \chi) &= \left(\frac{AV_0}{R_0} \right) Z(\omega, \chi) \\ &= \left(\frac{AV_0 R}{R_0} \right) \left[1 + \frac{r}{R} + \mu_0 \eta Q_L \chi'' + i Q_L \left(\mu_0 \eta \chi' + \left(1 - \frac{1}{\omega^2 LC} \right) \right) \right] \quad , \end{aligned} \quad (4.73)$$

where $Q_L = \omega L / R$ is the Q value of the circuit. (The PSD in the Q-meter box is tuned so that it should select only the real part. The imaginary part is shown here only for better understanding.) Since the circuit is tuned as in Eq. (4.64) at the angular Larmor frequency $\omega = \omega_0$, the output voltage takes the minimum value at $\omega = \omega_0$ and is approximately symmetric.

When the Larmor frequency is shifted by changing the external magnetic field B_0 slightly and does not match to the tuning of the circuit, magnetization of the material does not affect the circuit, the susceptibility becomes $\chi' = \chi_0$ and $\chi'' = 0$. The output curve in such a case is called *Q-curve* or

baseline and is expressed as

$$V(\omega, \chi) = \left(\frac{AV_0}{R_0}\right) Z(\omega, \chi) = \left(\frac{AV_0R}{R_0}\right) \left[1 + \frac{r}{R} + iQ_L \left(\mu_0\eta\chi_0 + \left(1 - \frac{1}{\omega^2 LC}\right)\right)\right] . \quad (4.74)$$

Subtracting the baseline Eq. (4.74) from the output Eq. (4.73) gives the the signal from the material,

$$V_{\text{sub}}(\omega, \chi) = \left(\frac{AV_0R}{R_0}\right) [\mu_0\eta Q_L [\chi'' + i(\chi' - \chi_0)]] . \quad (4.75)$$

Since the PSD is tuned to select the real part, the subtracted signal is

$$V_{\text{sub}}(\omega, \chi) = \left(\frac{AV_0R}{R_0}\right) [\mu_0\eta Q_L \chi''] . \quad (4.76)$$

Thus, one can obtain the signal which is proportional to the absorption function χ'' . The experimentally measured baseline and subtracted signal are shown in Figure 4.15.

4.2.3 Area method

In this section, a method called *area method* to determine the nuclear polarization is summarized. The basis of this method has been already mentioned above.

As has been seen in Section 4.2.1, the polarization is proportional to the integral of the absorption function,

$$P = \frac{B_0}{g_I \mu_N N} \times \chi_0 = \left(\frac{2\hbar I}{g_I^2 \mu_N^2 N \pi}\right) \mathcal{P} \int_{-\infty}^{\infty} \frac{\omega_0 \chi''(\omega')}{\omega'} d\omega' \propto \int \frac{\omega_0 \chi''(\omega')}{\omega'} d\omega' . \quad (4.77)$$

In the case of deuteron spins or ${}^6\text{Li}$ spins, the width of the absorption function is very narrow (less than 5 kHz), compared to the Larmor frequency $\omega_0/2\pi$ (~ 16 MHz). Therefore, the polarization can be expressed approximately as

$$P \propto \int \chi''(\omega) d\omega . \quad (4.78)$$

On the other hand, the output voltage of the NMR signal is, as considered in Section 4.2.2,

$$V_{\text{sub}}(\omega, \chi) = \left(\frac{AV_0R}{R_0}\right) [\mu_0\eta Q_L \chi''] \quad (4.79)$$

Combining Eq. (4.78) and (4.79), the polarization is proportional to the area S of the NMR signal,

$$P = CS \quad , \quad (4.80)$$

where the factor C contains the number N of spins per unit volume, the effective filling factor η and so on and is not practical to determine from a calculation. The factor C can be calibrated by detecting the NMR signal at thermal equilibrium (TE). Since the polarization P_{TE} at thermal equilibrium can be analytically calculated by Eq. (4.5), the factor C is determined as

$$C = \frac{P_{TE}}{S_{TE}} \quad , \quad (4.81)$$

where S_{TE} is the area of the NMR signal at thermal equilibrium.

The polarization P_{dyn} after dynamic nuclear polarization can be determined as

$$P_{dyn} = \frac{P_{TE}}{S_{TE}} S_{dyn} \quad (4.82)$$

by detecting the NMR signal and calculating its area S_{dyn} .

4.3 Polarized target apparatus

The COMPASS solid polarized target apparatus consists of a dilution refrigerator providing low temperature and high cooling power, a superconducting magnet producing 2.5 T, two 70 GHz microwave systems for DNP and the NMR signal detection system for the polarization monitoring. In Figure 4.4, the side view of the apparatus is shown. The polarized target apparatus in the initial layout of the COMPASS experiment is based on the system build for the SMC (NA47) experiment and a detailed description can be found in Ref. [111] and therein.

Since the polarized target apparatus requires many expertise in each sub system, it is not appropriate to write down all the technical details in this thesis. In this section, only the basic aspects are reported. Our efforts to minimize the amount of material inside the polarized target apparatus for the COMPASS experiment is reported in the context of the microwave cavity in Section 4.3.3. Technical aspects on the superconducting magnet, for which I devoted major part of my major Ph.D days, are described in Chapter 5.

4.3.1 Dilution refrigerator

The dilution refrigerator provides the low temperature and high cooling power. During DNP with microwave irradiation, the dilution refrigerator provides a cooling power of 0.4 watt at 300 mK. Once the microwaves are switched off, the dilution refrigerator cools down the material below 100 mK, which is sufficient to realize *frozen spin mode*, i.e. keep the nuclear spins with the decay constant of ~ 2000 hours at 0.4-0.5 T. The frozen spin technique is one of the essential basis for the spin reversal by field rotation and for the transversely polarized target.

The target materials are placed in the *mixing chamber*, which is located in the bore of the superconducting magnet system, along the axis of the solenoid coil. The mixing chamber is the coolest volume in the refrigerator. Figure 4.5 illustrates the detail view around the target material. The target materials are filled into two target cell, namely upstream target cell and the downstream target cell. Each target cell has a cylindrical shape with a diameter of 30 mm and a length of 600 mm and they are separated by 100 mm. The target cells were fixed to the Kevlar-epoxy cylinder part of the so-called target holder. The material loading into the target cells is done in the separate specially designed liquid nitrogen bath, then the target holder is inserted into the precooled (~ 100 K) mixing chamber from the

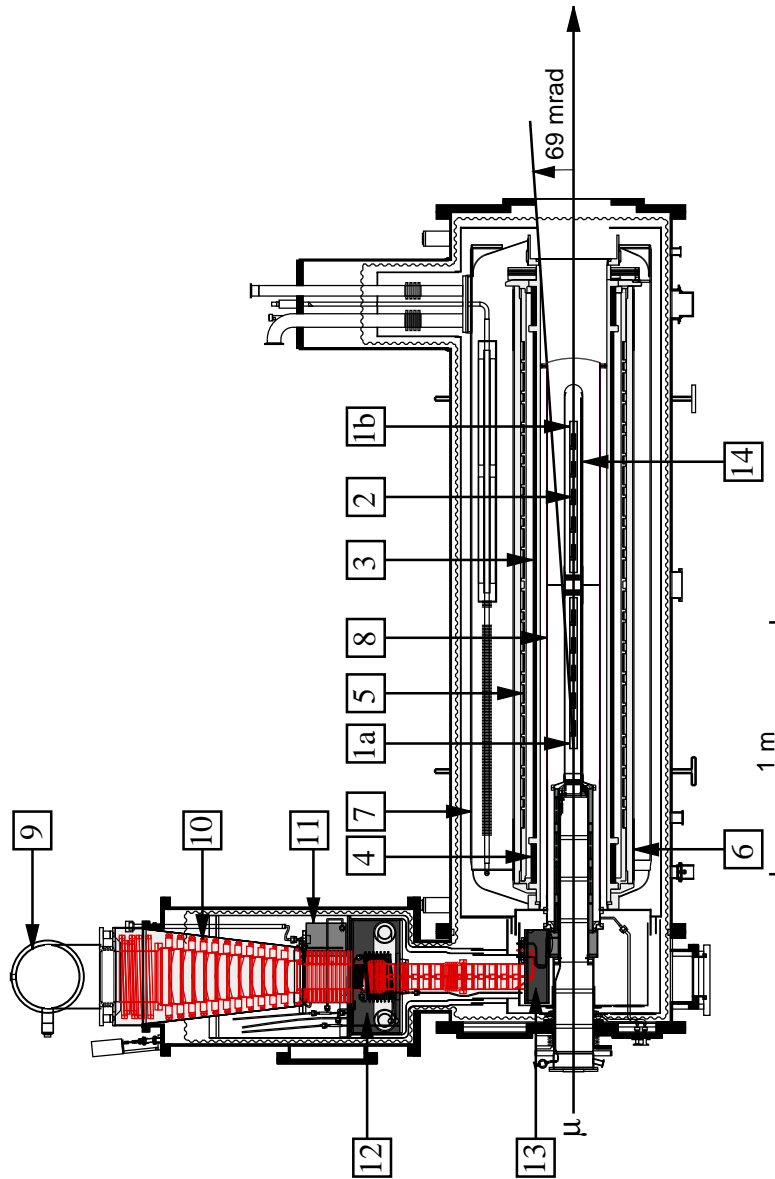


Fig. 4.4: Side view of the COMPASS polarized target apparatus. The muon beam traverses from left to right. The geometrical acceptance for the outgoing particles is 69 mrad in the opening angle from the upstream end of the target cell. (1a) upstream target cell, (1b) downstream target cell, (2) 10 NMR coils inside target material, (3) solenoid coil, (4) compensation coils, (5) 16 correction coils, (6) dipole coil, (7) liquid helium vessel for the magnet, (8) microwave cavity, (9) ^3He pumping port, (10) ^3He precooler, (11) separator, (12) evaporator, (13) still, and (14) mixing chamber.

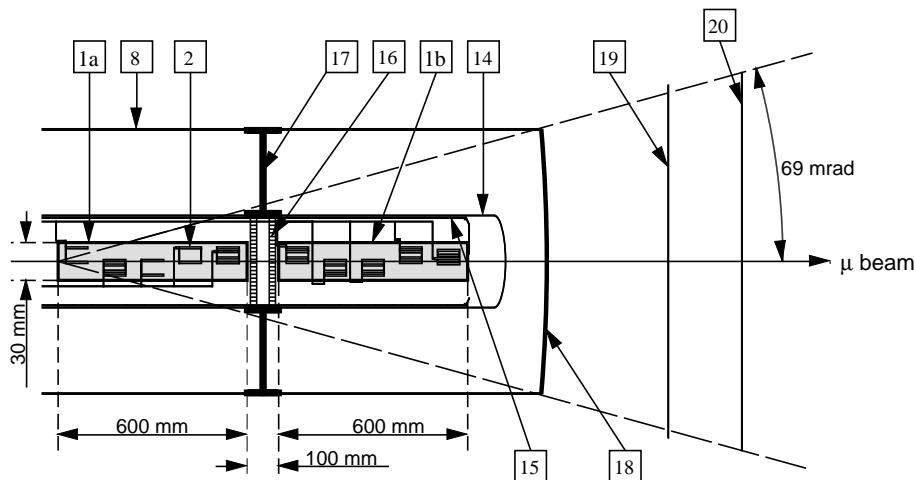


Fig. 4.5: Materials inside the particle detection acceptance including the essential modifications, i.e. the microwave stopper and the target cells. For better illustration, the vertical-horizontal scale is not proportional. (1a) upstream target cell, (1b) downstream target cell, (2) 10 NMR coils inside the target cells, (8) microwave cavity, main cylindrical structure, (14) mixing chamber (glass-fiber-epoxy, $t = 0.06$ mm), (15) target holder support, fitting inside the mixing chamber (kevlar-epoxy, $t = 0.83$ mm), (16) microwave absorbers (polyamid honeycomb with carbon coating) with the reflection mesh (Cu, $t = 0.05$ mm) on their surfaces, (17) microwave stopper (made of $t = 0.1$ mm Cu foil), (18) cavity end window (made of $t = 0.5$ mm Cu foil), (19) magnet radiation shield (Stainless steel, $t = 0.5$ mm), and (20) magnet vacuum window (Al, $t = 1$ mm). Here, t denotes the thickness of each material.

left side of Figure 4.4. This cold target loading is mandate in preventing the paramagnetic center in the target material from decaying due to the warming up.

In the rest of this section, the operation principle of the dilution refrigerator with the practice of the COMPASS apparatus is reported. For general and detail aspects, see for example Ref. [112, 113]. There are 2 separate circuit that are thermally in contact each other. One is called the *precooling circuit* or ${}^4\text{He}$ circuit, the other is called *mixture circuit*, ${}^3\text{He}/{}^4\text{He}$ circuit or simply ${}^3\text{He}$ circuit. A simplified diagram of the COMPASS dilution refrigerator is shown in Figure 4.6.

The precooling circuit is the path for ${}^4\text{He}$ fluid. Liquid ${}^4\text{He}$ is supplied

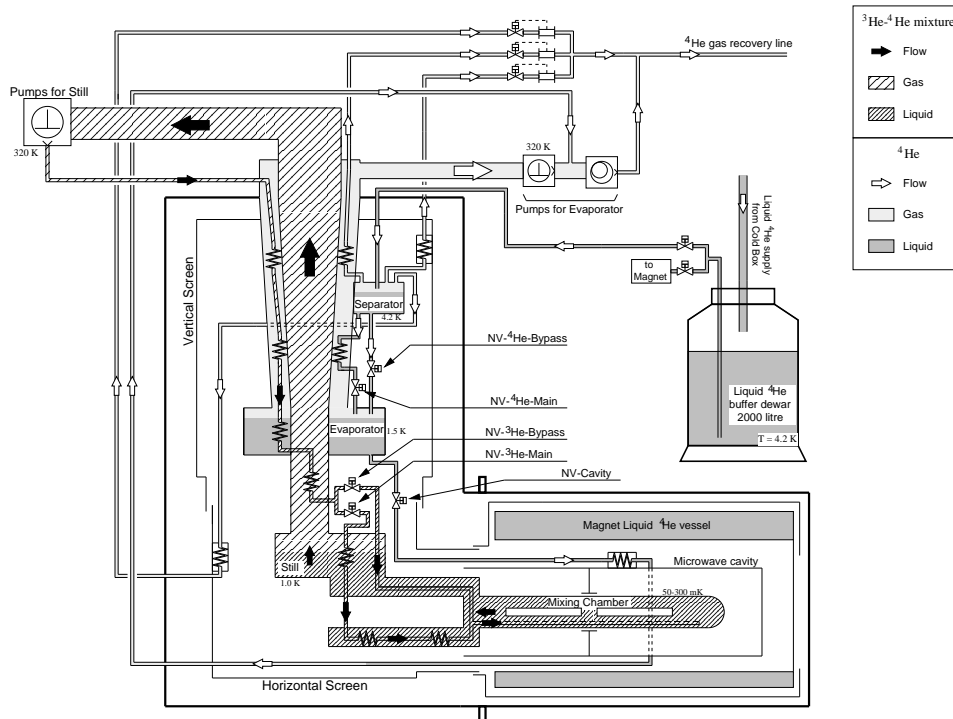


Fig. 4.6: Simplified diagram of the dilution refrigerator in the COMPASS polarized target.

from 'Liquid ^4He buffer dewar' to this precooling circuit. The incoming liquid ^4He enters the vessel called *Separator*. In *Separator* the gaseous ^4He is separated from the liquid due to gravity and the gas is sent to ^4He gas recovery line. The temperature of *Separator* is about 4.2 K, the boiling temperature under the pressure of the recovery line which is 50 mbar higher than the ambient atmospheric pressure. The liquid phase in *Separator* will be distributed to 4 different destinations described below.

- (a) go to *Evaporator* through the heat exchange tube via needle valve NV- ^4He -Main.
- (b) go to *Evaporator* without going through a heat exchange tube via needle valve NV- ^4He -Bypass.
- (c) go to the tube which contacts and cools down *Vertical Screen*, which reduces the heat load to *Separator* and *Evaporator*. The ^4He evaporated

in this path goes to ^4He gas recovery line.

- (d) go to the tube which contacts and cools down *Horizontal Screen* which reduces the heat load to Still and Target Holder. The ^4He evaporated in this path goes to ^4He gas recovery line.

Vertical Screen and Horizontal Screens are cooled down to typically 50-100 K.

The liquid ^4He in the vessel Evaporator (path (a) and (b) above) is forced to be evacuated by 'Pumps for Evaporator'. The path (b) is used in the beginning of the cooling down for the rapid cooling and is usually closed in the steady operation. The path (a) is used for the DNP process and the frozen spin mode. Evaporator itself is the vessel of evaporative cooling whose cooling power is the latent heat of the vaporization times the rate of the gas removal. In the COMPASS polarized target, Pumps for Evaporator have the pumping speed of $2000\text{ m}^3/\text{h}$ and Evaporator is cooled down to about 1.5 K.

From Evaporator, there is one more path. A fraction of liquid ^4He in Evaporator goes to the tube via the needle valve NV-Cavity which contacts and cools down the microwave cavity down to 2.0 K. The ^4He evaporated in this line goes to the point before the rotary pump of Pumps for Evaporator.

The total consumption of ^4He corresponds to liquid boil-off between 15l/h and 40l/h, depending on the circulation rate of the mixture mentioned below.

Hereafter, the subject is the mixture circuit. The incoming $^3\text{He}/^4\text{He}$ mixture is cooled down by the thermal contact with the evaporation gas from Evaporator and goes through the piping inside Evaporator, where the incoming $^3\text{He}/^4\text{He}$ mixture becomes liquid. The liquefied $^3\text{He}/^4\text{He}$ mixture is further cooled down by the evaporation gas from Still mentioned below. Then the $^3\text{He}/^4\text{He}$ liquid is distributed to 2 paths. One is so-called the mixture bypass path, whose flow is controlled by the needle valve NV- ^3He -Bypass, and joins the other mixture main path just before the mixing chamber. The other mixture main path, whose flow is controlled by the needle valve NV- ^3He -Main, goes through the piping in Still and the intensive heat exchanger, then enters the bottom part of the mixing chamber. The mixture bypass path is used only in the beginning of the cooling down from room temperature to helium temperature.

In the mixing chamber, there exist 2 phases of liquid. One is named *Phase I* which is ^3He rich non-superfluid phase and the other is *Phase II* which is ^4He rich superfluid phase. Due to the gravitational effect, relatively heavier Phase II occupies the bottom part of the mixing chamber

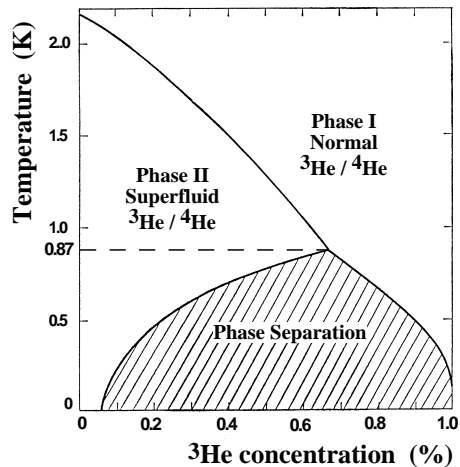


Fig. 4.7: Phase diagram of ^3He - ^4He mixture. The diagram shows the lambda line of the superfluid transition line and the phase separation line of the mixture. Below 0.87 K, the phase separation starts.

and Phase I stays on top of Phase II. Figure 4.7 shows the phase diagram as a function of temperature and ^3He concentration. The phase separation starts at 0.87 K and the ^3He concentration increases (decreases) as the mixing chamber cools down in Phase I (Phase II). By pumping the bottom part of Phase II, practically by pumping Still, ^3He molecules in Phase I dilute into Phase II and will be pumped out. Since the enthalpy of ^3He in Phase II $H_d(T)$ is larger than that in Phase I $H_c(T)$, the molecules absorb the energy from the surrounds, i.e. cool down the surrounds, in diluting into Phase II. Its cooling power \dot{Q} (J/s) is

$$\dot{Q} = \dot{n}_3 [H_d(T) - H_c(T)], \quad (4.83)$$

where \dot{n}_3 is the molar flow rate (mol/s), and $H_d(T)$ and $H_c(T)$ denote the molar enthalpy (J/mol) of ^3He in Phase II and in Phase I, respectively. The difference of enthalpy $H_d(T) - H_c(T)$ is called *heat of mixing*, which analogically corresponds to the latent heat, i.e. the energy that molecules absorb from surroundings in evaporating from liquid phase to gas phase. Since there is at least 6% ^3He concentration in Phase II even when the temperature is approaching to 0 K, the cooling of the mixing chamber theoretically continues infinitely. (Practically, it is limited by the heat load and the pumping capability to produce \dot{n}_3 in Eq. (4.83).) In the COMPASS polarized target, the mixing chamber temperature was 0.1-0.3 K during DNP process and was

about 80-100 mK without microwave pumping for DNP, i.e. during frozen spin mode.

The liquid ^3He pumped out from Phase II in the mixing chamber travels through the heat exchanger and fills up the vessel *Still*. The liquid in the still is subject to the evaporative cooling. In the COMPASS polarized target, the Pumps for Still has the pumping speed of $13\,500\text{ m}^3/\text{h}$ for ^3He . The pumped gas is re-sent to the mixture circuit of the dilution refrigerator again and circulates. In order to gain n_3 in Eq. (4.83), a heater is installed in the still and is fired appropriately. The operating temperature of the still is typically 1.0 K. Since the vapor pressure of ^3He is much larger than that of ^4He , ^3He is mainly pumped out from Still and circulating. The flow rate of the mixture is 27-350 mmol/s depending on the operation.

4.3.2 Superconducting magnet

In this section, the characteristics of the magnet system is reported. Technical aspects are described in Chapter 5.

The superconducting magnet system produces a longitudinal (horizontal) 2.5 T solenoid field and a transverse (vertical) 0.5 T dipole field. The coils are in the liquid helium bath and the superconductivity is realized.

The power supply for the main solenoid coil is bipolar, making it possible to choose the parallel or anti-parallel longitudinal field. A field homogeneity of $\Delta B/B = \pm 3 \cdot 10^{-5}$, is achieved with the appropriate tuning of 16 independent trim coils. In this homogeneous field, high target polarization is built-up by dynamic nuclear polarization with microwaves (see Section 4.1).

The dipole field is produced by the saddle shape coils with the moderate homogeneity. The power supply for the dipole coil is unipolar and the direction is only one way.

The special feature of this magnet system is so-called *field rotation* which results in the *spin reversal* of the target polarizations, from (a) to (b) (or from (c) to (d)) in Figure 3.8 and vice versa. The field rotation is based on the nature that the pointing directions of spins follows the rotation of the external magnetic field as long as the rotation frequency is much slower than the Larmor frequencies (see Section 4.1.2) of the spins, i.e. as long as the external magnetic field is 'static' enough from the view of the spins. Since the Larmor frequency of the nuclear magneton μ_N is $\mu_N B/h = 4\text{ MHz}$ at 0.5 T, a rotation by any magnet devices is 'slow' enough. In the COMPASS polarized target, one spin reversal by field rotation can be completed in about 33 minutes, which helps the reduction of the systematic error in the particle physics experiment due to the different spectrometer acceptance of the two

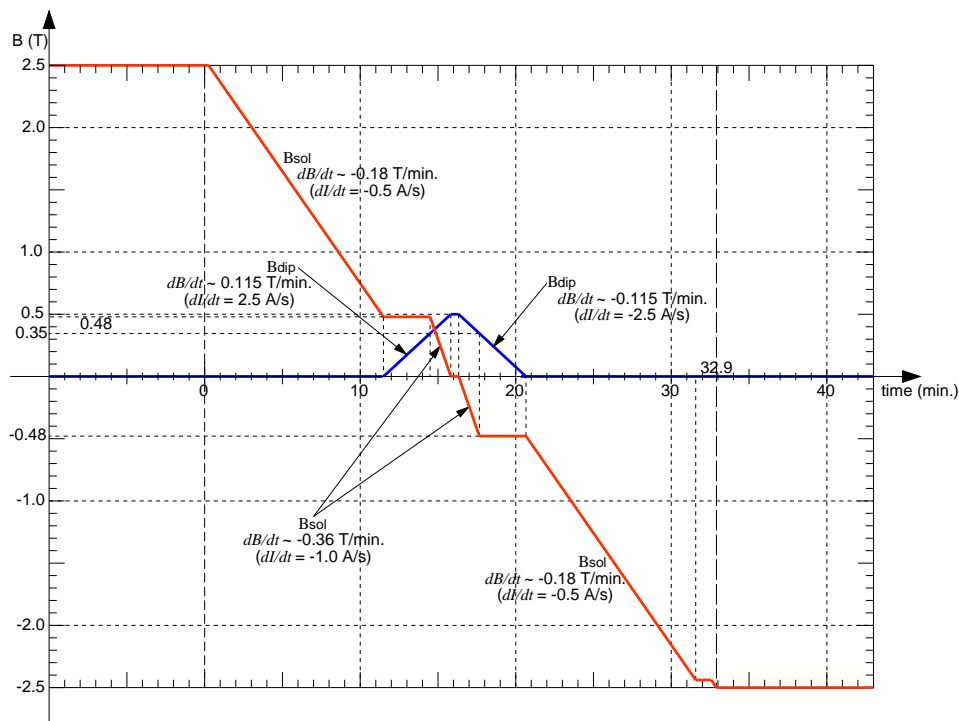


Fig. 4.8: Operation of the solenoid and the dipole field during the field rotation from +2.5 T to -2.5 T. The rotation from -2.5 T to +2.5 T can be performed similarly.

target cells and due to the time dependent variation of the spectrometer efficiency. The spin reversal by field rotation is performed every 8-12 hours. (The spin reversal by DNP with microwaves takes about a week to reach the maximum polarization and is not adequate for frequent spin reversals like a few times per day. However, it must be performed at least once during the data taking in order to move from (a) to (c) or vice-versa in 3.8.)

Practically, field rotation is realized by the combinatorial operation of the solenoid and the dipole system. Their operation versus time is shown in Figure 4.8 and the magnetic field during the field rotation is shown in Figure 4.9. Before $t = 0$, microwave irradiation and automatic NMR data taking are stopped. At $t = 0$, the sequence of field rotation is started and it continues until $t = 31.5$ min automatically. Meanwhile, at $t = 0$ bad homogeneity of solenoid field is intentionally produced by detuning the correction coil currents, practically by changing the polarity of them, in order to

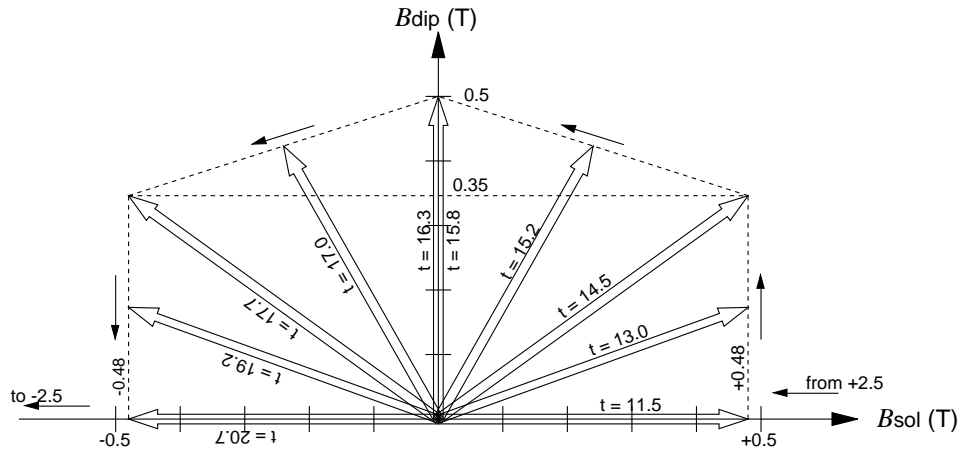


Fig. 4.9: Side view of the magnetic field during the field rotation. t refers the timing in Figure 4.8. This side view can superimpose to Figure 4.4.

prevent 'superradiance' (spontaneous rapid decay of negative polarization) which was observed in the proton target in the SMC experiment. In the COMPASS experiment with ${}^6\text{LiD}$ material, superradiance has never been observed. Thus, the detuning is employed only for extra safety and for possible future proton target. For the reason that the solenoid and dipole coils experiences strong Lorentz force each other if they are ramped up to high currents at the same time, the dipole field can be ramped up only after the solenoid field reaches 0.48 T. At $t = 15.8$ min, there is only transverse magnetic field by dipole. Then, the correction coil currents are detuned for the negative solenoid field. Then the solenoid current is ramped to the opposite sign in a symmetric manner about $t = 15.8$ min. The before reaching to nominal -2.5 T, the solenoid field is paused at -2.45 T and the baseline of the NMR circuit (see for example Figure 4.15) for the NMR measurements at -2.5 T. After the baseline measurement, the solenoid field is ramped to nominal -2.5 T and the field rotation is completed at $t = 32.9$ min.. Then, automatic NMR data taking and the microwave irradiation for DNP are restarted.

The discussion above concerns the particle physics program with the longitudinally polarized target. The COMPASS experiment contains the physics program with the transversely polarized target program as well. The transverse polarization can be realized by pausing the field rotation at the middle of it, holding the nuclear spin only with the dipole field of

0.4-0.5 T in the frozen spin mode (80-100 mK in the mixing chamber).

4.3.3 Microwave system

High nuclear polarization is produced by DNP mechanism described in Section 4.1, where the simultaneous spin flips of electrons and nuclei play an important role and can be caused by a rf field, practically by the microwave irradiation. Choosing the microwave frequency slightly below (above) the electron Larmor frequency, 70 GHz at a magnetic field of 2.5 T leads to a positive (negative) enhanced nuclear polarization.

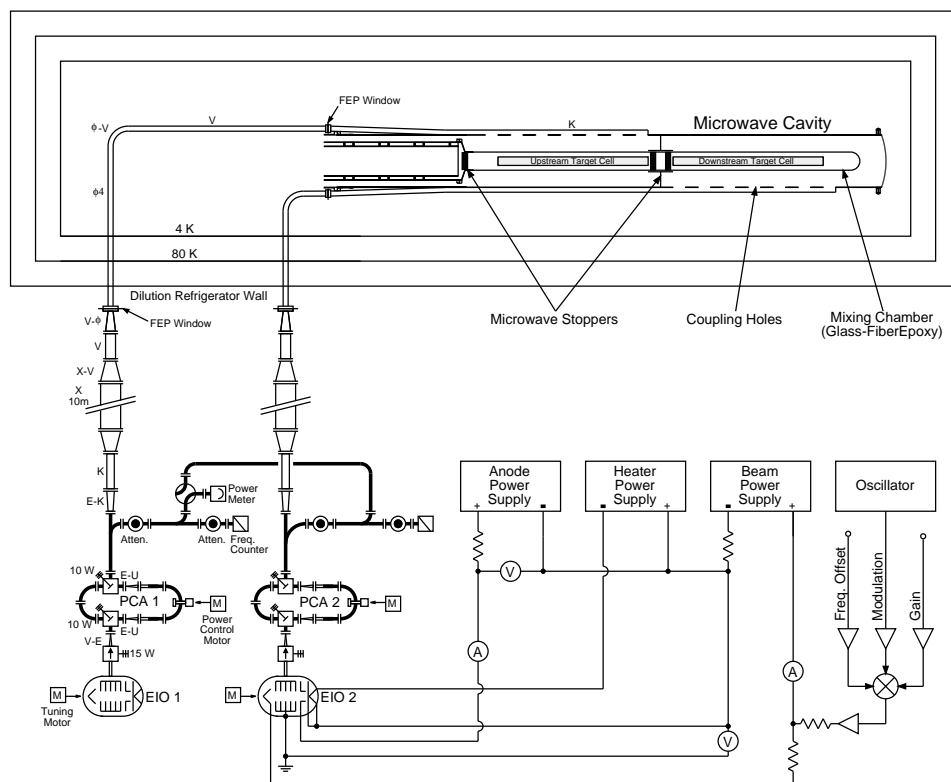


Fig. 4.10: Illustration of the microwave system. EIO stands for Extended Interaction Oscillator, PCA for Power Control Attenuator based on the interferometer technique, V, E and K for the size of the rectangular waveguides and ϕ for the circular waveguide.

In order to polarize the two target cells in opposite directions at the same

Material	ID in Fig. 4.5	X_0 (mm)	$x(69 \text{ mrad})$ (mm)	x/X_0 (%)
$^3\text{He}/^4\text{He}$	–	6740	288	4.3
Mixing chamber	(14)	287	12	4.2
Target holder support	(15)	150	8.7	5.8
Microwave stopper	(17)	14.3	0.1	0.7
Cavity end window	(18)	14.3	0.5	3.5
Magnet radiation shield	(19)	17.6	0.5	2.8
Magnet vacuum window	(20)	88.9	1	1.1
Total				22.4

Tab. 4.1: Thickness of the materials in the polarized target apparatus in radiation lengths X_0 for the outgoing particles with an opening angle of 69 mrad from the upstream end of the target cell. Such particles traverse a length of $x(69 \text{ mrad})$ in each material described in Figure 4.5. Generally, the total x/X_0 varies depending on the vertex point and the outgoing angle. For simplicity, the contribution from the NMR coils, $^3\text{He}/^4\text{He}$ mixture distribution tube inside the mixing chamber, and the superinsulation sheets are ignored.

time, two independent microwave systems are used. In Figure 4.10 Extended Interaction Oscillator (EIO) tubes generate microwaves of 70 GHz with a band width of 0.1 MHz and a maximum power output of 10-20 Watts. The frequency can be fine-tuned by changing the cathode voltage and coarse-tuned by changing the size of the resonant cavity. As reported in Section 4.5.2, additional modulation of the microwave frequencies by 8-30 MHz at a rate of 500 Hz or higher led to an increase of the maximum value of polarization. The modulation of the microwave frequencies is accomplished by applying a 500 Hz sine wave to the cathode voltage with a proper amplitude to modulate the frequency by 8-30 MHz. In order to control the microwave power without disturbing the frequency tuning, interferometers (PCA in Figure 4.10) made of waveguides are used to attenuate the microwaves through destructive interference. Waveguides transfer the microwaves from the EIO tubes through the PCAs to the dilution refrigerator. The power at the entrance of the dilution refrigerator is about 1 Watt.

In the COMPASS experiment, one of the challenges in the polarized target apparatus is the minimization of non-target materials. Since the evaluation of N_{cc}^{\rightarrow} and N_{cc}^{\leftarrow} in Equation 3.2 is based on the reconstruction

from the decay particles of short living hadrons that contain a charm quark, e.g. $D^0 \rightarrow K^- \pi^+$, their multiple scattering should be avoided. On the other hand, the microwave stopper which separates the microwave cavity into two is mandate and be prepared appropriately in order to polarize the two target cells in opposite directions at the same time. In Figure 4.5, the side view of the microwave cavity can be found. The central window of the microwave stopper is made of $100 \mu\text{m}$ Cu foil. The skin depth at 70 GHz for high conductivity copper is less than $0.1 \mu\text{m}$, assuming a residual resistance ratio of 100 between a room temperature and 1 K. Thus the microwave leakage for a simple plane wave is expected to be less than 30 dB. The leakage through the central hole is prevented by the 100 mm long cylindrical part around the mixing chamber made of $100 \mu\text{m}$ Cu foil soldered to the central window foil (see item (17) in Figure 4.5). The gap between the mixing chamber and the cylindrical part is kept below a half of the wavelength to suppress the wave propagation. At room temperature an isolation of better than 20 dB between the two halves of the microwave cavity was measured with this configuration. The downstream end of the cavity has a window of 0.5 mm thick Cu (item (18) in Figure 4.5). The thickness of material is considerably reduced, compared to the SMC experiment. Table 4.1 summarizes the radiation length due to the non-target materials in the detection acceptance.

4.3.4 Nuclear magnetic resonance system

The nuclear polarization was measured by the continuous wave, series LRC Q-meter NMR technique described in Section 4.2. A general schematic outline of the NMR system is shown in Figure 4.11.

5 NMR coils were equally spaced and spirally mounted inside the target cells to probe different parts of the cell equally over the large volume. The coils were made of 1.6 mm diameter non-magnetic CuNi tube with a wall thickness of 0.1 mm and with outer Teflon tube protection.

The RF synthesizer produces the rf signal with a frequency near the Larmor frequency of the nuclear spin of interest. The signal from RF Synthesizer is distributed to the 10 so-called Liverpool Q-meters (see Section 4.2.2 and Ref. [110]). In the Q-meter, Phase Sensitive Detection (PSD) technique is used to pick up the real part of the voltage, i.e. absorption part of the NMR signal. The signal from PSD is sent to DC-offset card, which subtract the DC component for the purpose of the best use of the ADC range. The DC-offset card also has the function of amplification. The PC-VME system controls the frequency sweep of the RF Synthesizer and records the signal data from DC-offset card. The NMR circuits were tuned to 16.38 MHz, Lar-

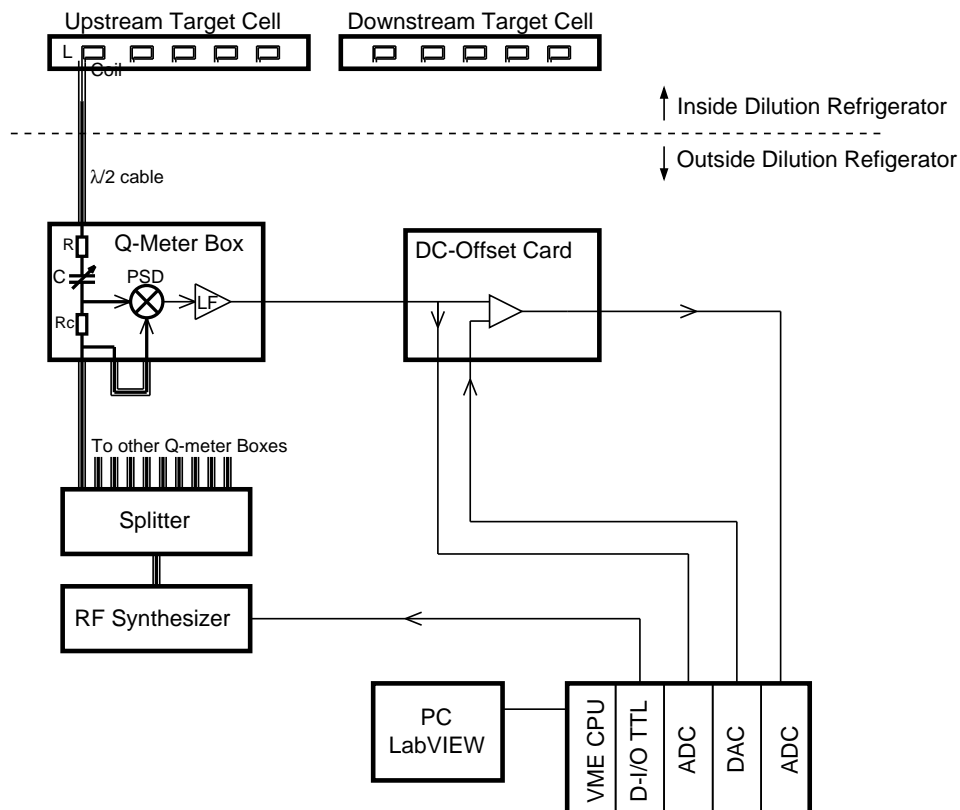


Fig. 4.11: Schematic outline of the NMR system.

mor frequency of deuteron at 2.506 T. The sweep width was ± 0.5 MHz. The same circuit tuning was used for the detection of NMR signals of ${}^6\text{Li}$ and ${}^7\text{Li}$ with a sweep width of ± 0.5 MHz and ± 1.0 MHz respectively, by changing the solenoid field appropriately.

The deuteron NMR signals were taken in 1-5 minutes intervals during the physics data taking.

4.4 Target material ${}^6\text{LiD}$

The target material used in the COMPASS experiment is lithium-6 deuteride ${}^6\text{LiD}$. The development and the mass production for COMPASS experiment have been done by the group of Bochum University. The details relevant to the target material development can be found in Ref. [109, 114, 115, 116, 117, 118, 103, 119, 120] In this section, the motivation to use ${}^6\text{LiD}$ and its characteristics are reported.

The material ${}^6\text{LiD}$ is a crystal with the face-centered cubic structure at room temperature. The dimension of the unit cube is $4 \cdot 10^{-10}$ m, i.e. the distance between a D and a ${}^6\text{Li}$ site is $2 \cdot 10^{-10}$ m, as illustrated in Figure 4.12.

According to the mass spectroscopy, ${}^6\text{LiD}$ used in the COMPASS experiment contains the isotopes, proton (0.2-0.3 % of the nominal deuteron sites) and ${}^7\text{Li}$ (4-5 % of the nominal ${}^6\text{Li}$ sites).

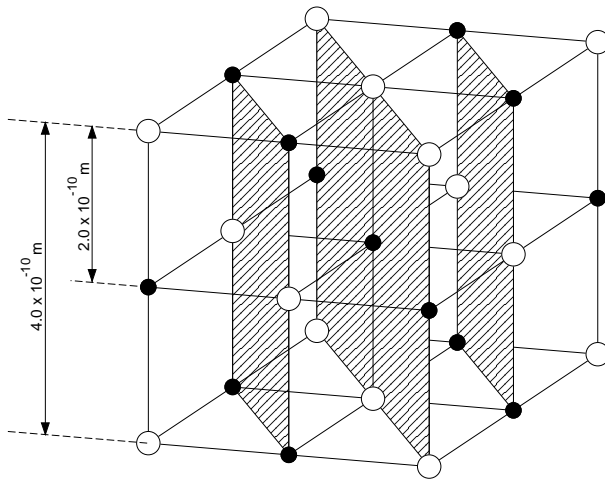


Fig. 4.12: Illustration of the face centered cubic structure of ${}^6\text{LiD}$. The black ball denotes the deuteron site and the white balls the ${}^6\text{Li}$

4.4.1 Choice of the material

A very short explanation for the choice of the material is 'best one that can achieve the physics program with the shortest beam time'. Because of the limited beam intensity and the small cross section of open charm lepto-production, the beam time needed to measure $\Delta g/g$ with an accuracy of

10% is at the order of years as discussed in Section 3.2. This long scale of beam time makes the choice of material important.

The statistical accuracy of experimental double spin asymmetry in Eq. 3.2 is

$$\frac{\delta A^{\text{exp}}}{A^{\text{exp}}} \simeq \frac{1}{\sqrt{2\bar{N}}} \frac{1}{A^{\text{exp}}} = \frac{1}{\sqrt{2\bar{N}} A f P_T P_B} , \quad (4.84)$$

where \bar{N} is the spin averaged number of count $\bar{N} = (N^{\rightarrow} + N^{\leftarrow})/2$, f is the dilution factor discussed below, P_T is the target nucleon polarization which is referred as P_n in this section, and P_B is the muon beam polarization. Here, Eq. (3.3) is used and A is the 'real' physical asymmetry of PGF indicated in Figure 3.1.

The number of count \bar{N} can be expressed as

$$\bar{N} = F_B N_{\text{sc}} t \bar{\sigma} , \quad (4.85)$$

where F_B is the beam flux (number of particles per unit area per unit time), N_{sc} is the number of the scattering center in the beam spot, t is the duration of beam time, and $\bar{\sigma}$ is the spin averaged cross section of interest. The number of the scattering center N_{sc} is expressed with practical numbers as

$$N_{\text{sc}} = \frac{S \ell \kappa \rho N_A N_n}{M_m} , \quad (4.86)$$

where S is the area of beam spot, ℓ is the length of the target cell, κ is the packing factor

$$\kappa = \frac{(\text{volume occupied by the target material})}{(\text{nominal volume of the target cell})} , \quad (4.87)$$

ρ is the density of material, N_A is the Avogadro number, N_n is the number of nucleon per unit molecule, and M_m is the molecular weight of the unit molecule. Here, nucleons are considered as scattering centers because there is no difference in obtaining $\Delta g/g$ from a proton or a nucleon at a first order. Combining Eq. (4.84)-(4.86), the statistical accuracy becomes

$$\frac{\delta A^{\text{exp}}}{A^{\text{exp}}} = \frac{1}{\sqrt{2F_B \frac{S \ell \kappa \rho N_A N_n}{M_m} t \bar{\sigma}}} \frac{1}{A f P_T P_B} . \quad (4.88)$$

Solving this equation about the beam time t ,

$$t = \frac{1}{2F_B P_B^2 \bar{\sigma} A^2 \left(\frac{\delta A^{\text{exp}}}{A^{\text{exp}}}\right)^2 \frac{S \ell N_A N_n}{M_m} F} , \quad (4.89)$$

where figure of merit of the target

$$F = \kappa\rho(fP_T)^2 \quad (4.90)$$

is introduced. Eq. (4.89) says that the beam time needed to achieve a certain statistical accuracy is inversely proportional to the figure of merit of the target. Thus figure of merit is a key factor in the choice of the target material. (The other target related term $\frac{S\ell N_A N_n}{M_m}$ does not vary much depending on the choice of material, since N_n/M_m is nearly unity in all the substances.) ${}^6\text{LiD}$ is chosen for its unrivaled figure of merit because of the following reasons.

- Large fraction of polarizable nucleons with respect to total nucleons.
- High nuclear polarization as high as 50% both in deuteron and ${}^6\text{Li}$ at a magnetic field of 2.5 T.

The figure of merit of ${}^6\text{LiD}$ is discussed in a simple picture and also in a fine picture.

A simple picture

In a simple picture, a ${}^6\text{Li}$ nucleus is considered as being composed of spinless α (${}^4\text{He}$ nuclei) and spin-1 deuteron. The two nucleons out of six nucleons in a ${}^6\text{Li}$ nucleus are polarizable and are responsible for the ${}^6\text{Li}$ nuclear polarization. This picture is justified by the fact that a ${}^6\text{Li}$ nucleus has the spin-1 as a deuteron does and their magnetic moments are similar each other. As for a deuteron, its polarization is considered to be carried by the spin of the internal 2 nucleons. In such a picture, nuclear polarizations are carried by the spin of the polarizable nucleons, i.e. $P_n = P_N$, where P_n is the polarization of the polarizable nucleons and P_N is the nuclear polarization. The dilution factor f is defined as

$$\begin{aligned} f &= \frac{\text{(number of polarizable nucleon in the unit molecule)}}{\text{(number of total nucleon in the unit molecule)}} \\ &= \frac{(2 \text{ from } {}^6\text{Li} + 2 \text{ from D})}{(6 \text{ from } {}^6\text{Li} + 2 \text{ from D})} = 0.5 \quad , \end{aligned} \quad (4.91)$$

Now assume that polarization of both deuteron and ${}^6\text{Li}$ to be 50%, which is at the first approximation justified later in Section 4.5.4. Then, the figure of merit F reads $F = 29 \text{ kg/m}^3$, with the typical packing factor $\kappa = 0.55$ and the density $\rho = 0.84 \cdot 10^3 \text{ kg/m}^3$. This figure of merit is larger than that of ammonia (NH_3), which is the second best one as shown in Table 4.2, by a factor 2.3.

		NH ₃	butanol	d-butanol	⁶ LiD
Polarization of the nuclei	P_N	H: 0.90	H: 0.90	D: 0.50	D: 0.510 H: 0.992 ⁶ Li: 0.493 ⁷ Li: 0.914
Polarization of the nucleons	P_n	0.90	0.90	0.463	0.472 in D 0.992 in H 0.427 in ⁶ Li 0.573 in ⁷ Li
(fractional) dilution factor	f	0.176	0.135	0.238	D: 0.2481 H: 0.0003 ⁶ Li: 0.2375 ⁷ Li: 0.0056
Effective polarization	P_{eff}	0.158	0.122	0.110	0.222
Density (10 ³ kg/m ³)	ρ	0.85	0.99	1.10	0.84
Packing factor	κ	0.60	0.60	0.60	0.55
Figure of merit (kg/m ³)	F	12.7	8.8	8.0	22.8

Tab. 4.2: Comparison of the figure of merit among ⁶LiD and selected common polarized target materials. The nuclear polarization and the packing factor are the typical ones. The density of NH₃, butanol and deuterated butanol (d-butanol) is taken from Ref. [111]. For the clear demonstration of the advantage of ⁶LiD, the small contribution of ⁷Li is ignored and the nuclear polarizations of both the deuteron and the ⁶Li nuclei are assumed to be 50%. The very small contribution of the nitrogen polarization in ammonia is ignored as well.

A fine picture

For precise experiments, one needs to consider how much nuclear polarization is carried by a nucleon spin, which varies depending on the nuclear species. In addition, one needs to count the isotopes of ⁶Li or D, whose polarization are different each other. According to the mass spectroscopy, ⁶LiD used in the COMPASS experiment contains the isotopes, proton (0.2-0.3% of the nominal deuteron sites) and ⁷Li (4-5% of the nominal ⁶Li sites). In this fine picture, it is appropriate to replace fP_T in Eq. (4.90) with the effective polarization P_{eff} defined by

$$P_{eff} = \sum_N f_N P_n \quad , \quad (4.92)$$

where the summation runs over the kind of nuclei of interest and P_n is the polarization of the polarizable nucleon in nuclei N . Since it is known that the nucleon spin is not entirely responsible for the parent nuclear spin, P_n can be defined as $P_n = x_n P_N$, where x_n denotes the fraction of which the nucleon spin is responsible. Now the dilution factor f_N is defined as

$$f_N = \frac{(\text{number of polarizable nucleons in a nuclei } N \text{ in the unit molecule})}{(\text{number of nucleons in the unit molecule})} . \quad (4.93)$$

From these considerations, the figure of merit Eq. (4.90) can be rewritten into

$$F = \rho \kappa P_{eff}^2 = \rho \kappa \left(\sum_N f_N x_N P_N \right)^2 . \quad (4.94)$$

The nuclear polarizations P_N can be obtained by the EST concept once the polarization of one nuclear species is measured, which is explained in Section 4.1.7 and justified in Section 4.5.4.

In evaluating the figure of merit Eq. (4.94), the knowledge on x_N for each nucleus is necessary.

The simplest nucleus is a proton. Since a proton is a nucleon and a nucleus at the same time, $x_p = 1$.

In a deuteron, a proton and a neutron are in a S-state or in a D-state with the probability of 95.1 % and 4.9 %, respectively. When two nucleons are in S-state, there is no need to consider angular momentum effect and the nucleon spin appears as the nuclear spin. On the other hand, if two nucleons are in D-state, their spins are aligned oppositely to the nuclear spin at net 50 % of the time. Consequently,

$$P_n = \left(S - \frac{1}{2}D \right) P_N = 0.9265 P_N , \quad (4.95)$$

where S and D denotes the probability that two nucleons are in S- and D-state, respectively. The result is $x_D = 0.926 \pm 0.016$ considering the slight variation in the data and the theoretical description [121].

A ${}^6\text{Li}$ nucleus can be regarded as being composed of a spinless α particle plus a proton and a neutron, that are carrying the total spin-1 of the nucleus. Unlike a deuteron, the nucleons inside a ${}^6\text{Li}$ nucleus can be found also in a P - and P' -state. For such a three body system,

$$P_n = \left(S + \frac{1}{2}P + 0 \cdot P' - \frac{1}{2}D \right) P_N , \quad (4.96)$$

where P and P' denote the probability that three bodies are in P - and P' -state, respectively. Eight of the models in Ref. [109, 121] give similar results and their average leads $x_{6\text{Li}} = 0.866 \pm 0.012$.

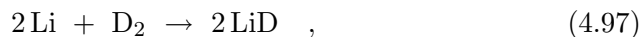
A ${}^7\text{Li}$ is well described as the two body system of a spinless α and spin- $\frac{1}{2}$ triton [122]. This idea allows the nucleon polarization in ${}^7\text{Li}$ to be described based on the nucleon polarization in a triton. In a ${}^3\text{H}$ nucleus, 94% of ${}^3\text{H}$ nuclear polarization is carried by a triton spin. The two body system of α and triton form an $I = \frac{3}{2}$ where the spin of the triton is aligned parallel to the ${}^7\text{Li}$ at net 2/3 of the time. This consideration leads that the proton spin in a triton carries $x_{7\text{Li}} = (62.7 \pm 1.4)\%$ of the parent ${}^7\text{Li}$ spin. [109].

For the case of our isotope contamination, that protons occupies 0.25% of the nominal deuteron sites and ${}^7\text{Li}$ does 4.5% of the nominal lithium sites, the figure of merit and the related numbers are summarized in Table 4.2. Where the deuteron polarization of 51%, corresponding to the spin temperature $T_{SS} = 0.94$ mK is assumed and the polarizations of the other nuclei are calculated by Eq. (4.55). One can see that figure of merit of our ${}^6\text{LiD}$ is factor 1.8 larger than that of ammonia.

It should be noted that the dilution factor f considered above is to describe the choice of the material in the context of the figure of merit. For the extraction of the real physical asymmetry using Eq. (3.3), one needs to consider the Bjorken- x -dependence of the dilution factor f once it is measured. Such an approach is described in Ref. [111].

4.4.2 Preparation of ${}^6\text{LiD}$

In order to use ${}^6\text{LiD}$ for the COMPASS experiment, the particular challenge was the development of a mass production technique, which ensures the preparation of about 0.5 kg of highly polarizable granules of this material [119, 120]. The first step was the synthesis of the material from highly enriched ${}^6\text{Li}$ ($\approx 95.5\%$) and pure deuterium gas ($\approx 99.8\%$) by the reaction



which was performed in a specially designed furnace at temperatures between 700 K and 1100 K. After slowly cooling down and removing the material from the reaction chamber it was cut into small crystals with typical dimensions of a few millimeters.

In order to allow the DNP mechanism to operate, a suitable amount (10^{-4} - 10^{-3} per nucleus) of paramagnetic centers, i.e. of unpaired electrons, has to be implanted into the material. For this purpose the granules were exposed to the 20 MeV electron beam of the Bonn injection linac in batches

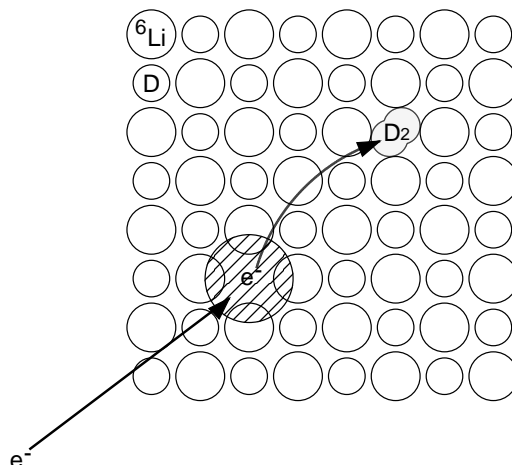


Fig. 4.13: A simple illustration of the F-center. A deuteron nucleus is hit and moved out from the original site by the electron beam. In the vacancy of the lattice, a free electron is captured.

of about 70 cm^3 , each for several hours. During the irradiation, in which each sample received a total dose of $2 \cdot 10^{17} \text{ e}^-/\text{cm}^2$, the material was kept at a temperature of $190 \pm 1 \text{ K}$ by means of a special irradiation cryostat [119]. The paramagnetic resonance of samples from each of the 13 batches were studied in a conventional X-band EPR spectrometer operating at 9.35 GHz. In order to prevent the paramagnetic centers from decaying, these studies as well as the storage of the material require the use of low (liquid nitrogen) temperatures. It was found that the radiation dose mentioned above gives rise to a concentration of paramagnetic centers of $2 \cdot 10^{19} / \text{g}$ and that the resonance structure of these defects is in agreement with the model of so called F-center. The simple view of F-center production is shown in Figure 4.13. By the electron beam bombardment, a deuteron nucleus is kicked out from the lattice and forms D_2 attaching to other deuteron nearby. In the vacancy in the original deuteron site, a free electron is captured. The wave function of the electron extends over the lattice sites of the six adjacent ${}^6\text{Li}$ nuclei, which leads to a characteristic 13 line pattern of the EPR signal as is shown in Figure 4.14. The discussion about the EPR spectrum and linking it to Hyperfine interaction is given in Section 4.1.6.

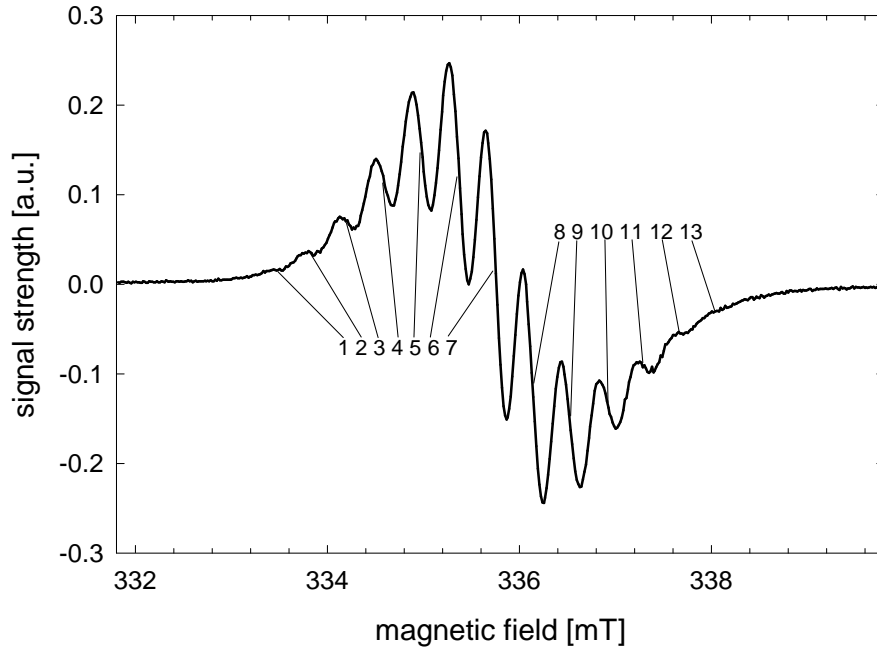


Fig. 4.14: Paramagnetic resonance spectrum of the electron irradiated ${}^6\text{LiD}$. The spectrum is taken at liquid nitrogen temperature 77 K. The 13 individual lines belong to the respective total magnetic quantum number of the six adjacent ${}^6\text{Li}$ nuclei.

4.5 Results from polarized target

4.5.1 TE calibration

The dynamic nuclear polarization value is determined by the area method based on TE calibration, according to Eq. (4.82). TE calibration is a very important and delicate process from which the most of the polarization errors come. In this section, how to process the TE signals and the consideration for the TE calibrations are reported.

First, consider how the NMR signals are processed. The NMR signals appear upon Q-curve of the NMR circuit as described in Section 4.2.2. If the magnetic field is shifted from the nominal value, the NMR signal does not appear on the Q-curve. The Q-curve is called *baseline* and shown in Figure 4.15 (a), which is the characteristic of the electronics circuit. When the nominal magnetic field is set, the NMR signal appears on the Q-curve as in Figure 4.15 (b) ('baseline + NMR signal'). By subtracting the base-

line (Figure 4.15 (a)) from 'baseline + NMR signal' (Figure 4.15 (b)), one can obtain the NMR signal on top of a residual background as shown in Figure 4.15 (c). The source of the residual background is considered to be a small change in the characteristics of electronics, for example a slight change in the impedance of the circuit or of the cable due to the temperature drift and so on. By subtracting the residual background by fitting a polynomial function to off-resonance region, the pure NMR signal is obtained as shown in Figure 4.15 (d). This pure signal corresponds to $C\chi''(\omega)$ where $\chi''(\omega)$ is the absorption function of the magnetic susceptibility of the material and C is a constant which includes, packing factor, sensitivity and amplification of the electronics and so on.

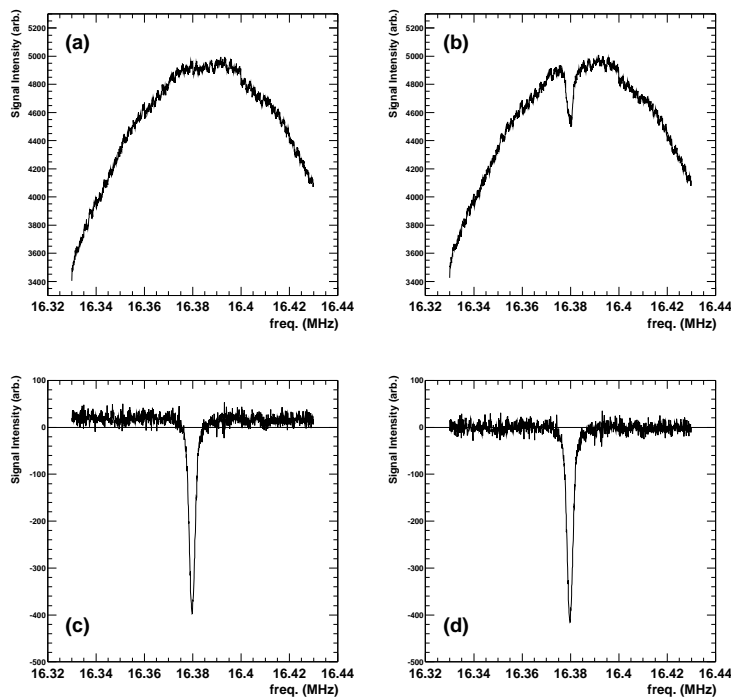


Fig. 4.15: Process of the NMR signal extraction. This data is from the deuteron TE measurement at 0.97 K. (a) 'Baseline', where no NMR signal appears because of slightly shifted magnetic field. (b) 'Baseline + NMR signal'. (c) Subtracted data '(b) - (a)'. Ideally, only NMR signal should appear but there is a residual background. (d) 'NMR signal' after the removal of residual background in (c) by polynomial fitting.

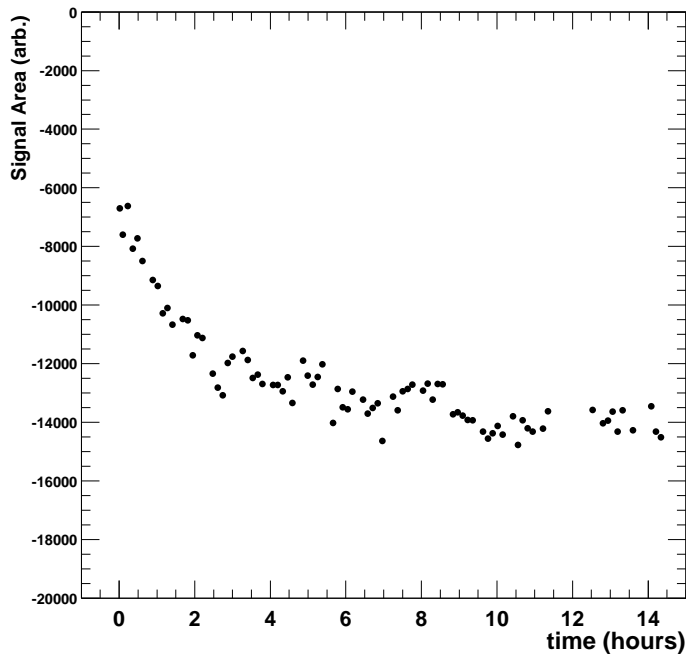


Fig. 4.16: Relaxation of the nuclear spin to the thermal equilibrium. This data is from the deuteron TE measurement at 0.97 K.

The area of the TE signal S_{TE} in Eq. (4.82) can be obtained by integrating the NMR signal shown in Figure 4.15 (d). Here one must be careful for that the spins are well in thermal equilibrium. Figure 4.16 shows the relaxation of the spins where the signal area is plotted versus time. The measurements show that it takes about 10 hours (8 hours) for spins in ${}^6\text{LiD}$ reaches the equilibrium with the lattice at temperature $T = 0.97\text{ K}$ (1.4 K). The area of the TE signal S_{TE} is determined by taking the average of the data points after the relaxation in Figure 4.16. The error of the TE signal δS_{TE} is evaluated by applying many patterns of fitting in removing the residual background discussed above.

In order to determine the calibration factor P_{TE}/S_{TE} by Eq. (4.82) it is necessary to know P_{TE} . P_{TE} can be calculated according to the Brillouin function Eq. (4.5) by knowing the temperature of the lattice. In COMPASS polarized target, the target cells are contained in the long Mixing Chamber

measurement ID	Nucleus	Temperature (K)	PT solenoid (T)	SM1
(1)	D	1.41	-2.506	OFF
(2)	D	1.41	+2.506	OFF
(3)	D	0.97	+2.506	OFF
(4)	D	0.97	-2.506	ON
(5)	D	0.94	+2.506	ON
(6)	${}^6\text{Li}$	1.41	-2.614	OFF
(7)	${}^6\text{Li}$	1.40	+2.614	OFF
(8)	${}^6\text{Li}$	0.95	+2.614	ON
(9)	${}^6\text{Li}$	0.94	+2.614	OFF
(10)	${}^7\text{Li}$	1.41	-0.990	OFF
(11)	${}^7\text{Li}$	1.41	+0.990	OFF
(12)	${}^7\text{Li}$	0.95	-0.990	ON
(13)	${}^7\text{Li}$	0.96	+0.990	OFF
(14)	${}^7\text{Li}$	0.94	-0.990	OFF

Tab. 4.3: Measurements for the TE calibration.

and 10 NMR coils are installed in order to measure the large target volume. On the other hand, temperature monitoring of 'section by section' is not practical. Thus it is ideal if Mixing Chamber temperature distribution is uniform. The uniform temperature was realized for TE calibration by filling Mixing Chamber with ${}^4\text{He}$, not with ${}^4\text{He}/{}^3\text{He}$ mixture. Below $T = 2.2\text{ K}$ in Figure 4.7, ${}^4\text{He}$ shows superfluidity that has an excellent thermal conductivity and assures the uniform temperature distribution. The temperature of Mixing Chamber was monitored by the vapor pressure method, which is the definition of the temperature today, ITS-90 [123]. The special volume in the dilution refrigerator, which is thermally in contact with Mixing Chamber, is filled with ${}^3\text{He}$ and its vapor pressure was measured by the model Baratoron from MKS instruments.

To make TE calibration reliable, the measurements were done in several conditions.

- At two temperatures, about 0.96 K and 1.4 K, in order to check and to include the variation in the calibration factor at different temperatures.
- At positive and negative solenoid field in order to check and include the variation if any.

Upstream cell		Downstream cell	
NMR coil	$\delta\left(\frac{P_{TE}}{S_{TE}}\right)$	NMR coil	$\delta\left(\frac{P_{TE}}{S_{TE}}\right)$
1	0.035	6	0.016
2	0.018	7	0.013
3	0.015	8	0.012
4	0.023	9	0.016
5	0.015	10	0.019

Tab. 4.4: Errors in TE calibration for deuteron signals. The NMR coils are numbered from upstream to downstream in an ascending order.

- With SM1 ON and with SM1 OFF. SM1 is Spectrometer Magnet No. 1 located downstream of the polarized target.

The TE measurements in the different conditions are listed in Table 4.3. The temperature effect and the sign of the solenoid current (field direction) effects were found much smaller than the the variation in the TE area evaluation. The SM1 effect was not visible in the NMR signal and was found negligible.

Summarizing, the errors in the TE calibration P_{TE}/S_{TE} includes the variation in the signal area evaluation, temperature drift and its measurement error, dependence of solenoid field sign, calibration value in the two different temperature, the negligible SM1 effects, and the amplifier effect (small TE signals are taken with the amplifier with nominal amplification factor of 227, while large enhanced signals were without amplifier). The errors of the calibration factor for each coils were shown in Table 4.4 for deuterons.

4.5.2 Deuteron polarization

In this section, the polarization of the deuteron and its related techniques are reported.

The enhanced deuteron polarizations were determined by the TE area method according to Eq. (4.82). At high polarization, the non-linearity of the electronics must be taken into account [124]. After the nonlinearity correction, the polarization can be given

$$P_D = \left(\frac{P_{TE}}{S_{TE}} \right) S_{dyn} \pm \frac{1}{2} C_{NL} \quad (4.98)$$

$$\delta P_D = \delta \left(\frac{P_{TE}}{S_{TE}} \right) S_{dyn} + \frac{1}{2} C_{NL} \quad , \quad (4.99)$$

where C_{NL} is the maximum possible nonlinearity effect which is estimated to be 0.5% for our case that modulation is less than 30% [124].

The DNP requires microwave irradiation thus the high cooling power by dilution refrigeration as well as low temperature is necessary. The refrigerator is operated in the $^3\text{He}/^4\text{He}$ dilution mode at temperatures between 100 mK and 300 mK depending on the actual microwave power. A typical build-up curve of the deuteron polarization is shown in Figure 4.17. Polarizations of +40% and -35% are usually reached within one day at comparatively high values of the microwave power, whereas a period of about one week is needed for obtaining the full polarization. During this second stage it is preferable to reduce the microwave power in order to optimize the working temperature of the refrigerator. The final deuteron polarizations (averaged over all NMR coils) were measured to be +54.2% and -47.1%. They were obtained under a 500 Hz modulation of the microwave frequency with a peak to peak amplitude of about 20 MHz. This technique is already known from the SMC experiment as being helpful in order to maximize the achievable polarization [111, 125, 126].

Figure 4.18 shows two dynamic NMR signals of coil No. 8 with polarizations of about +45% and -45%. In contrast to the TE signals, the dynamic signals exhibit a slight but easily detectable asymmetry around their respective centers, which themselves are shifted towards lower ($P < 0$) or towards higher ($P > 0$) frequencies. The magnitude of both, the asymmetry and the frequency shift, depends on the sign as well as on the degree of the polarization. Qualitatively this effect can be explained by different local fields at the sites of the deuterons, which are produced by the polarization of the neighboring ^6Li nuclei [127, 128].

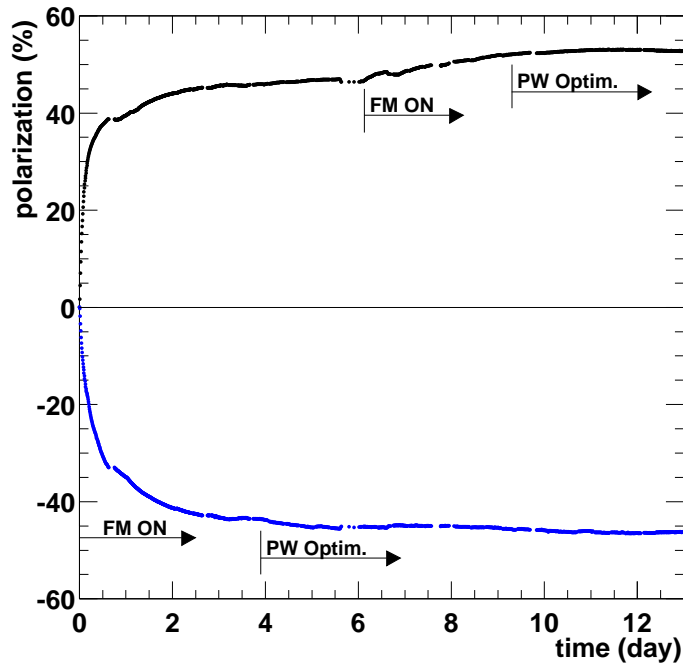


Fig. 4.17: Example of the deuteron polarization build-up. The upstream (downstream) cell is polarized positively (negatively). The interruptions of the data points correspond to a magnetic field rotation or to a technical interruption of the NMR data taking. The start time of the microwave frequency modulation is indicated by 'FM-ON' and that of the microwave power optimization by 'PW Optim.'

During the polarization build-up a shift of the optimum microwave frequencies towards the center of the electron Larmor resonance was observed. In the case of unmodulated microwaves the optimum values started from about 70.210 GHz and 70.270 GHz for positive and negative polarizations, respectively. The final frequencies were set around 70.238 GHz and 70.245 GHz for about $|P| > 40\%$. This behavior is qualitatively in agreement with the predictions following from the low temperature treatment of the spin temperature theory for hyperfine broadened electron spin systems [129]. In the case of enabled frequency modulation the polarization dependent shift was observed to be slightly less pronounced than without modulation. Nearly at the maximum polarization, the optimum central frequency was 70.210 GHz

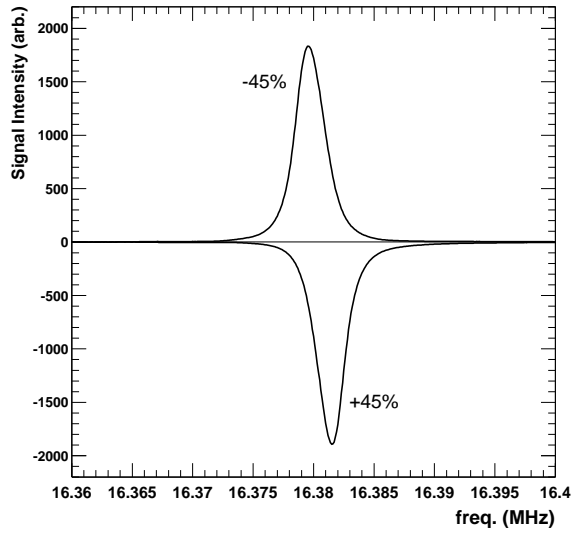


Fig. 4.18: Enhanced deuteron NMR signals at +45 % and -45 %. The positive polarization signal appears downward due to the amplification characteristics of DC-Offset card. For visibility, the central 40 kHz part is shown here while data is taken over 100 kHz.

and 70.255 GHz for positive and negative DNP respectively.

Compared to the target materials used in the SMC experiment [111], the polarization build-up of lithium deuteride is considerably slower. This observation is attributed to the relatively long relaxation time T_1 of the paramagnetic F-center. Thanks to the technique of spin reversal by field rotation (see Section 4.3.2) the long build-up time of ${}^6\text{LiD}$ is not a serious drawback regarding the accuracy of the COMPASS experiment, which relies on frequent changes of the relative orientation of the polarizations in the two target cells with respect to the muon beam. Most of the interruptions of the data points in Figure 4.17 correspond to these field rotation cycles, which are performed in the frozen spin mode. Compared to butanol and ammonia the much larger nuclear relaxation time of lithium deuteride at low magnetic fields – being about 2000 h at 0.5 T and at 90 mK – prevents the material from any polarization loss during the procedure of polarization reversal.

The individual polarizations measured by each of the ten NMR coils are shown in Table 4.5. They are differing by amounts larger than the measurement errors. Thus we consider that they reflect the physical polarizations

Upstream cell		Downstream cell	
NMR coil	$P_D \pm \Delta P_D$	NMR coil	$P_D \pm \Delta P_D$
1	$+57.8 \pm 2.2$	6	-46.2 ± 0.9
2	$+52.1 \pm 0.5$	7	-48.3 ± 0.8
3	$+53.0 \pm 0.9$	8	-49.6 ± 0.7
4	$+51.3 \pm 1.3$	9	-45.5 ± 0.8
5	$+56.7 \pm 1.0$	10	-45.9 ± 1.0

Tab. 4.5: Maximum deuteron polarization. The NMR coils are numbered from upstream to downstream in an ascending order. The major part of the error are from the TE calibration. The variation of the measured polarization among the coils is discussed in the text. The average polarization is $+54.2\%$ in the upstream cell and -47.1% in the downstream cell.

as present at the different positions within the target cells. One explanation for these differences considered so far could be ruled out by a comparison with the preliminary polarization results from the present run of 2002, which show similar differences between the NMR coils. After removing and refilling the target cells a possible correlation between a certain NMR coil and a certain production lot, which may have been prepared under slightly different conditions, is now to be excluded. The only explanations left are basing on certain temperature differences or on differently well matching properties of the microwave field along the two target cells. A $\pm 3 \cdot 10^{-5}$ inhomogeneity of the solenoid magnetic field leads to variation of the optimum frequency by 4 MHz. A frequency detuning of that size may be already critical in achieving the highest possible polarization in this material. Also the power distribution within the microwave cavity may vary along the cavity axis due to the presence of differently absorbing or reflecting materials within Mixing Chamber (e.g. the microwave stopper separating the two target cells).

It should be mentioned that a difference up to 7% between the average positive and negative polarizations has been observed, the sign of which is consistent with other results on ${}^6\text{LiD}$ samples of equal performance [117]. From the fact that a similar result has also been observed using the Bochum test cryostat – a dilution refrigerator with a completely different geometry of Mixing Chamber – it is believed that this effect is due to an inherent property of the material as prepared in the way described above.

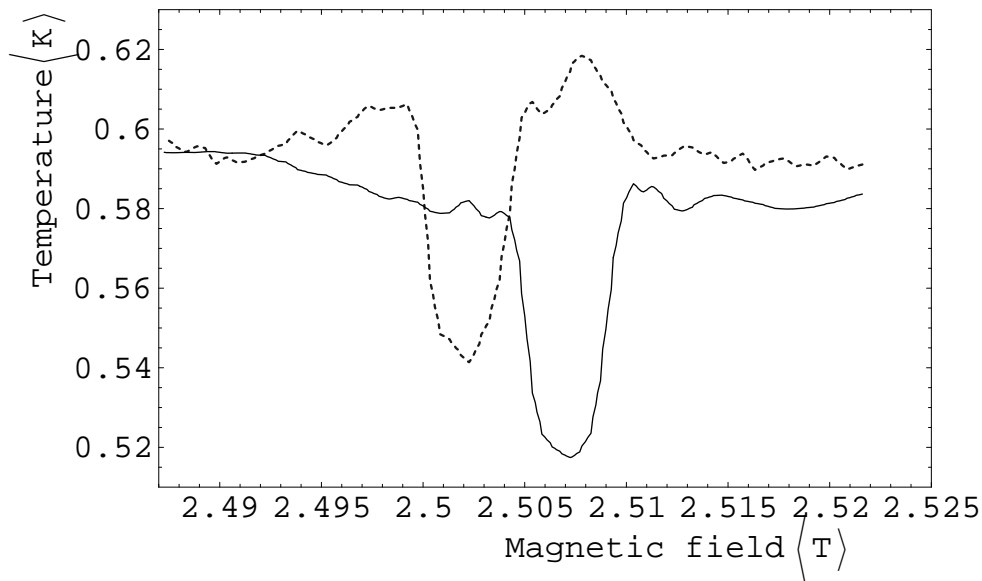


Fig. 4.19: Paramagnetic resonance spectrum of ${}^6\text{LID}$ at high polarization by bolometric method with the PT apparatus. The microwave frequency is 70.211 GHz. The solid (dashed) line is the measured resonance line of upstream (downstream) cell at $P_{\text{D}} = 52\%$ (46%). The temperature of the carbon thermometer is used as a bolometric prove.

4.5.3 Paramagnetic resonance at high polarization

The paramagnetic resonance at high polarization is of interest for the understanding of DNP process, while it is not widely carried out because of complexity and practical difficulty. We obtained the resonance lines at $P_{\text{D}} = 52\%$ and at $P_{\text{D}} = -46\%$ as shown in Figure 4.19.

The paramagnetic resonance lines were obtained in the polarized target apparatus by using the carbon thermometers as bolometers, keeping the microwave frequency and power constant, and sweeping the magnetic field. One carbon thermometer was installed outside each target cell and its temperature reflects the microwave absorption principally by the paramagnetic center in the material. Microwaves with a common frequency was fed to both upstream and downstream cavity, by using only a single microwave generator and dividing its output into two. The high polarizations were obtained by DNP in prior to this paramagnetic resonance measurement and was kept by the frozen spin mode.

In Figure 4.19, one can see the satellites and the baseline structure as well as the main broad peak. Since this bolometric method is not as ideal as the conventional dedicated EPR apparatus (for example, the one used to take the spectrum in Figure 4.14), the fine structures are not visible. In addition, the satellites and the baseline structure should not be attributed to the resonance of the material because they change when one applies a different microwave frequency. Hence, only the frequency of the main broad peak is relevant to the material. The measured lines show the separation of the main broad peaks by $4.5 \cdot 10^{-3}$ T.

In principle, the separation of these spectrum can be directly compared with the one in Fig 4.14 because the strength of hyperfine interaction is independent of the external magnetic field. (Please note that Figure 4.14 is the differential $\partial/\partial B$ spectrum while Figure 4.19 is not but the direct spectrum.) The comparison shows that the 6 ^6Li nuclei around the paramagnetic center, which produce the total magnetic quantum number +13 (-13), are polarized nearly 100 %. This observation is consistent with the DNP mechanism mentioned in Section 4.1 that the nucleus close to the paramagnetic center is efficiently polarized.

The direction of the shifts in Figure 4.19 is consistent with that of the optimum microwave frequency shift mentioned in Section 4.5.2. Therefore the shift of paramagnetic resonance due to the polarization of the neighbor nuclei is considered to be responsible for the shift of the optimum microwave frequency.

4.5.4 Verification of equal spin temperature theory

Not only the polarization of the deuteron, but also that of ^6Li and that of the residual ^7Li nuclei ($\approx 4.5\%$) are of importance for the evaluation of the particle physics data as well as for the understanding of the DNP process. These polarizations are plotted versus the deuteron polarization in Figure 4.20 together with the prediction by the EST concept [129]. The basic statement of the EST concept is that the Zeeman system of every nuclear species with spin I in the material share the same spin temperature T_S . In other words the difference of the Zeeman occupation numbers and thus the polarization of the particular spin system can be calculated from the respective Brillouin function Eq. (4.5) with T replaced by T_S .

The NMR measurements of ^6Li and ^7Li were done by stopping the microwave pumping occasionally during the DNP process and by setting the solenoid field so that the Larmor frequency of ^6Li or ^7Li became equal to the NMR circuit resonance frequency, i.e. to 16.38 MHz. The correction coils,

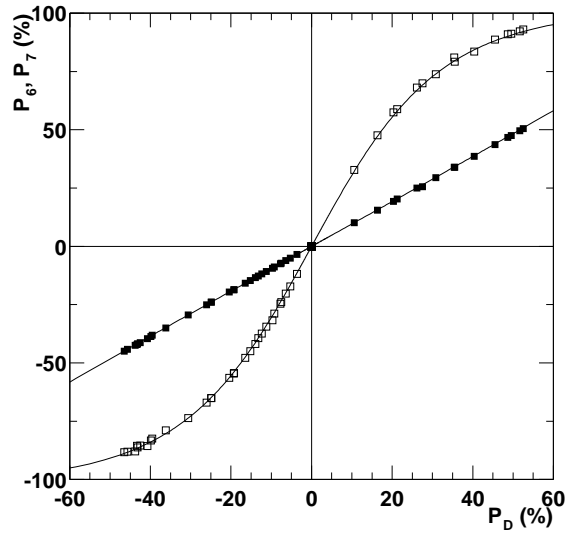


Fig. 4.20: The polarizations of ${}^6\text{Li}$ and ${}^7\text{Li}$ versus that of the deuteron. The closed (open) squares are the measured polarization of ${}^6\text{Li}$ (${}^7\text{Li}$). The lines are the prediction by EST concept. The measurements is consistent with the EST concept.

which are used to achieve the highest possible homogeneity of the magnetic field, were adjusted according to the respective solenoid field. Before and after each measurement of the polarization of the two lithium isotopes the deuteron NMR signals were taken at the nominal field to verify that no polarization was lost. Just like in the case of the deuteron the polarizations of ${}^6\text{Li}$ and ${}^7\text{Li}$ were determined by the area method with the TE signals taken at 0.97 K and at 1.44 K. It should be noted that the hardware tuning of the NMR system was kept unchanged throughout the experiment. Our data are in good agreement with the EST concept indicating a common spin temperature below 1 mK at the highest polarizations.

Besides important information about the DNP process the observed agreement offers significant practical benefits. Most importantly, it is not necessary to measure the polarizations of all the different spin species separately, which would either require more NMR coils in the material or a frequent change of the magnetic field in order to use the existing coils for the polarization measurement of the other nuclei. Both solutions would imply negative consequences for the efficiency of the particle physics experi-

ment. With the validity of the EST concept it is sufficient to monitor one of the nuclear polarizations, whereby all of the NMR coils can be used to check the uniformity of the polarization section by section. The corresponding polarization values of the other nuclei may then be calculated most simply using Eq. (4.55), which makes the extraction of the gluon polarization $\Delta g/g$ simpler and more reliable.

5. SUPERCONDUCTING MAGNET FOR THE POLARIZED TARGET

The hardware which the author was particularly responsible for in the COMPASS collaboration, which he spent major fraction of his time on, and which he enjoyed and learned very much is the large superconducting magnet system in the phase of installation and the first operation. The superconducting magnet system itself is a complicated apparatus in the sense that electric, magnetic, cryogenic and mechanical aspects are correlated each other. In addition, this size of magnet stores large energy and the required performance in the COMPASS experiment is very high. Therefore, the installation and the operation must be done in a professional industrial manner. Taking into these facts, the author prepares one chapter for the large superconducting magnet for the polarized target.

Originally, it was planned that one manufacture produces a new superconducting magnet, which is optimized for COMPASS experiment [75]. However, the new magnet has not been completed so far. As the second best choice, the COMPASS collaboration decided to use the existing superconducting magnet which was produced by Saclay, C.E.A. France and was used for the polarized target in NA47 SMC experiment at CERN. (In this chapter, the term *Magnet*, starting with capital M, means the entire system related to this superconducting magnet.) Since Magnet was not foreseen to be used again, it had not been stored in an ideal manner. I worked for the installation of this Magnet, together with the experts from Saclay and those from EP/TA3 division at CERN. The work contained wide spectrum of aspects, cryogenic, electric, magnetic, mechanic, related safety, and so on. In practice, what I did contains understanding the schemes, inventory to identify existing and missing items, re-building the system with modifications, test of each sub-functions, commissioning and the operation of the entire Magnet system in the COMPASS Polarized Target.

In this chapter, only operation related technical aspects are described, while many other technical points were considered in the phase of preparation. The basics and the practice of the engineering of the superconducting magnet can be found in for example in Ref. [130]. Other technical informa-

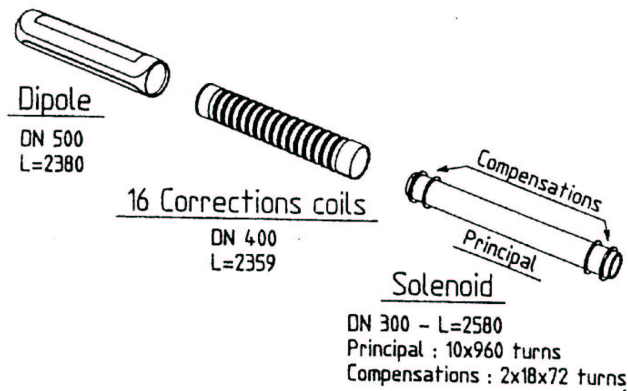


Fig. 5.1: The illustration of the coils before assembly. There are three formers and they are assembled in concentric manner.

tion can be found in [131, 132]. The abbreviation and the French terms in this chapter is explained in Appendix.

5.1 Electromagnetics

The Magnet system produces a longitudinal (horizontal) 2.5 T solenoid field and a transverse (vertical) 0.5 T dipole field. The assembly of the coils are shown in Figure 5.1. The coils are in the liquid helium bath and the superconductivity is realized.

The solenoid field with a homogeneity of $\pm 3 \times 10^{-5}$ is produced by the following items.

- 'one principal solenoid + two compensation coils'. These are connected electrically in series. The compensation coils compensates the edge effect of the principal solenoid coil. In this chapter, the subsystem related to this circuit is called *Solenoid*. The power supply for Solenoid is bipolar.
- 16 independent correction coils. These are used to achieve the homogeneity. The subsystem related to this circuit is called *Corrections*. The 16 power supplies for Corrections are unipolar but there are the relay-based electronics which inverse the polarity, enabling the practical bipolar operation.

	principal solenoid coil	compensation coils
Nominal B (T)	2.506	
$\Delta B/B$	$\pm 3 \times 10^{-5}$ (with Corrections)	
Nominal I (A)	417.32	
Nominal dI/dt (A/s)	0.5 when $I > 80$ A 1.0 when $I < 80$ A	
Nominal stored energy (kJ)	488	
Max. B (T)	2.63	
Max. I (A)	438	
Max. stored energy (kJ)	537	
Inductance (H)	5.6	
Dumping resistor (Ω)	1	
Inner diameter (mm)	300	300
Outer diameter (mm)	326	347
Axial length (mm)	2000	150 each
Number of layers	10	18 each
Number of turns	9610	1296 each

Tab. 5.1: Electromagnetic characteristics of Solenoid. The field homogeneity $\Delta B/B$ is achieved with the help of Corrections. The max. I is limited by the hardware setting of the power supply. The nominal I is defined conservatively in order to avoid the risk of quench due to the heating by AC-loss. (see for example, [130].)

The dipole field with a moderate homogeneity is produced by

- A pair of the saddle coils. the subsystem related to these coils is called *Dipole*. The power supply for Dipole is unipolar.

The electric scheme of Solenoid together with Corrections is shown in Figure 5.2. The circuit in the left part shows Solenoid. Three coils corresponds to the first compensation coil, the principal solenoid coil, and the second compensation coil, and they are connected in series. RD 350 is the dumping resistor of 1Ω installed inside the helium vessel which plays an important role together with the main circuit breaker CP 350. in Décharge Rapide (fast discharge) in the protection of Magnet (Section 5.3). The circuit RM 350, DM 350 and two resistors near them are installed to check if there is grounding error (leak current to the electric ground) in Solenoid. DT 351 is the quench detection electronics which surveys if there is a voltage drop due to a quench in the coils. VS 350P and VS 350N are the electronics

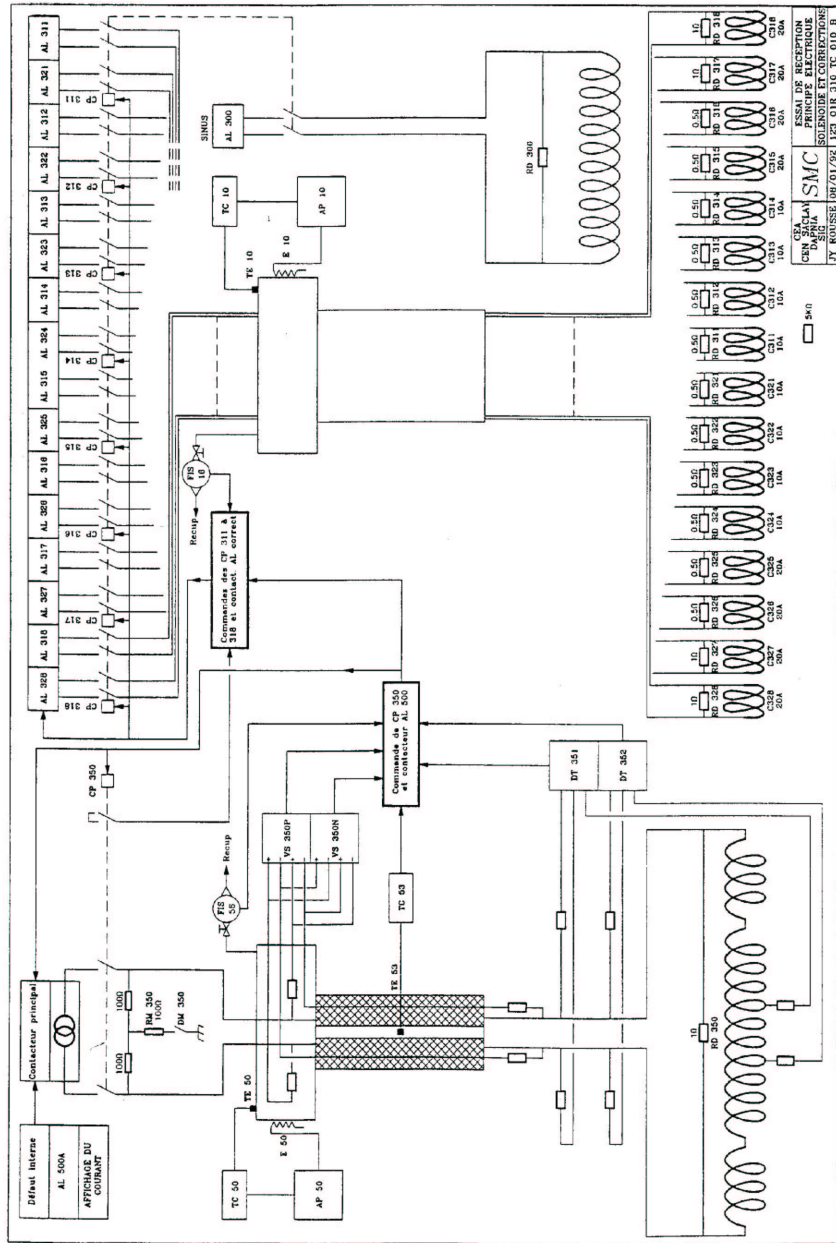
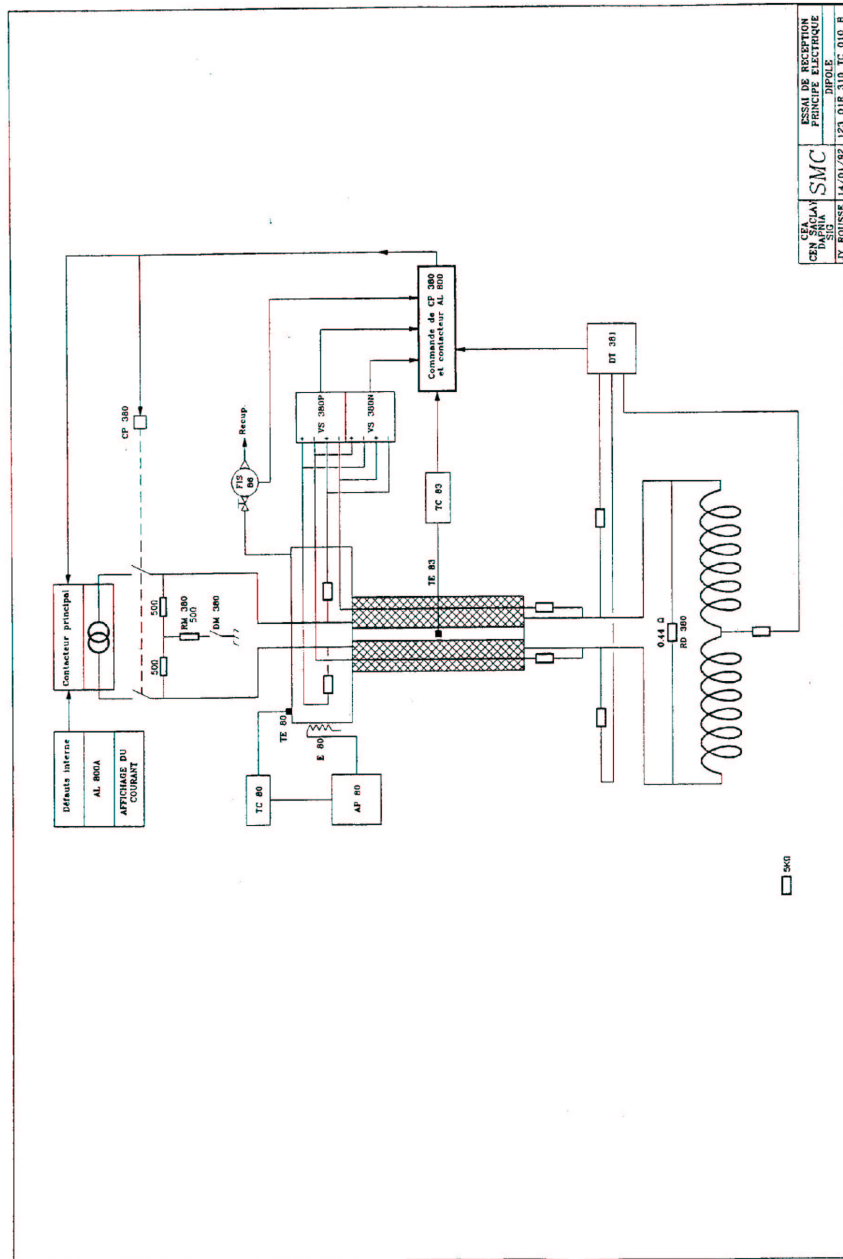


Fig. 5.2: Electric scheme of Solenoid and Corrections. (The circuits related to AL 300 is only for the test purpose and not used in the experiment.)



LES	SMC	SEMI DE SUPERCONDUCTEUR
CEN SAULAY		PRINCIPES ELECTRIQUE
DIPOLE		DIPOLE
JY ROUSSE 14/01/82		123 01E 310 TC 010 B

Fig. 5.3: Electric scheme of Dipole.

ID	C311-C316	C317	C318
	C321-C326	C327	C328
Nominal B (T)	< 0.013	< 0.030	< 0.045
Nominal I (A)	< 5	< 6	< 6
Nominal dI/dt (A/s)	–	–	–
Nominal stored energy (J)	< 0.75	< 4.32	< 9.72
Max. B (T)	~ 0.025	~ 0.050	~ 0.15
Max. I (A)	10	10	20
Max. stored energy (J)	3.0	12	108
Inductance (H)	0.06	0.24	0.54
Mutual Inductance (H) with Solenoid	0.14	0.27	0.41
Dumping resistor (Ω)	0.5	1	1
Diameter (mm)	408	408	408
Axial length (mm)	150	150	150
Number of layers	2	4	6
Number of turns	300 each	600 each	each 900 each

Tab. 5.2: Electromagnetic characteristics of Corrections. The ID refers the indication in Figure 5.2. The Max. I is limited by the capability of the power supplies. There is no active setting for the nominal ramping rate dI/dt . The nominal current is directly set by the power supplies and it takes practically about 5 seconds to stabilize.

which surveys if there is a voltage drop due to overheating in the current leads inside the magnet structure. VS 350P is responsible for the positive current operation and VS 350N for the negative since the power supply for Solenoid is bipolar. TE53 is the temperature sensor which monitors the temperature of the current leads if there is overheating. The chain with the number 50 is used in order to keep the connection box of the current leads warm by detecting the temperature by TE 50, deciding ON-OFF of the heater by the electronics TC 50, and warming up the connection box by the heater E 50 whose electric power is supplied by AP50. FIS 56 is the flow meter monitoring the gas ^4He flow along the current leads.

The small 16 coils in Figure 5.2 depict the correction coils. One dumping resistor is installed for each coil. CP 311-CP 318 are the main circuit breakers, each of which covers two coils times two lines, i.e 4 lines. The chain with the number 10 is for keeping the connection box of the current leads warm, just like in Solenoid.

Nominal B (T)	0.5 (0.42)
$\Delta B/B$	$< 2 \times 10^{-2}$
Nominal I (A)	650 (550)
Nominal dI/dt (A/s)	2.5
Nominal stored energy (kJ)	78 (56)
Inductance (H)	0.37
Dumping resistor (Ω)	0.44
Max. B (T)	0.5
Max. I (A)	650
Max. stored energy (kJ)	85
Inner diameter (mm)	500
Outer diameter (mm)	508
Axial length (mm)	2500
Number of turns	272 per coil.

Tab. 5.3: Electromagnetic characteristics of Dipole. The nominal magnetic field B of 0.42 T is recommended in the long term operation of Dipole for the physics program with transversely polarized target from the magnet protection point of view. The max. I is limited by the capability of the power supply. The nominal dI/dt is defined conservatively in order to avoid the risk of quench due to the heating by AC-loss.

The electric schemes of Dipole is shown in Figure 5.3. The design strategy is basically same as that for Solenoid, except that the practical parameters like the value of the dumping resistor are different.

Electromagnetic characteristics of Solenoid, Corrections, and Dipole are summarized in Table 5.1, Table 5.2 and Table 5.3, respectively.

5.2 Cryogenics

The cryogenic scheme is illustrated in Figure 5.4. The central item corresponds to the structure of Magnet which contains three independent volumes inside.

- Isolation Vacuum ($V \sim 100 \ell$), which is shared with the dilution refrigerator and is pumped out by the diffusion pump C42 and the mechanical rotary pump C40. Inside the isolation vacuum, there is one radiation screen between the outside structure and Helium Vessel. The radiation screen is covered by layers of the superinsulation sheets.
- Helium Vessel. ($V \sim 500 \ell$) The coils are located inside the it.
- LN2 Precooling Line. In the precooling from 300 K to 100 K, LN2 is sent into this line.

The left side dewar in the Figure 5.4 is LN2 dewar which is used for the precooling of the magnet.

The right side dewar is the 2000 liters LHe buffer dewar. Throughout the experiment, the LHe level in the buffer dewar is kept about 50 % and the pressure is maintained at 1.34-1.36 bar with respect to vacuum. LHe is supplied to the buffer dewar from the liquefier so-called COLD BOX with the maximum capability of 110 LHe ℓ /hour. The LHe buffer dewar and COLD BOX is controlled by CERN LHC/ECR division.

The evaporated helium gas from Magnet is sent to COLD BOX via He gas recovery line, labeled LIGNE RECUPERATION “ONLINE” in Figure 5.4, via which the evaporation gas from the dilution refrigerator is also sent. (In this Figure, the evaporation gas from the dilution refrigerator is not illustrated. See Figure 4.6.) The pressure of He gas recovery line is maintained at 50-60 mbar above ambient atmospheric pressure by CERN LHC/ECR division.

For the mechanical safety of Helium Vessel, there two mechanical pressure relief valves PSV 65 and PSV 65, which opens at the pressure difference of 0.5 bar and 1.25 bar with respect to the ambient atmospheric pressure and closes after the pressure is relieved. In addition to them, there is one rupture disk PSE 67 which breaks at the pressure difference of 2 bar w.r.t. ambient atmospheric pressure.

The cryogenic characteristics during normal continuous operation and the cooling down phase is described in the following sections.

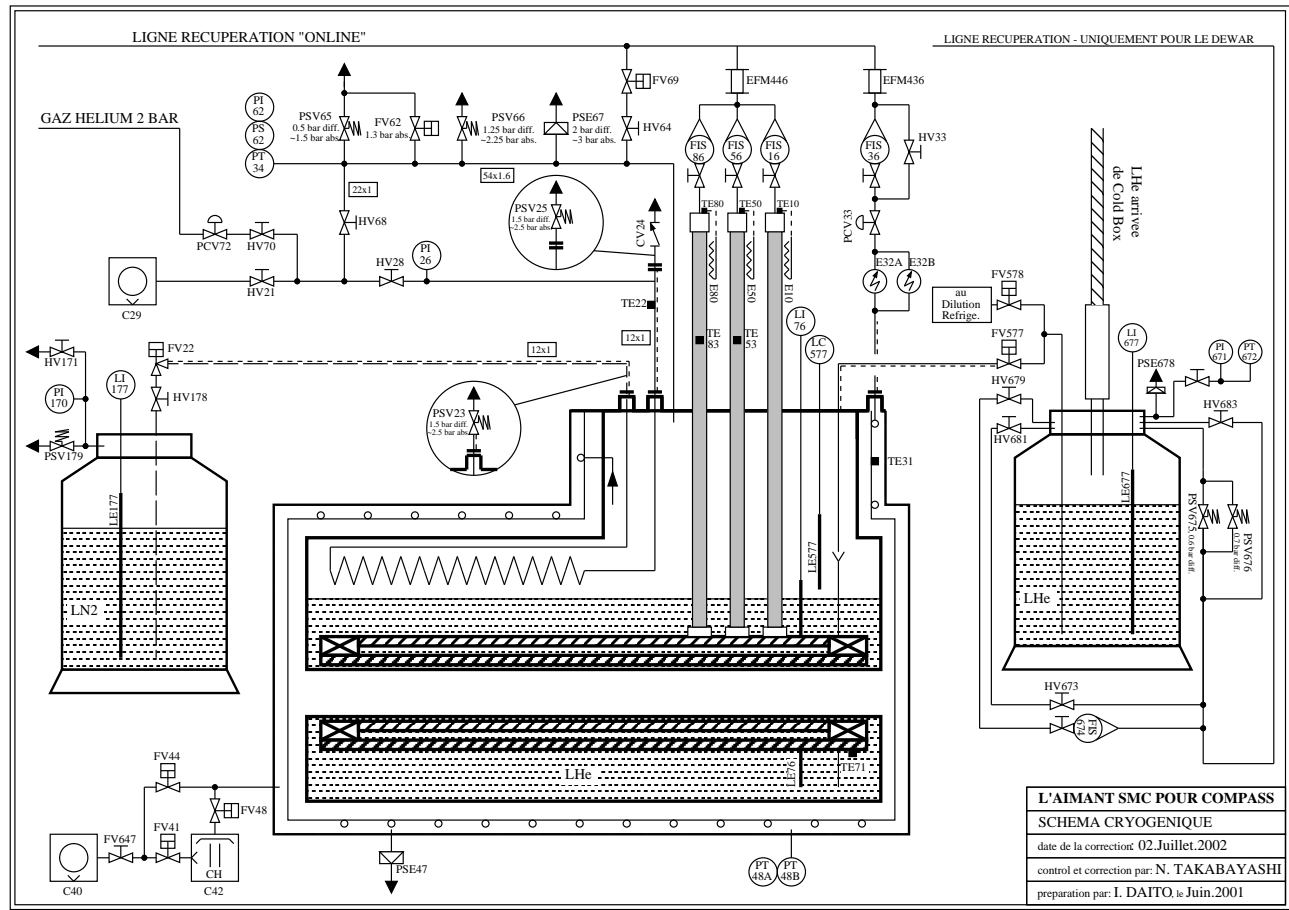


Fig. 5.4: Cryogenic scheme of Magnet.

5.2.1 Normal continuous operation

The superconductivity of the coils is realized by keeping the coils in liquid helium, which is filled inside the LHe vessel. The operation pressure of Helium Vessel is 1.1-1.15 bar w.r.t. vacuum under which the liquid helium is naturally boiling off at temperature of 4.3-4.4 K.

LHe is supplied from the LHe buffer dewar to Helium Vessel, driven by the pressure difference between them. The evaporation He gas from Helium Vessel, which is still cold, is distributed into 4 paths and cools down the related parts.

(Path 1): along Solenoid current leads in the Magnet structure.

(30-32 gas He ℓ /min.)

(Path 2): along Dipole current leads in the Magnet structure.

(30-32 gas He ℓ /min.)

(Path 3): along Corrections current leads in the Magnet structure.

(18-20 gas He ℓ /min.)

(Path 4): through the piping fixed to the radiation screen.

(70-100 gas He ℓ /min.)

The flow rates are determined by the pressure difference between Helium Vessel and He gas recovery line and by the impedance balance between the 4 paths, practically by adjustable valves FIS 56, FIS 86, FIS 16 and FIS 36.

The LHe level inside Helium Vessel is maintained automatically by the loop of LHe level sensor LE577, Level controller LC 577 which decides 'Supply/Minimum' in a threshold manner, the electro-pneumatically controlled valve FV 577 which opens completely at 'Supply' signal from LC 577 and keeps small flow at 'Minimum' signal. The small flow is kept by 'Minimum' mode to avoid the warming up of the transfer tube, which would cause inefficient transfer in the next 'Supply' mode. More He gas comes out from Helium Vessel and the pressure there increases in 'Supply' mode than in 'Minimum', because there is no perfect transfer tube and LHe evaporates in filling the Helium Vessel. Therefore, during 'Supply' mode, the Path (a)

Path (a): from Helium Vessel to He gas recovery line via HV 64 and FV 69

is automatically opened in order to release the extra pressure in addition to the (Path 1)-(Path 4) above. LC 577 is tuned so that 'Supply' mode takes place every a few minutes and 'Supply' mode completes in about 10 seconds.

Overall, the typical LHe consumption is 20 LHe ℓ /hour.

5.2.2 Cooling down phase

The cooling down phase is splitted further into 2 stages.

(Stage 1) From 300 K to 100 K with LN2.

(Stage 2) From 100 K to 4 K and filling with LHe.

Cooling down from 300 K to 100 K with LN2

This stage contains crucial risks to damage the magnet system and there exist special attentions.

Spatial temperature gradients must be avoided. Rapid cooling itself also produces spatial temperature gradients and must be avoided. The superconducting conductor consists of the superconducting filaments, high thermal conductivity metal stabilizer (copper in this Magnet), and the insulator on its surface. The conductor is wound on the metals formers and is impregnated with epoxy-resin. Each material has different thermal contraction coefficient and different thermal conductivities. The rapid cooling and the spatial temperature gradients would causes the forces at the interfaces of the material, which an potentially damage the coils system.

Solidification of any substance, especially solid H_2 , must be avoided. Solid on the coil surface decreases cooling efficiency, resulting in the degradation in the stabilizing performance. Solid H_2 is more problematic since it is formed at 273 K and is cooled down to 100 K, showing a different thermal contraction coefficient on its way. In addition, it can potentially harm the electric insulation and produce defect current to the electric ground.

Taking these points into account, the following cooling method is employed.

- Fill Helium Vessel with He gas as heat exchange gas.
- Send LN2 through the LN2 Precooling Line.

The heat exchange gas mediates the 'coldness' from LN2 Precooling Line to the coils, softly reasonably uniformly in space. In order to avoid the rapid cooling, the nominal cooling down speed is conservatively given as 2 K/hour. The LN2 feeding is semi-automatic ON-OFF control in the loop of TE 22 and FV 22. The temperature sensor TE 22 monitors the temperature of outgoing N_2 gas and a electronics TC 22 decides the ON-OFF control according to the setting point. The valve FV 22 opens at 'ON' signal and closes at 'OFF' signal. The setting point of TC 22 is given by the operators based on the

experience data. By changing the temperature setting in TC 22 by 5-10 K every several hours, the cooling rate of 2 K/h can be achieved. A small overshooting in the cooling rate, say 4 K/h for a few hours is not preferable but was acceptable.

In order to avoid the solidification of any substances, practically from the ambient air, the pressure of heat exchange He gas in Helium Vessel is kept between 1.05-1.2 bar w.r.t. vacuum by filling He gas adequately.

The nominal estimation is that this stage requires 1500 LN₂ ℓ and can be done in 4 days. Practically, it is done in about 5 days by the conservative operation.

Cooling down from 100 K to 4 K and filling up with LHe

In this stage, the risks is less that in the previous stage, because the thermal contraction of the materials finishes at 120-140 K. On the other hand, solidification of any substance should be still avoided. The following method is used in this stage.

- send LHe from LHe buffer dewar into Helium Vessel.

Since there is no risk of thermal contraction, this stage can be proceeded as fast as practical. The cooling speed is practically limited by the acceptable amount of outgoing cold He gas. In this stage, the paths of the outgoing gas is Path (1)-(4), Path (a) in Section 5.2.1 plus bypass line through HV 33 in the Screen flow line. The current lead connection boxes along Path (1)-(3) are equipped with the heaters E 50, E 80 and E 10, respectively so that no solid H₂O should be formed there. Each heater can accept about 45 gas ℓ/min. The flow to other paths are limited so that the cold outgoing gas should not freeze the line too much. The pressure in He vessel is kept above ambient atmospheric pressure due to the large evaporation of He.

When cooling down to 4 K, LHe from LHe buffer dewar is guided to the bottom of the Helium Vessel for the efficient cooling of the coils. When filling starts, LHe is guided to only to the top part of Helium Vessel for the better separation of gas phase. This configuration is used in the normal continuous operation as well in order to avoid a quench due to the bubble originating from LHe transfer.

Typically it takes 1 day to cool the coils down to 4 K and takes another 1 day to fill up Helium Vessel with LHe.

5.3 Active protection system

Since this size of superconducting magnet stores a large energy which can potentially damage the coils themselves, the vessel structures, the internal cabling and so on, one must protect the magnet system actively.

The active protection system is based on the 'two-level' policy.

- Décharge Lente (DL, Slow Discharge). When the surveillance instruments find a signature of danger which does not require immediate actions, the chassis CCS1 or CCS2 commands the DL to the instruments involved.
- Décharge Rapide (DR, Fast Discharge). When the surveillance instruments find any crucial danger which requires a sudden actions, the chassis CCS1 or CCS2 commands DR to the instruments involved.

For three coil systems (Solenoid, Corrections, and Dipole), the details of DL is summarized in Table 5.4 and those of DR in Table 5.5 and 5.6.

ID	DL in Solenoid
possible causes	<ul style="list-style-type: none"> • He flow along the current leads too low (FIS 56 < 20 gas ℓ/min). Risk of overheating of the current leads inside He vessel. • Bad Vacuum (PT 48B > $1.0 \cdot 10^{-5}$ mbar). Risk of violent evaporation of 500 liters of LHe and risk of quench. • LHe level too low (LC 77 < 5 %). Risk of quench.
action by CCS 1	<ul style="list-style-type: none"> • RAZ Solenoid PSU. (Solenoid PSU actively decreases the current down to 0 A in a controlled manner at the specified slope of 0.5 A/s.)
consequence	<ul style="list-style-type: none"> • The stored energy of 488 kJ will be dissipated in the transistor bank of Solenoid PSU.
ID	DL in Corrections
comment	<ul style="list-style-type: none"> • There is no DL in Corrections since the current and the stored energy are small.
ID	DL in Dipole
possible causes	<ul style="list-style-type: none"> • He flow along the current leads too low (FIS 86 < 20 gas ℓ/min). Risk of overheating of the current leads inside He vessel. • Bad Vacuum (PT 48B > $1.0 \cdot 10^{-5}$ mbar). Risk of violent evaporation of 500 liters of LHe and risk of quench. • LHe level too low (LC 77 < 5 %). Risk of quench.
action by CCS 2	<ul style="list-style-type: none"> • RAZ Dipole PSU. (Dipole PSU actively decreases the current down to 0 A in a controlled manner at the specified slope of 2.5 A/s.)
consequence	<ul style="list-style-type: none"> • The stored energy of 78 kJ will be dissipated in the transistor bank of Dipole PSU.

Tab. 5.4: DL (Slow discharge). RAZ stands for Remise à Zero (Put back to zero) and PSU for Power Supply Unit. Identification (ID) label is used to describe each case.

ID	DR in Solenoid
possible causes	<ul style="list-style-type: none"> • Detection of quench ($DT\ 351 > 20\ \text{mV}$ OR $DT\ 352 > 20\ \text{mV}$). Risk of the local overheating at the quench spot. • Voltage drop in the current leads too high ($VS\ 351 > 75\ \text{mV}$ OR $VS\ 352 > 75\ \text{mV}$). Risk of overheating in the current leads. • Temperature at the current leads too high ($TC\ 53 > -10\ ^\circ\text{C}$). Risk of overheating in the current leads.
actions by CCS1	<ul style="list-style-type: none"> • Shutdown Solenoid PSU. • Open the circuit breaker CP 350. • Open the active valve FV 62 in order to release the rapidly evaporated He gas.
consequences	<ul style="list-style-type: none"> • The stored energy of 488 kJ will be dissipated mainly in the dumping resistor RD 350 ($1\ \Omega$). Its time constant is $5.6\ \text{H}/1\ \Omega = 5.6\ \text{sec}$. • In the case of quench, some fraction of the energy will be dissipated at the quenching spot by ohmic heating.
comments	<ul style="list-style-type: none"> • The detection signal of DR in Solenoid is used to close FV 577 (valve for LHe transfer) in order to avoid sending high pressure into the LHe buffer dewar.
ID	DR in Corrections
possible causes	<ul style="list-style-type: none"> • He flow along the current leads too low ($FIS\ 16 < 10\ \text{gas}\ \ell/\text{min}$). Risk of overheating in the current leads inside He vessel. • DR in Solenoid. DR in Solenoid is a serious case and Corrections should be shutdown to avoid further complications.
actions by CCS1	<ul style="list-style-type: none"> • Shutdown Correction PSUs. • Open the circuit breakers CP311, CP 312, ... CP 318.
consequences	<ul style="list-style-type: none"> • The stored energy of 10 J/coil at maximum will be dissipated mainly in the dumping resistors RD 311, ..., RD 318, and RD 321, ..., and RD 328. The time constant depends on the combination of the inductance and the resistance. The longest one is $0.27\ \text{H}/0.5\ \Omega = 0.54\ \text{sec}$.

Tab. 5.5: DR (Rapid discharge). Continues to Table 5.6.

ID	DR in Dipole
possible causes	<ul style="list-style-type: none"> • Detection of quench ($DT\ 381 > 10\ \text{mV}$ OR $DT\ 352 > 10\ \text{mV}$). Risk of the local overheating at the quench spot. • Voltage drop in Current Leads too high ($VS\ 381 > 80\ \text{mV}$). Risk of overheating in the current leads. • Temperature at the current leads too high ($TC\ 83 > -10\ ^\circ\text{C}$). Risk of overheating in the current leads.
actions by CCS2	<ul style="list-style-type: none"> • Shutdown Dipole PSU. • Open the circuit breaker CP 380. • Open the active valve FV 62 in order to release the rapidly evaporated He gas.
consequences	<ul style="list-style-type: none"> • The stored energy of 78 kJ will be dissipated mainly in the dumping resistor RD 380 ($0.44\ \Omega$). Its time constant is $0.37\ \text{H}/0.44\ \Omega = 0.84\ \text{sec}$ • In the case of a quench, some fraction of the energy will be dissipated at the quenching spot by ohmic heating.
comments	<ul style="list-style-type: none"> • The detection signal of DR in Dipole is used to close FV577 (valve for LHe transfer) in order to avoid sending high pressure into the LHe buffer dewar.

Tab. 5.6: DR (Rapid discharge). Continued from 5.5.

5.4 Anomalous cases

It is important to design or understand how the magnet system reacts and how the stored energy will be dissipated in the case of anomalous cases. Here, the term *anomalous* means the situation like the loss of mains electric power (AC 230 V or AC 380 V) the loss of cooling water and so on.

how Magnet is prepared against the loss of mains electricity at the platform is shown in Table 5.7 and that against the other cases is in Table 5.8. The instruments at the control room is powered by another normal mains electricity, which is common to the rest of COMPASS collaboration. The case of loss of the normal mains electricity at the control room is shown in Table 5.9.

ID	AN1
case	Loss of normal mains electric power EXD415/HN2
possible causes	<ul style="list-style-type: none"> • power cut. • accidents. • (In the case of AUL or AUG, see AN4.)
consequences	<ul style="list-style-type: none"> • Solenoid PSU loses electricity. • Dipole PSU loses electricity.
stored energy	<ul style="list-style-type: none"> • The stored energy in Solenoid or Dipole will be dissipated in the transistor bank in the corresponding PSU in an uncontrolled manner. Experience shows that it takes ~ 10 (1.5) minutes to reach 0 A in Solenoid (Dipole).
ID	AN2
case	Loss of diesel mains electricity EAD415/HN2.
possible causes	<ul style="list-style-type: none"> • power cut. • accidents. • (In the case of AUL or AUG, see AN4.)
consequences	<ul style="list-style-type: none"> • The vacuum pumps C 40 (Rotary pump) and C 42 (Diffusion pump) lose their power. • Usually no problem because the vacuum tightness is good, cryopumping is strong, and EAD415/HN2 will usually (excepted for AUL/AUG) restarts in tens of seconds. • At the worst case, the bad vacuum causes DL in Solenoid and in Dipole.
stored energy	<ul style="list-style-type: none"> • (For the worst case, see Section 5.3 for DL.)
ID	AN3
case	Loss of UPS mains electricity EOD415/HN2.
possible causes	<ul style="list-style-type: none"> • CERN UPS battery became empty after long power cut. • accidents. • (In the case of AUL or AUG, see AN4.)
consequences	<ul style="list-style-type: none"> • The surveillance electronics in Rack BI and the circuit breakers (CP350, CP380, CP311, ..., CP318, CP321, ..., CP328) in rack BP lose the electricity. Without electricity, all the circuit breakers become OPEN. • Opening the circuit breakers has practically the same effect as DR does. See Section 5.3.
stored energy	<ul style="list-style-type: none"> • The stored energy in Solenoid, Corrections, and Dipole will be dissipated like in DR. See Section 5.3.

Tab. 5.7: The behavior in the anomalous cases, loss of electricity. Continues to Table 5.8. ANx is the short expression for the identification (ID) of each anomalous case.

ID	AN4
case	CERN AUL or AUG
possible causes	<ul style="list-style-type: none"> • Somebody pressed one of the AUL/AUG buttons. • Accident in the cabling related to AUL/AUG.
consequences	<ul style="list-style-type: none"> • All the electricity more than 50 V at the platform will be lost. • Solenoid PSU loses the electricity. • Dipole PSU loses the electricity. • The vacuum pumps C 40 (Rotary pump) and C 42 (Diffusion pump) lose the electricity. • The surveillance electronics in Rack BI and the circuit breakers (CP350, CP380, CP311, ..., CP318, CP321, ..., CP328) in rack BP lose the electricity. Without electricity, all the circuit breakers become OPEN. • Opening the circuit breakers has practically the same effect as DR does. See Section 5.3.
stored energy	<ul style="list-style-type: none"> • The stored energy in Solenoid, Corrections, and Dipole will be dissipated like in DR. See Section 5.3.
ID	AN5
case	Solenoid PSU inoperational
possible causes	<ul style="list-style-type: none"> • Loss of cooling water for Solenoid PSU. • Internal error in Solenoid PSU (overheating, overcurrents, etc).
consequences	<ul style="list-style-type: none"> • Solenoid PSU shuts down by itself.
stored energy	<ul style="list-style-type: none"> • The stored energy in Solenoid will be dissipated in the transistor bank in Solenoid PSU in an uncontrolled manner. Experience shows that it takes ~ 10 minutes to reach 0 A.
ID	AN6
case	Dipole PSU inoperational
possible causes	<ul style="list-style-type: none"> • Loss of cooling water for Dipole PSU. • Internal error in Dipole PSU (overheating, overcurrents, etc).
consequences	<ul style="list-style-type: none"> • Dipole PSU shuts down by itself.
stored energy	<ul style="list-style-type: none"> • The stored energy in Dipole will be dissipated in the transistor bank in Dipole PSU in an uncontrolled manner. Experience shows that it takes ~ 1.5 minutes to reach 0 A.

Tab. 5.8: The behavior in the anomaly cases. Continued from Table 5.7. Continues to 5.9. AUL stands for Arrêt Urgent Local (emergency local stop), and AUG for Arrêt Urgent Général (emergency general stop), according to CERN safety regulation.

ID	AN7
case	Loss of normal mains electricity in the control room
possible causes	<ul style="list-style-type: none"> • Somebody pressed one of the AUL/AUG buttons. • Accident in the cabling related to AUL/AUG.
consequences	<ul style="list-style-type: none"> • In the first ~ 10 minutes, <ul style="list-style-type: none"> · PSUs for Corrections goes 0 A. The field homogeneity will be lost and one has to stop microwaves to avoid the loss of polarization. · VME system and SUN computer is powered by the local UPS boxes. <ul style="list-style-type: none"> · Solenoid PSU is operational. · Dipole PSU is operational. · FV 577 (valve for LHe transfer) is operational, powered by the local UPS boxes. • After the local UPS boxes become empty, the situation will be complicated. <ul style="list-style-type: none"> · VME system and SUN computer lose the electricity. <ul style="list-style-type: none"> · Solenoid PSU keeps the current according to the setting value even after VME system loses the electricity. The current setting value is held inside the PSU itself owing to RS232 communication scheme.) One can keep the polarization in frozen spin mode. · The current setting value for Dipole becomes 0 A and the slope setting value for it does 0 A/s. The Dipole current will be held in an abnormal way. · FV 577 (valve for LHe transfer) is inoperational and will be completely closed. DL will soon be caused because of the small flow along the current leads.
stored energy	<ul style="list-style-type: none"> • The stored energy in Correction coils will be dissipated inside the transistor banks in the corresponding PSUs. • Once DL is caused due to the small flow along the current leads, stored energies in Solenoid and Dipole will be dissipated like in DL. See Section 5.3.

Tab. 5.9: The behavior in the anomalous cases. Continued from Table 5.8.

6. CONCLUSIONS AND OUTLOOK

There are still mysteries in the spin structure of the nucleon. Only small fraction 20-30 % of the nucleon spin is carried by quarks at $Q^2 = 10 \text{ GeV}^2$. The Ellis-Jaffe sum rule is violated while the Bjorken Sum Rule is verified.

The main goal in the COMPASS experiment is to measure the gluon spin contribution to the nucleon spin. The author contributed to the start-up of the large polarized target system for the COMPASS experiment. There were crucial requirements which the polarized target system had to fulfill.

One of the requirements was to have a large number of nucleon scattering centers and a high 'figure of merit' target in order to improve the statistical accuracy of the $\Delta g/g$ measurement since the beam flux is limited to $1.6 \cdot 10^{11} \text{ muons cm}^{-2} \text{ day}^{-1}$ and the cross section of interest is as small as about 2nb. The world largest polarized target system is used to realize a large number of scattering centers of $N_{\text{sc}} = 2.6 \cdot 10^{26}$, corresponding to the material volume of 420 cm^3 . The 'figure of merit' defined as $F = \kappa \rho (f P_T)^2$, where κ is the packing factor, ρ is the density of the material, f is the dilution factor (fraction of the polarizable nucleons), and P_T is the target polarization, is important since it is inversely proportional to the beam time to achieve a certain statistical accuracy of the double spin asymmetry. ${}^6\text{LiD}$ was chosen as the material for its unrivaled dilution factor which is about 0.5 and for its potential to be polarized as high as 50 %.

In order to obtain high polarization, the material was studied and prepared carefully and the dynamic nuclear polarization (DNP) process was surveyed. A large amount of ${}^6\text{LiD}$ with a paramagnetic center concentration of $2 \cdot 10^{19}/\text{g}$ was produced. The electron paramagnetic (EPR) spectrum is consistent with the atomic structure of F-center and its hyperfine coupling constant is determined to be $7.1 \cdot 10^{-27} \text{ J}$. The transition probability calculated from a quantum mechanical description shows that the conventional DNP picture via dipolar dipolar interaction is dominant while the hyperfine interaction is visible in the EPR spectrum.

In order to realize the high polarization, all the subsystems of the polarized target apparatus were also prepared carefully to show high performance. The dilution refrigerator provided the base temperature of 80 mK and high

cooling power of 1 Watt at 0.4 K, increasing the thermal relaxation time of the nuclear spin. The large superconducting magnet system produced 2.5 T longitudinal field with an homogeneity of $\pm 3 \times 10^{-5}$, in which the DNP was performed efficiently. The high power 70 GHz microwave system was used in order to enhance the polarization in the large volume and the frequency modulation technique was implemented in order to gain the polarization. In the long term and statistics critical COMPASS experiment, the stability of the apparatus is also the key factor. The author successfully installed the large superconducting magnet system, which uses 650 A and stores 488 kJ, with special considerations on the stability, reliability, and the protection of the hardware.

The high degree of deuteron polarizations, +54.2% and -47.1%, were achieved by DNP with the microwave frequency modulation technique. The shift of the optimum microwave frequency was observed depending on the sign and the degree of the polarization. The bolometric EPR spectrum at high polarization was taken to obtain the insight of the DNP process. The EPR spectrum showed the shift of the main absorption peak, which can explain the shift of the optimum microwave frequency. It also showed that the shift of the main absorption peak could be due to the hyperfine interaction with the six adjacent ${}^6\text{Li}$ nuclei whose polarizations are nearly 100%. These high nuclear polarizations near the paramagnetic centers confirm the DNP mechanism.

One of the other requirements was to know the polarization of all the polarizable nuclei, precisely. In ${}^6\text{LiD}$, ${}^6\text{Li}$ and a small fraction of ${}^7\text{Li}$ as well as deuterons are polarizable and their polarization must be determined. The precise polarization measurement was done by nuclear magnetic resonance (NMR) technique using a series LRC continuous wave Q-meter. The polarizations of the large volume was monitored by ten NMR coils which were embedded in the target cells. The deuteron polarization was measured with an accuracy of 1.0% absolute on average. All the NMR circuits are tuned to the deuteron Larmor frequency at 2.5 T and is not possible to measure the lithium polarization during the beam time. In order to know the polarization of all the polarizable nuclei, the equal spin temperature (EST) theory was tested. The measurement showed that the EST holds between deuterons, ${}^6\text{Li}$ and ${}^7\text{Li}$ during the DNP process down to the spin temperature of ± 1 mK. The confirmation of the EST theory in this large volume and at such a low spin temperature is the world first result. The measured agreement with EST theory is particularly important in the COMPASS experiment for the following reasons. The installation of extra coils to monitor lithium polarizations, which would decrease the amount of the target

material and increase the complication in the evaluation of the scattering events of interest, is not necessary. The change of the longitudinal magnetic field to monitor lithium polarizations during the beam time, which would also impose the complication in the analysis of the events of interest, is not necessary, either.

With the achieved high polarizations of ${}^6\text{LiD}$, the target figure of merit reached 22.8 kg/m^3 , which is better than that of the ammonia, the second best material, by a factor of 1.8.

There was a requirement also on the thickness of material to minimize the multiple scattering for the efficient reconstruction of the invariant mass of D^0 from the decay particles. On the other hand, the double target cell configuration, where the cells were polarized with opposite directions each other and the spins were reversed by a magnetic field rotation every 8-12 hours, was required in order to suppress the systematic errors due to the time dependent variation in the beam flux and in the spectrometer efficiency. Such a polarization configuration demands the metal material to isolate the microwave cavities for the two cells. The microwave stopper with minimum thickness was developed. The stopper was proved to have an isolation factor of more than 20 dB at room temperature and worked satisfactorily in the real operation. The total radiation length for the particles produced at the upstream end of the cell and scattered at 69 mrad is minimized to $0.2X_0$.

These good performances of the polarized target system achieved by the author's efforts enabled the COMPASS experiment to start the data taking in 2002. The COMPASS experiment will measure the gluon polarization $\Delta g/g$ in the nucleon spin with the accuracy of $\sim 10\%$ in the coming years. The data will constrain the gluon spin distribution function Δg , select the valid theoretical models among many of them, and improve the understanding of the spin structure of the nucleon.

APPENDIX

A. PARAMETERS IN CHAPTER 3

variable	description
k	four-vector of the incoming muon.
k'	four-vector of the outgoing muon.
E_μ	energy of incoming muon.
q	four-vector of the virtual photon. $q = k - k'$
Q^2	squared momentum transfer by muon. $Q^2 = -q^2$
ν	energy of the virtual photon.
y	energy ratio of the virtual photon to the incoming muon. $y = \nu/E_\mu$
q_g	four-vector of the involved gluon.
$p_c (p_{\bar{c}})$	four vector of the produced charm (anticharm) quark.
p_n	four-vector of the nucleon.
m_n	mass of the nucleon.
\hat{s}	one of the Mandelstam variables of photo-gluon fusion process. $\hat{s} = (q + q_g)^2$ squared center-of-mass energy.
\hat{t}	one of the Mandelstam variables of photo-gluon fusion process. $\hat{t} = (q + p_c)^2$
\hat{u}	one of the Mandelstam variables of photo-gluon fusion process. $\hat{u} = (q + p_{\bar{c}})^2$
η	$\hat{s}/(2m_n\nu) = \hat{s}/(2m_nE_\mu y)$ naively, the momentum fraction carried by the gluon in the nucleon.
β	$\sqrt{1 - (4m_c^2/\hat{s})}$
W	$W = 4m_c^2 + Q^2(1 - \beta^2)$
S	c.m. energy of the muon and the nucleon. $S = (k + p_n)^2$
s'	c.m. energy of the virtual photon and the nucleon. $s' = 2m_nE_\gamma = 2m_nE_\mu y$

Tab. A.1: Variables in Chapter 3 to discuss photon-gluon fusion process.

B. PARAMETERS IN CHAPTER 4

μ_0	permeability of vacuum	$4\pi \cdot 10^{-7}$	N A^{-2}
h	Planck constant	$6.626\,075 \cdot 10^{-34}$	J s
\hbar	(Reduced) Planck constant	$= h/2\pi = 1.054\,572\,66 \cdot 10^{-34}$	J s
k_B	Boltzmann constant	$1.380\,658 \cdot 10^{-23}$	J K^{-1}
μ_B	Bohr magneton	$9.274\,015 \cdot 10^{-24}$	J T^{-1}
μ_e	magnetic moment of electron	$1.001\,160 \mu_B = 9.284\,770 \cdot 10^{-24}$	J T^{-1}
g_e	electron g-factor $2(1 + a_e)$	$= 2\mu_e/\mu_B = 2.002\,319$	
μ_N	nuclear magneton	$5.050\,786 \cdot 10^{-27}$	J T^{-1}
μ_p	magnetic moment of proton	$2.792\,8474 \mu_N = 1.410\,607 \cdot 10^{-26}$	J T^{-1}
g_p	g factor of proton	$= 2\mu_p/\mu_N = 5.585\,695$	
μ_D	magnetic moment of deuteron	$0.857\,4382 \mu_N = 4.330\,737 \cdot 10^{-27}$	J T^{-1}
g_D	g factor of deuteron	$= \mu_D/\mu_N = 0.857\,4382$	
$\mu_{^6\text{Li}}$	magnetic moment of ^6Li	$0.822\,0467 \mu_N = 4.151\,982 \cdot 10^{-27}$	J T^{-1}
$g_{^6\text{Li}}$	g factor of ^6Li	$= \mu_{^6\text{Li}}/\mu_N = 0.822\,0467$	
$\mu_{^7\text{Li}}$	magnetic moment of ^7Li	$3.256\,427 \mu_N = 1.644\,752 \cdot 10^{-26}$	J T^{-1}
$g_{^7\text{Li}}$	g factor of ^7Li	$= \frac{3}{2} \frac{\mu_{^7\text{Li}}}{\mu_N} = 2.170\,951$	

Tab. B.1: Constants in Chapter 4

frequency	Hertz	Hz	s^{-1}	
force	Newton	N	m kg s^{-2}	
energy, work, heat	Joule	J	N m	$= \text{m}^2 \text{kg s}^{-2}$
magnetic flux density	Tesla	T	V s m^{-2}	$= \text{kg s}^{-2} \text{A}^{-1}$

Tab. B.2: Units for Chapter 4

DNP	Dynamic Nuclear Polarization
EST	Equal Spin Temperature
TE	Thermal Equilibrium
EPR	Electron Paramagnetic Resonance \simeq ESR
ESR	Electron Spin Resonance \simeq EPR
NMR	Nuclear Magnetic Resonance

Tab. B.3: Abbreviations in Chapter 4

C. PARAMETERS IN CHAPTER 5

French	English
principal(e)	principal, main
décharge rapide	fast discharge
décharge lent	slow discharge
correction	correction, trim
contacteur principal	main circuit breaker
défaut interne	internal defect/error
Affichage du courant	digital indication of current
gaz	gas
recuperation	recuperation/recovery

Tab. C.1: Terms in Chapter 5.

	French	English
AL	Alimentation	power supply
CP	Contacteur Principal	main circuit breaker
TE	Température, Émetteur	Temperature Emitter/sensor
TC	Température, Controlleur	Temperature Controller (electronics)
E	Échauffeur	heater element
DT	Détecteur du Transition	transition/quench detector (electronics)
VS	Voltage Sonde (Seuil/Signalisation)	Voltage Sensor (threshold/signalling/switch)
RD	Resisteur pour Décharge	dumping/discharge resistor
DM	Défaut du Mass	defect/error in grounding
LHe	Liquide, Helium (^4He)	Liquid Helium (^4He)
LN2	Liquide, azote (N_2)	Liquid nitrogen (N_2)
FIS	Debit, Indicateur et Sonde (Seuil/Signalisation)	flow indicator and the sensor (threshold/signalling/switch)
HV	vanne à main	Hand Valve (manual control, usually)
FV	vanne pour ajuster le debit	Flow Valve (electrical control, usually)
PCV	Pression, Controller, Vanne	Pressure Control Valve
PSV	Pression, Securite, Vanne	pressure relief valve (mechanical, passive, recoverable)
PSE	Pression Securite Élément	rupture/burst disk (passive, non-recoverable)
LI	niveau, indicateur	Level Indicator
LE	niveau, émetteur,	Level Emitter/sensor
LC	niveau, controlleur	Level Controller (electronics)
PI	Pression, Indicateur	Pressure Indicator
PS	Pression, Sonde (Seuil/Signalisation)	Pressure Sensor (threshold/signalling/switch)
PT	Pression, Transducteur	Pressure Transmittor/Transducer
	COLD BOX	He liquefier at CERN
RAZ	Remise à Zero	Put back / reset to zero
AUL	Arrêt Urgent Local	local emergency stop
AUG	Arrêt Urgent Général	general emergency stop

Tab. C.2: Abbreviations in Chapter 5. AUL and AUG are defined in CERN safety regulation.

BIBLIOGRAPHY

- [1] E80 collaboration, M. J. Alguard *et al.*, Phys. Rev. Lett., 37 (1967) 1261. *Deep Inelastic Scattering of Polarized Electrons by Polarized Protons.*
- [2] E130 collaboration, G. Baum *et al.*, Phys. Rev. Lett, 51 (1983) 1135. *A New Measurement of Deep Inelastic e p asymmetries.*
- [3] European Muon Collaboration (EMC), J. Ashman *et al.*, Phys. Lett. B206 (1988) 364. *Measurement of the Ratios of Deep Inelastic Muon Nucleus Cross-Sections on Various Nuclei Compared to Deuterium.*
- [4] European Muon Collaboration (EMC), J. Ashman *et al.*, Nucl. Phys. B328 (1989) 1. *An Investigation of the Spin Structure of the Proton in Deep Inelastic Scattering of Polarized Muons on Polarized Protons.*
- [5] J. Ellis and R. Jaffe, Phys. Rev. D9 (1974) 1444. *Sum rule for deep-inelastic electroproduction from polarized protons.*
Erratum: *ibid.* D10 (1974) 1669.
- [6] J. D. Bjorken, Phys. Rev. 148 (1966) 1467. *Applications of the Chiral $U(6) \otimes U(6)$ Algebra of Current Densities.*
- [7] J. D. Bjorken, Phys. Rev. D1 (1970) 1376. *Inelastic Scattering of Polarized Leptons from Polarized Nucleons.*
- [8] R. L. Jaffe and A. Manohar, Nucl. Phys. B337 (1990) 509. *The g_1 Problem: Deep Inelastic Electron Scattering and the Spin of the Proton.*
- [9] F. E. Close, *An Introduction to Quarks and Partons*, Academic Press, (1979).
- [10] F. Halzen and A. D. Martin, *Quarks and Leptons*, John Wiley & Sons (1984).
- [11] E. Leader and E. Predazzi, *An Introduction to Gauge Theories and the New Physics*, Cambridge University Press (1985).

-
- [12] A. V. Manohar, *An Introduction to Spin Dependent Deep Inelastic Scattering in Symmetry and Spin in the Standard Model: Proceedings of the Seventh Lake Louise Winter Institute 1992*, B. A. Campbell, A.N. Karmal, F.C. Khanna (Editor), L. G. Greeniaus, World Scientific (1992).
- [13] Particle Data Group, *Review of Particle Physics*, Recent publications are
- D. E. Groom *et al.*, Eur. Phys. J. C15 (2000) 1.
- K. Hagiwara *et al.*, Phys. Rev. D66 (2002) 010001.
- [14] B. L. Ioffe, V. A. Khoze and L. N. Lipatov, *Hard Processes: Phenomenology, Quark-Parton Model*, North Holland (1984).
- [15] M. Anselmino, A. Efremov and E. Leader, Phys. Rep. 261 (1995) 1. *The Theory and Phenomenology of Polarized Deep Inelastic Scattering*.
- [16] C. F. v. Weizsäcker, Z. Phys. 88 (1934) 612. *Radiation Emitted in Collisions of Very Fast Electrons*.
- [17] E. J. Williams, Phys. Rev. 45 (1934) 729. *Nature of the High-Energy Particles of Penetrating Radiation and Status Ionization and Radiation Formulae*.
- [18] N. H. Hand, Phys. Rev. 129 (1963) 1834. *Experimental Investigation of Pion Electroproduction*.
- [19] A. Mendez, Nucl. Phys. B145 (1978) 199. *QCD Predictions for Semi-inclusive and inclusive leptoproduction*.
- [20] L. W. Whitlow *et al.*, Phys. Lett. B250 (1990) 193. *A Precise Extraction of $R = \sigma_L/\sigma_T$ from a Global Analysis of the SLAC Deep Inelastic ep and ed Scattering Cross-Section*.
Note: This reference contains a typographic mistake. Correct is $b_1 = 0.0635$.
- [21] K. Abe *et al.*, Phys. Lett. B452 (1999) 194. *Measurements of $R = \sigma_L/\sigma_T$ for $0.03 < x < 0.1$ and Fit to World Data*.
- [22] C. G. Callan and D. J. Gross, Phys. Rev. Lett. 22 (1969) 156. *High-Energy Electroproduction and the Constitution of the Electric Current*.
- [23] M. G. Doncel and E. De Rafael, Nuovo Cimento 4A (1971) 363. *Inelastic Lepton Scattering from Nucleons and Positivity Restrictions*.

-
- [24] P. Gnädig and F. Niedermayer, Nucl. Phys. B55 (1973) 612. *Positivity Inequalities for Spin-dependent Lepton-Hadron Scattering from the Light Cone Algebra of Quark Currents.*
- [25] Spin Muon Collaboration (SMC), D. Adams *et al.*, Phys. Lett. B336 (1994) 125. *Spin Asymmetry in Muon-Proton Deep Inelastic Scattering on a Transversely Polarized Target.*
- [26] Spin Muon Collaboration (SMC), D. Adams *et al.*, Phys. Lett. B396 (1997) 338. *The Spin Dependent Structure Function $g_1(x)$ of the Deuteron from Polarized Deep Inelastic Muon Scattering.*
- [27] E143 Collaboration, K. Abe *et al.* Phys. Rev. Lett. 76 (1996) 587. *Measurements of the Proton and Deuteron Spin Structure Function g_2 and Asymmetry A_2 .*
- [28] E154 Collaboration, K. Abe *et al.*, Phys. Lett. B404 (1997) 377. *Measurement of the Neutron Spin Structure Function g_2^n and Asymmetry A_2^n .*
- [29] E155 Collaboration, P. L. Anthony *et al.* Phys. Lett. B458 (1999) 529. *Measurement of the Proton and Deuteron Spin Structure Functions g_2 and Asymmetry A_2 .*
- [30] R. P. Feynman, Phys. Rev. Lett. 23 (1969) 1415. *Very High-Energy Collisions of Hadrons.*
- [31] J. D. Bjorken and E. A. Paschos, Phys. Rev. 185 (1969) 1975. *Inelastic Electron-Proton and γ -Proton Scattering and the Structure of the Nucleon.*
- [32] J. Lichtenstadt and H. J. Lipkin, Phys. Lett. B353 (1995) 119. *Spin contents of nucleons with $SU(3)$ breaking.*
- [33] D. Bailin, *Weak Interactions*, Sussex University Press (1982).
- [34] WA2 Group, M. Bourquin *et al.*, Z. Phys. C21 (1983) 17. *Measurements of Hyperon Semileptonic decays at the CERN Super Proton Synchrotron. Test of the Cabibbo Model.*
- [35] - J. R. Ellis and M. Karliner, Phys. Lett. B313 (1993) 131. *Analysis of Data on Polarized Lepton-Nucleon Scattering.*
- J. R. Ellis and M. Karliner, *Spin Structure Functions*, Plenary talk at 13th International Conference on Particles and Nuclei, PANIC '93, Perugia, Italy. Published in Perugia PANIC 1993, p48

-
- [36] G. Altarelli and G. Parisi, Nucl. Phys. B126 (1977) 298. *Asymptotic Freedom in Parton Language.*
- [37] R. K. Ellis, W. J. Stirling, and B. R. Webber, *QCD and Collider Physics*, Cambridge University Press (1996).
- [38] W. A. Bardeen, A. J. Buras, D. W. Duke and T. Muta, Phys. Rev. D18 (1978) 3998. *Deep Inelastic Scattering beyond the Leading Order in Asymptotically Free Gauge Theories.*
- [39] R. G. Roberts, *The Structure of the proton: Deep Inelastic Scattering*, Cambridge University Press (1990).
- [40] R. D. Ball, S. Forte, and G. Ridolfi, Phys. Lett. B378 (1996) 255. *Next-to-Leading Order Determination of the singlet axial charge and the polarized gluon content of the nucleon.*
- [41] Y. L. Dokshitzer, Sov. Phys. JETP 46 (1977) 641. *Calculation of Structure Functions of Deep-Inelastic Scattering and e^+e^- Annihilation by Perturbation Theory in Quantum Chromodynamics.*
- [42] - V. N. Gribov and L. N. Lipatov, Sov. J. Nucl. Phys. 15 (1972) 438. *Deep Inelastic ep Scattering in Perturbation Theory.*
- L. N. Lipatov, Sov. J. Nucl. Phys. 20 (1975) 94. *The Parton Model and Perturbation Theory.*
- [43] G. Altarelli, Phys. Rep. 81 (1982) 1. *Partons in Quantum Chromodynamics.*
- [44] A. D. Martin, W. J. Stirling and R. G. Roberts, Phys. Rev. D50 (1994) 6734. *Parton Distributions of the Proton.*
- [45] M. Glück, E. Reya, A. Vogt, Eur. Phys. J. C5 (1998) 461. *Dynamical Parton Distributions Revisited.*
- [46] M. Glück, E. Reya, M. Stratmann and W. Vogelsang, Phys. Rev. D53 (1996) 4775. *Next-To-Leading Order Radiative Parton Model Analysis of Polarized Deep Inelastic Lepton-Nucleon Scattering.*
- [47] H. L. Lai, J. Huston, S. Kuhlmann, F. I. Olness, J. F. Owens, D. E. Soper, W. K. Tung and H. Weerts, Phys. Rev. D55 (1997) 1280. *Improved Parton Distributions from Global Analysis of Recent Deep Inelastic Scattering and Inclusive Jet Data.*

-
- [48] A. D. Martin, R. G. Roberts, W. J. Stirling and R. S. Thorne, Eur. Phys. J. C4 (1998) 463. *Parton Distributions: A New Global Analysis*.
- [49] Spin Muon Collaboration, B. Adeva *et al.*, Phys. Rev. D58. (1998) 112002. *A Next-To-Leading Order QCD Analysis of the Spin Structure Function g_1* .
- [50] Y. Goto, N. Hayashi, M. Hirai, H. Horikawa, S. Kumano, M. Miyama, T. Morii, N. Saito, T. A. Shibata, E. Taniguchi, and T. Yamanishi, Phys. Rev. D62 (2000) 034017. *Polarized Parton Distribution Functions in the Nucleon*.
- [51] A. L. Kataev Phys. Rev. D50 (1994) 5469 *The Ellis-Jaffe Sum Rule: The Estimates of the Next to Next-To-Leading Order QCD Corrections*.
- [52] J. R. Ellis and M. Karliner Phys. Lett. B341 (1993) 397 *Determination of α_s and the Nucleon Spin Decomposition using recent polarized structure function data*.
- [53] E. B. Zijlstra and W. K. van Neerven, Nucl. Phys. B417 (1994) 61. *Order- α_s Corrections to the Polarized Structure Functions $g_1(x, Q^2)$* .
- [54] R. Mertig and W. L. van Neerven, Z. Phys. C70 (1996) 637. *The Calculation of the Two-Loop Spin Splitting Function $P_{ij}^{(i)}$* .
- [55] W. Vogelsang Phys. Rev. D54 (1996) 2023. *Rederivation of the Spin-Dependent Next-To-Leading Order Splitting Functions*.
- [56] S. J. Brodsky, J. Ellis and M. Karliner, Phys. Lett. B206 (1988) 309. *Chiral Symmetry and the Spin of the Proton*.
- [57] G. M. Shore and G. Veneziano, Phys. Lett. B244 (1990) 75. *The $U(1)$ Goldberger-Treiman Relation and the Two Components of the Proton "spin"*.
- [58] G. M. Shore and G. Veneziano, Nucl. Phys. B381, 1992, 23. *The $U(1)$ Goldberger-Treiman Relation and the Two Components of the Proton "spin": A Renormalisation Group Analysis*.
- [59] S. Narison, G. M. Shore and G. Veneziano, Nucl. Phys. B433 (1995) 209. *Target Independence of the EMC-SMC effect*.
- [60] S. A. Larin and J. A. M. Vermaseren, Phys. Lett. B259 (1991) 345. *The α_s^3 Corrections to the Bjorken Sum Rule for Polarized electroproduction and to the Gross-Llewellyn Smith Sum Rule*.

-
- [61] M. Gourdin, Nucl. Phys. B38 (1972) 418. *Polarization Effects in Deep Electroproduction and the Quark Parton Model.*
- [62] A. V. Efremov and O. V. Teryaev, Dubna Report, (1988) JIN-E2-88-287. *Spin Structure of the Nucleon and Triangle Anomaly.*
- [63] G. Altarelli and G. Ross, Phys. Lett. B212 (1988) 391. *The Anomalous Gluon Contribution to Polarized Leptoproduction.*
- [64] R. D. Carlitz, J. D. Collins and A. H. Mueller, Phys. Lett. B214 (1988) 229. *The Role of the Axial Anomaly in Measuring Spin-Dependent Parton Distributions.*
- [65] J.S. Bell and R. Jackiw, Nuovo Cimento A60 (1969) 47. *A PCAC Puzzle: $\pi^0 \rightarrow \gamma\gamma$ in the σ -Model.*
- [66] S. L. Adler, Phys. Rev. 177 (1969) 2426. *Axial-Vector Vertex in Spinor Electrodynamics.*
- [67] S. L. Adler and W. A. Bardeen, Phys. Rev. 182 (1969) 1517. *Absence of Higher-Order Corrections in the Anomalous Axial-Vector Divergence Equation.*
- [68] R. Jackiw, *Current Algebra and Anomalies*, World Scientific (1985).
- [69] M. Glück and E. Reya, Z. Phys. C39 (1988) 569. *Spin Dependent Parton Distributions in Polarized Deep Inelastic Lepton Nucleon Scattering.*
- [70] J. Babcock, D. Sivers and S. Wolfram, Phys. Rev. D18 (1978) 162. *Quantum-Chromodynamic Estimates for Heavy Particle Production.*
- [71] T. Gehrmann and W. J. Stirling, Z. Phys. C65 (1995) 461. *Spin-Dependent Parton Distributions from Polarized Structure Function Data.*
- [72] A. D. Watson, Z. Phys. C12 (1982) 123. *Spin-Spin Asymmetries in Inclusive Muon Proton Charm Production.*
- [73] D. W. Duke and J. F. Owens, Phys. Rev. Lett. 44 (1980) 1173. *Charm Photoproduction with Linearly Polarized Photons.*
- [74] E. Eichten, I. Hinchliffe, K. D. Lane and C. Quigg, Rev. Mod. Phys. 56 (1984) 579. *Super Collider Physics.*
Erratum: *ibid.* 58 (1986) 1065.

-
- [75] COMPASS Proposal, CERN/SPSLC 96-14, SPSLC/P297, 1 March 1996.
- [76] The NA14 collaboration, M. P. Alvarez et al., Z. Phys. C60 (1993) 53. *Study of Charm photoproduction mechanisms.*
- [77] P. L. Frabetti et al., Phys. Lett. B263 (1991) 584. *A Measurement of the D^0 and D^+ lifetimes.*
- [78] M. Derrick et al, Phys. Lett. B349 (1995) 225. *Study of $D^{*(2010)\pm}$ Production in $e p$ Collisions at HERA.*
- [79] SLAC-PROPOSAL-E161, V. Ghazikhanian et al, *Proposal to Measure the Gluon Spin Distribution using Polarized Open Charm Photoproduction.*
- [80] A. Bravar, D. von Harrach and A. Kotzinian, Phys. Lett. B421 (1998) 349. *Large Gluon Polarization from Correlated high- p_T hadron pairs in polarized electro-production.*
- [81] The HERMES Collaboration, A. Airapetian et al, Phys. Rev. Lett. 84 (2000) 2584. *Measurement of the Spin Asymmetry in the Photoproduction of Pairs of High- p_T Hadrons at HERMES.*
- [82] M. Anselmino et al, hep-ph/0011299, DESY-2000-160, TPR-2000-20, DESY-00-160, (2000). *Electron Scattering with Polarized Targets at TESLA.*
- [83] For example,
- S. E. Vigdor, ep-ex/9905034, *The RHIC Spin Program: Snapshots of Progress.*, 13th International Symposium on High-energy Spin Physics, Protvino, Russia, Sep. 1998 - World Scientific, Singapore, 1999.
- [84] For example,
- The PHENIX Collaboration, D. P. Morrison, Nucl. Phys. A698 (2002) 565 *The PHENIX Experiment at RHIC.*
- [85] M. Frhr. von Hodenberg, Dipomarbeit, Universität Freiburg, *A First Reconstruction of COMPASS Data.*
- [86] - H. Fischer et al., IEEE Trans. Nucl. Sci., 49 (2002) 443. *The COMPASS Data Acquisition System*, 12th IEEE-NPSS Real Time Conference, Valencia, Spain, 2001.

-
- H. Fischer *et al.*, Nucl. Instr. and Meth. A461 (2001) 507-510 *Implementation of the Dead-Time Free F1 TDC*.
 - G. Baum *et al.*, CERN Yellow Report, CERN 99-09/p383, CERN-LHCC-99-033, hep-ex/9911009, *F1 : An Eight Channel Time-to-Digital Converter Chip for High Rate Experiments*.
 - G. Braun *et al.*, EHEP-98-08 2 Nov 1998. 5p, hep-ex/9810048, *TDC Chip and Readout Driver Developments for COMPASS and LHC-Experiments*.
- [87] For example, see below and references therein.
- M. Lamanna *et al.*, CHEP 2000, Computing in high energy and nuclear physics, p576, Batavia 2000, Advanced computing and analysis techniques in physics research, p238, *The COMPASS Computing Farm Project*.
- [88] L. Gatignon, *User Guide for the M2 beam*.
<http://gatignon.home.cern.ch/gatignon/M2manual.html>
- [89] C. S. Wu, E. Ambler, R. W. Hayward, D. D. Hoppes, and R. P. Hudson, Phys. Rev. 105 (1957) 1413. *Experimental Test of Parity Conservation in Beta Decay*.
- [90] The Spin Muon Collaboration (SMC), B. Adeva *et al.*, Nucl. Instr. and Meth. A343 (1994) 363. *Measurement of the Polarization of a High-Energy Muon Beam*.
- [91] N. Doble, L. Gatignon, G. von Holtey, and F. Novoskoltsev, Nucl. Instr. and Meth. A343 (1994) 351. *The Upgraded Muon Beam at the SPS*.
- [92] - S. Horikawa *et al.*, Nucl. Instr. and Meth. A431 (1999) 177. *Time Resolution of a Scintillating Fiber Detector*.
- I. Daito *et al.* Nucl. Instr. and Meth. A433 (1999) 587. *Time Resolution of Multi-Cladding Scintillating Fiber Hodoscope*.
- [93] A. Abragam, *Principle of Nuclear Magnetism*, Oxford University Press, London (1961).
- [94] C. D. Jeffries, *Dynamic Nuclear Orientation*, Interscience Publishers, a division of John Wiley & Sons, New York (1963).
- [95] M. Goldman, *Spin Temperature and Magnetic Resonance in Solids*, Oxford University Press, London (1970).

-
- [96] W. de. Boer, *Dynamic Nuclear Orientation of Nuclei at Low Temperatures*, CERN, Yellow Report 74-11 (1974)
- [97] F. Reif, *Fundamentals of Statistical and Thermal Physics*, McGraw-Hill Book Company, New York (1965).
- [98] J. J. Sakurai, *Modern Quantum Mechanics*, Addison-Wesley, New York (1985).
- [99] J. D. Jackson, *Classical Electrodynamics*, John Wiley & Sons, New York (1975).
- [100] C. P. Slichter, *Principles of Magnetic Resonances*, 3rd ed., Springer, Berlin (1990).
- [101] A. F. Kip, C. Kittel, R. A. Levy, and A. M. Portis, Phys. Rev. 91 (1953) 1066. *Electronic Structure of F centers: Hyperfine Interactions in Electron Spin Resonance.*
- [102] J. H. Van Vleck, Phys. Rev. 74 (1948) 1168. *The Dipolar Broadening of Magnetic Resonance Lines in Crystals.*
- [103] St. Goertz, Ch. Bradtke, H. Dutz, R. Gehring, W. Meyer, M. Plückthun, G. Reicherz, K. Runkel, and A. Thomas, Nucl. Instr. and Meth. A356 (1995) 20. *Investigations in high temperature irradiated ${}^{6,7}\text{LiH}$ and ${}^6\text{LiD}$, its dynamic nuclear polarization and radiation resistance.*
- [104] C. M. Dulya, Ph.D. Thesis, University of California, Los Angeles (1996). *The Polarization of Deuterons in Butanol and of Nitrogen Nuclei in Ammonia.*
- [105] Spin Muon collaboration (SMC), C. M. Dulya *et al.*, Nucl. Instr. and Meth. A398 (1997) 109. *A line-shape analysis for spin-1 NMR signals*
- [106] N. Takabayashi, Master Thesis, Nagoya University, Japan (1998). *Development of Deuterated Polarized Target.*
- [107] A. Abragam and W. G. Proctor, Phys. Rev. 109 (1958) 1441. *Spin Temperature.*
- [108] Spin Muon Collaboration (SMC), D. Adeva *et al.*, Nucl. Instr. and Meth. A419 (1998) 60. *Measurement of Proton and Nitrogen Polarization in Ammonia and a Test of Equal Spin Temperature.*

-
- [109] S. Bültmann *et al.*, Nucl. Instr. and Meth. A425 (1999) 23. *A Study of Lithium Deuteride as a Material for a Polarized Target.*
- [110] G. R. Court, D. W. Gifford, P. Harrison, W. G. Heyes and M. A. Houlden, Nucl. Instr. and Meth. A324 (1993) 433. *A High Precision Q-meter for the Measurement of Proton Polarization in Polarized Targets.*
- [111] SMC Collaboration, D. Adams *et al.*, Nucl. Instr. and Meth. A437 (1999) 23. *The Polarized Double Cell Target of the SMC.*
- [112] O. V. Lounasmaa, *Experimental Principles and Methods below 1 K*, Academic Press, London (1974).
- [113] F. Pobell, *Matters and Methods at Low Temperatures*, Springer, (1992).
- [114] A. Abragam, V. Bouffard, Y. Roinel and P. Roubeau, J. Phys. (Paris) L 41 (1980) 309. *A New Polarized Target Material: ${}^6\text{LiD}$.*
- [115] V. Bouffard, Y. Roinel and P. Roubeau, and A. Abragam, J. Phys. (Paris) 41 (1980) 1447. *Dynamic Nuclear Polarization in ${}^6\text{LiD}$.*
- [116] P. Chaumette, J. Derégel, G. Durand, J. Fabre and I. van Rossum, High Energy Spin Physics, Proceedings of the Eighth International Symposium, Minneapolis, 1988, edited by K. J. Heller, AIP Conference Proceeding (AIP, New York, 1989), Vol. 2, p.1275.
- [117] B. van den Brandt, J. A. Konter, S. Mango and M. Weßler, *Results from the PSI ${}^6\text{LiD}$ Target.* High Energy Spin Physics, Proceedings of the 9th International Symposium, Bonn, 1990, eds. W. Meyer, E. Steffens, W. Thiel, (Springer, Berlin 1991) p.320.
- [118] St. Goertz, Ph.D Thesis, Universität Bonn, BONN-IR-95-08.
- [119] A. Meier, Ph.D Thesis, Universität Bochum (2001).
- [120] St. Goertz, Habilitation, Universität Bochum (2002).
- [121] N. W. Schellingerhout, L. P. Kok, S. A. Coon, and R. M. Adam, Phys. Rev. C48 (1993) 2714. *Nucleon Polarization in Three-Body Models of Polarized ${}^6\text{Li}$.*
- [122] H. Walliser and T. Fliessbach, Phys. Rev. C31 (1985) 2242. *Cluster Picture of ${}^7\text{Li}$.*

-
- [123] - H. Preston-Thomas, *Metrologia* 27 (1990) 3.
- B. M. Magnum, *J. Res. Nat. Inst. Stand. Technol.* 95 (1990) 69.
- B. M. Magnum, G. T. Furukawa, *Nat. Inst. Stand. Technol., Technical Note* 1265 (1990).
- [124] J. J. Hill and D. A. Hill, *Nucl. Instr. and Meth.* 116 (1974) 269. *Simple Correction for Q-Meter Measurement of Proton Target Polarization.*
- [125] Yu. F. Kisselev, *Nucl. Instr. and Meth.* A356 (1995) 99. *The Modulation Effect on the Dynamic Polarization of Nuclear Spins.*
- [126] B. Adeva et al., *Nucl. Instr. and Meth.* A372 (1996) 339. Erratum *ibid.* A376 (1996) 490. *Large Enhancement of Deuteron Polarization with Frequency Modulated Microwaves.*
- [127] A. Abragam, M. Chapellier, J. F. Jacquinet, and M. Goldman. *J. Magn. Resonance* 10 (1973) 322. *Absorption Lineshape of Highly Polarized Nuclear Spin Systems.*
- [128] Y. Roinel and V. Bouffard, *J. Magn. Resonance* 18 (1975) 304. *First Moments of NMR Lines for Highly Polarized Nuclei: A Rigorous Version of the "Local Filed".*
- [129] A. Abragam and M. Goldman, *Rep. Prog. Phys.* 41 (1978) 395. *Principles of Dynamic Nuclear Polarisation.*
- [130] M. N. Wilson, *Superconducting magnet*, Oxford University Press (1983).
- [131] A. Daël, D. Cacaut, H. Desportes, R. Duthil, B. Gallet, F. Kircher, C. Lesmond, Y. Pabot, J. Thinel, *IEEE Trans. Magn.* 28 (1992) 560. *A Superconducting 2.5 T High Accuracy Solenoid and a Large 0.5 T dipole magnet for the SMC target.*
- [132] J. M. Le Goff et al., *Nucl. Instr. and Meth.* A356 (1995) 96. *Computer Control of the SMC polarized target.*

ACKNOWLEDGMENTS

First of all, I would like to thank my advisor Prof. Horikawa who provided me with the opportunity to join the COMPASS collaboration, to work locally at CERN, and made my work possible. I would also like to thank Prof. Hasegawa, Prof. Iwata, Prof. Daito, Prof. Matsuda, Dr. Ishimoto and the colleagues in our laboratory for their supports.

I am extremely indebted to the COMPASS polarized target group, Dr. Koivuniemi for his technical advises and coordination, Prof. Meyer for his expertise and his directorial supports, Dr. Magnon for his insights and being a perfect producer for the magnet project, Dr. Gautheron for his beautiful job in the IT part and his encouraging attitude, Dr. Goertz for the material and the introduction to the spin world, Dr. Reicherz for the NMR works and the material, Dr. Kisselev for his enthusiasm, Mr. Doshita for his excellent handling of dilution refrigerator, Ms. Kondo for her devotion to the NMR system, Prof. Baum, Dr. Ball, Dr Berglund and Dr. Gustafsson for their supports.

I would like to thank the COMPASS collaboration, especially Dr. Malot for making my stay possible and enormous amount of coordination, Dr. Le Goff for his efficient helps in the magnet control and acquisition system, Dr. Weise for the electromagnetic calculations, Dr. Baliev for the mechanical calculations.

Apparently, the COMPASS polarized target could not have started its operation and not have survived without wide spectrum of helps from many experts. Here, I would like to say thanks in French since I feel it is right.

Les travaux professionnels par M. J.M. DOMOLIS et M. V. PESARO, notre techniciens de COMPASS, ils étaient indispensable. Merci encore.

Je voudrais cordialement exprimer mes mercis à les experts de Saclay, C.E.A, France, M. A. Daël, M. B. Levesy, M. J-C. Gélébart, M. M. Cazanou, M. P. Clay, M. D. Pierrepont, M. J-Y. Rousse, M A. Le Coroller, M. J-M. Joubert, M. G. Dispau, M. A. Donati, M. J-L. Jannin, M. C. Lesmond, et tous les experts qui participaient le projet d'aiment. Vous avez sauvegardé ma vie.

Je voudrais exprimer mes mericis sincère á M. W. Flegel, M. E. Sbrissa,

M. N. Bourgeois, M. G. Crepet de CERN EP/TA3 et M. P. Fin de S.P.I.E. pour les aides en l'instrumentation de l'aimant. Je éprouvais du plaisir à travailler avec vous.

J'ai reçu les appuis larges de Division LHC/ECR CERN. Je remercie à M. K. Barth, M. C. Jouve, M. P. Alliod, M. S. Rangod, M. O. Pirrote, M. J. Cosson pour l'installation cryogenique. Je voudrais dire 'merci' cordialement à chaque opératrice et chaque opérateur dans Zone Nord, qui était professionnels et sympathiques, Je remercie à M. T. Niinikoski pour sa expertise dans la cible polarisée.

J'ai reçu les appuis par beaucoup de personnes à CERN. L'équip de M. G. Sigaud (EST/LEA) pour la câblage, L'équip de M. A. Castel (EST/LEA) pour l'azote argon, M. R. Bourgeois, M. A. Monsted et M. R. Mollay (ST/CV) pour l'installation d'eau refroidissement, L'équip de M. J. Gomez pour l'installation électrique, M. Y. Gaillard (SL/PO) pour l'interlock dans SPS, et l'opérateurs de ST/HM pour les grues et les transports. Je remercie toutes les service industrielles et administratives à CERN.

Je remercie à les secrétaires, Mme. Seiner et ses collègues de bâtiment 892, qui me aidaient beaucoup de chose, non seulement les affaires administratives, mais aussi la langue française, les affaires pratiques dans la vie de chacun jour. Je ne peut pas imaginer comment je aurais vécu sans vos aides.

Spending four years in Europe was a terrific experience to me. I sincerely thank everyone whom I met and who helped me. I appreciate the supports by the administration offices in Nagoya University and Japan Society for the Promotion of Science.

Finally, I would like to dedicate this thesis with my my best 'arigato' to my parents and my sisters.